

In vitro modeling of early mouse development

Présentée le 17 janvier 2020

à la Faculté des sciences de la vie
Unité du Prof. Lutolf
Programme doctoral en biotechnologie et génie biologique

pour l'obtention du grade de Docteur ès Sciences

par

Mehmet Ugur GIRGIN

Acceptée sur proposition du jury

Prof. B. Deplancke, président du jury
Prof. M. Lütolf, directeur de thèse
Dr B. Steventon, rapporteur
Dr N. Rivron, rapporteur
Prof. A. C. Oates, rapporteur

What I cannot create, I do not understand.

-

Know how to solve every problem that has been solved.

Richard Feynman

(February 1988)

Table of Contents

SUMMARY	5
RÉSUMÉ	7
CHAPTER I: INTRODUCTION	10
OBJECTIVE and AIMS	16
REFERENCES	17
CHAPTER II: MULTI-AXIAL SELF-ORGANISATION PROPERTIES OF MOUSE EMBRYONIC STEM CELLS INTO GASTRULOIDS	21
ABSTRACT	23
RESULTS and DISCUSSION	23
ACKNOWLEDGEMENTS	33
MATERIAL and METHODS	33
REFERENCES	41
SUPPLEMENTARY INFORMATION	45
CHAPTER III: ARTIFICIAL EPIBLASTS UNDERGO AXIAL MORPHOGENESIS AND FORM ANTERIOR NEURAL PROGENITORS INDEPENDENT OF EXOGENOUS WNT STIMULATION	62
ABSTRACT	64
INTRODUCTION	64
RESULTS	66
DISCUSSION	88
MATERIAL and METHODS	90
REFERENCES	92

CHAPTER IV: BIOENGINEERED EMBRYOIDS MIMIC POST-IMPLANTATION DEVELOPMENT IN VITRO	95
ABSTRACT	97
INTRODUCTION	97
RESULTS	99
DISCUSSION	113
MATERIAL and METHODS	116
REFERENCES	119
SUPPLEMENTARY INFORMATION	123
CHAPTER V: CONCLUSIONS AND OUTLOOK	129
REFERENCES	134
CHAPTER VI: CURRICULUM VITAE	138
ACKNOWLEDGEMENTS	141

SUMMARY

Embryonic development is a complex process integrating cell fate decisions and morphogenesis in a spatio-temporally controlled manner. Previous studies with model organisms laid the foundation of our knowledge on post-implantation development; however, studying mammalian embryos at this stage is a difficult and laborious process. Since their first isolation in mice, embryonic stem cells (ESCs) have become a valuable tool to study aspects of development in vitro. Due to the limited accessibility of the post-implantation mouse embryo, scientists have been using ESCs as a surrogate model for the early embryo. Although some aspects of embryogenesis could be recapitulated with ESCs, existing culture methodologies largely neglect key characteristics of the embryo such as its three-dimensional (3D) organization, cell type diversity, or interactions between embryonic and extra-embryonic tissues.

Previous attempts to recapitulate embryogenesis in a developmentally relevant context started with aggregates composed of a few thousand ESCs, termed embryoid bodies (EB), that upon induction of differentiation reveal a surprising level of autonomous cell fate patterning, in some cases giving rise to spatially arranged ectoderm, mesoderm and endoderm layers. However, cell fate patterning and morphogenesis in EBs is poorly reproducible and cannot be controlled. These limitations necessitate further research on the self-organization potential of ESCs, and in particular the development of more robust in vitro models mimicking post-implantation mouse embryos. This PhD thesis explored three novel approaches towards this goal.

Firstly, together with collaborators, I focused on a previously established in vitro model of gastrulation termed *gastruloids*. *Gastruloids* emerge from small ESC aggregates that, upon activation of Wnt signaling, break symmetry and undergo axial morphogenesis to create structures that are similar to the developing tail of the mouse embryo. A systematic improvement of the existing culture conditions allowed *gastruloids* to be cultured for an extended period of time, resulting in an embryo-like patterning along the three major body axes. Furthermore, gene expression analyses, combined with immunohistochemistry and in situ hybridization assays, demonstrated that *gastruloids* exhibit spatio-temporal activation of *Hox* genes in a way that is remarkably similar to post-implantation mouse embryos.

Secondly, I report a novel *gastruloid* culture approach, which for the first time promotes the formation of anterior neural tissues. Mouse ESCs were aggregated and treated in high-throughput in a bioengineered microwell array system to generate homogeneous ‘artificial epiblasts’ that transcriptionally and morphologically resemble post-implantation epiblasts.

These epiblast-like (EPI) aggregates break symmetry and undergo axial elongation to establish antero-posterior patterning. I provide evidence for attenuated Wnt signaling and the presence of an epithelium in the starting EPI aggregates as the major determinants for the formation of anterior neural tissues, that are completely absent in conventional *gastruloids*.

Lastly, I systematically explored the role of extraembryonic tissues in the patterning of artificial epiblasts. By combining EPI aggregates with trophoblast stem cell aggregates, hybrid self-organizing structures termed *EpiTS embryoids* were generated that mimic epiblast and extraembryonic ectoderm, respectively. *EpiTS embryoids* were found to execute an elaborate self-organization program that is initiated through highly localized gastrulation-like processes at the embryonic-extraembryonic interface. Upon axial elongation, *EpiTS embryoids* give rise to primitive brain-like and preplacodal ectoderm-like regions. These observations highlight the role of extraembryonic tissues for proper induction of gastrulation and in particular the formation of anterior neural tissues.

Altogether, this thesis introduces three innovative and highly versatile stem cell culture technologies to study post-implantation mouse embryonic development. The approaches are amenable to large-scale studies aimed at identifying novel regulators of gastrulation and anterior neural development that is currently out of reach with existing experimental tools. This work should contribute to the advancement of the nascent field of ‘synthetic embryology’, opening up exciting perspectives for various applications of pluripotent stem cells in disease modeling and tissue engineering.

Keywords: developmental biology, synthetic embryology, embryoids, hydrogel-based microwells, poly(ethylene) glycol (PEG), gastrulation, anterior neural development, epithelium, Wnt signaling, embryonic stem cells, trophoblast stem cells, symmetry breaking, self-organization, axial morphogenesis, epiblast, brain, placode

RÉSUMÉ

Le développement embryonnaire est un processus complexe constitué de décisions guidant le destin cellulaire et la morphogénèse des tissus de manière contrôlée dans l'espace et le temps. Bien que l'utilisation classiques d'organismes modèles ont fondé la base de notre connaissance sur le développement embryonnaire après implantation, l'étude d'embryons de mammifère à ce stade de développement est laborieuse et difficile. Depuis leur première isolation dans les embryons de souris, les cellules souches embryonnaires (CSE) sont devenues un outil clé pour étudier *in vitro* certains aspects du développement. Dû à l'accès limité d'embryons de souris au stade après implantation, les scientifiques utilisent donc depuis les CSE comme modèle de substitution à l'embryon. Néanmoins, bien que certains aspects de l'embryogénèse puissent être étudiés avec ce système, les méthodes de cultures conventionnelles négligent largement des caractéristiques clés de l'embryon comme son organisation tridimensionnelle (3D), sa diversité cellulaire ou encore l'interaction entre les tissus embryonnaires et extra-embryonnaires.

Les premières tentatives pour modéliser l'embryogénèse au plus proche possible du développement ont démarré avec des agrégats de quelques milliers de CSE, appelés « corps embryonnaires » qui, dès induit en différenciation, révèlent une capacité surprenante à s'organiser de manière autonome. Dans certains cas, il a pu être prouvé que les couches d'endoderme, mésoderme et ectoderme s'auto-arrangent naturellement. Pourtant, le destin des cellules ainsi que la morphogénèse des tissus grandissant dans ces corps embryonnaires n'est pas reproductible ni contrôlable. Ces limitations, nécessitent plus de recherche explorant la capacité d'auto-organisation des CSE et en particuliers le développement de modèles *in vitro* plus robustes pour mieux imiter la biologie embryonnaire après implantation. Ce travail de doctorat explore trois approches innovatrices afin de répondre à ces limitations.

Premièrement, dans le cadre d'une collaboration, je me suis focalisé sur un modèle de gastrulation *in vitro*, appelé « gastruloïdes ». Les gastruloïdes se forment à partir de petits agrégats de CSE qui, en activant la cascade de signalisation Wnt, induisent un processus de morphogénèse et s'allongent le long d'un axe bien défini pour former des structures ressemblantes à la queue de l'embryon en développement. Après une amélioration systématique des conditions de culture de ces gastruloïdes, j'ai pu significativement rallonger leur temps de vie en culture ce qui a aussi permis de faire apparaître les trois axes majeurs du corps dans ces structures. De plus, une analyse de l'expression des gènes combinée avec des analyses d'immunohistochimies et d'hybridation *in-situ* ont démontré que ces gastruloïdes

expriment les gènes Hox dans l'espace et dans le temps de manière quasiment identique à un réel embryon après implantation.

Deuxièmement, dans ce travail, j'ai pu établir une méthode innovante pour cultiver des gastruloïdes, qui, pour la première fois, contiennent des tissus neuraux bien plus antérieur que les gastruloïdes classiques. Je démontre qu'en agrégeant des CSE de souris à haut débit dans une plateforme de culture bio-ingénierée contenant des micro-puits en hydrogel, il est possible de former des épiblastes artificiels qui ressemblent à l'épiblaste après implantation autant du point de vue de l'expression des gènes que de leur morphologie. Ces épiblastes artificiels sont également capables d'induire un changement de symétrie ainsi qu'un allongement le long de l'axe antérieur-postérieur. J'ai pu aussi montrer qu'une atténuation de l'activation de la cascade de signalisation Wnt et la présence d'un épithélium dans les premiers jours de l'épiblaste artificiel sont deux facteurs déterminants pour la formation de tissus antérieurs tels que les tissus neuraux, des structures complètement absentes dans les gastruloïdes classiques.

Finalement, j'ai caractérisé systématiquement le rôle des tissus extra-embryonnaires dans le façonnage des épiblastes artificiels. En combinant de jeunes épiblastes artificiels avec des cellules souches du trophoblaste, j'ai pu générer des structures auto-organisées, appelées embyroïdes EpiTS, qui modèlent l'épiblastes et l'ectoderme extra-embryonnaire dans une même structure. Ces embyroïdes EpiTS s'auto-organisent de manière extrêmement élaborée. Cette auto-organisation surprenante est initiée à l'interface des tissus embryonnaire et extra-embryonnaire. Lors de l'allongement le long de leur axe, les embyroïdes EpiTS forment des débuts de tissus cérébraux et d'ectoderme préplacodale. Ces observations soulignent le rôle majeur des tissus extra-embryonnaires pour une induction appropriée de la gastrulation, en particuliers des tissus neuraux antérieurs.

De manière générale, ce travail de doctorat présente trois approches innovantes et extrêmement polyvalentes de cultures de CSE pour l'étude du développement embryonnaire de souris après implantation. Les méthodes présentées ici sont complètement compatible avec des études à large échelle ciblant l'identification de régulateurs encore inconnus de la gastrulation ainsi que du développement des tissus antérieurs neuraux, qui jusqu'à aujourd'hui fut impossible à cause du manque d'outils expérimentaux appropriés. Ce travail devrait contribuer à l'avancement de ce domaine naissant qu'est l'embryologie synthétique, et ouvre des perspectives attrayantes pour des applications variées telles que la modélisation de maladies et l'ingénierie de tissus utilisant des cellules souches pluripotentes.

Mots clés: biologie du développement, embryologie synthétique, embryoïdes, micropuits à base d'hydrogel, poly(ethylene) glycol (PEG), gastrulation, développement neural antérieur, épithélium, cascade de signalisation Wnt, cellules souches embryonnaires, cellules souches du trophoblaste, rupture de symétrie, auto-arrangement, morphogenèse axiale, épiblaste, cerveau, placodes

CHAPTER I

INTRODUCTION

Mouse embryonic development is a fascinating process that yields to establishment of a complete body plan and perfectly organized tissues within a span of few weeks. Numerous *in vivo* efforts have been made to understand how this complex process unfolds and to extrapolate these observations to human development. However, performing *in vivo* genetic experiments in mouse, compared to other model organisms, is often time consuming and hampered by limited accessibility of post-implantation embryos. This necessitates establishment of *in vitro* models to study early embryonic development.

The first attempts to model mouse embryonic development *in vitro* begun with a coincidental observation. When teratocarcinomas from neo-natal mouse testes were analyzed, scientists noticed a structural similarity to the developing mouse embryo¹, however, in a very disorganized manner. Hence, they called these tumors as “embryoid bodies”². It was further shown that embryoid bodies were transplantable^{3,4} and retained the tumor forming capacity to form cell types ranging from cartilage to neural tissue, a multipotency that later attributed to the embryonal carcinoma (EC) cells⁵. When EC cells were isolated from tumors and aggregated *in vitro*, the differentiation potential was recapitulated and these embryoid bodies exhibited spatial organization of endoderm and ectoderm layers, resembling mouse embryos at day 5 of development^{6,7}. The use of EC cells to mimic embryonic development was rapidly replaced by embryonic stem cells (ESCs) following their isolation in 1981^{8,9}. The first embryoid bodies formed from mouse ESCs were shown to differentiate into blood islands and myocardium *in vitro*¹⁰. In the following 30 years, embryoid bodies have been extensively used for directed differentiation of cell types originating from all three germ layers¹¹⁻¹³ but yet, remained inadequate to study embryonic development. Pioneering studies¹⁴ have demonstrated self-organization potential embryoid bodies to recapitulate, in a limited extent, gastrulation-like events and antero-posterior axis determination (e.g. polarized *T/Bra* expression) (**Fig. 1a, 2a**). However, this was not accompanied by axial morphogenesis.

More recently, originating from studies with embryonal carcinoma cells¹⁵, *gastruloids* have taken the extent of self-organization potential of mESCs to demonstrate that embryoid bodies could undergo axial morphogenesis^{16,17}. In this model, when treated with Wnt agonist CHIR99021, small aggregates of mESCs (~300 cells) were shown to break symmetry and demonstrated polarized *T/Bra* expression in a reproducible way. When cultured further, *gastruloids* elongated and established patterning along antero-posterior, dorso-ventral and medio-lateral axes. Moreover, the multi-axial patterning was linked to spatio-temporal activation of *Hox* gene clusters¹⁸, a phenomenon which is conserved across many species¹⁹.

Such self-organization potential of mESCs, in the absence of any extraembryonic tissue, was remarkably similar to developing post-occipital region of the mouse embryo (**Fig. 1b, 2b**). However, *gastruloids* failed to form any tissues corresponding to the brain regions.

Mechanical forces and extracellular matrix composition have significant influence on the developing mouse embryo²⁰⁻²². So far, embryoid bodies and *gastruloids* have disregarded this aspect in the context of recapitulating early embryonic development. When mESCs were differentiated towards epiblast-like cells and cultured on geometrically confined laminin-coated substrates, they demonstrated radial patterning to generate germ layers corresponding to ectoderm, mesoderm and endoderm²³ (**Fig. 1c, 2c**). Similar radial patterning of germ layers was observed when mESCs were differentiated in three-dimensional fibrin gels in a stiffness dependent manner²⁴ (**Fig. 1d, 2d**). Change of extracellular matrix to a more biomimetic but less defined Matrigel resulted in formation of epithelialized and cavitated cysts that morphologically resembled post-implantation epiblast^{25,26} (**Fig. 1e, 2e**). The interaction of cells with extracellular matrix was shown to be dependent on β -1 integrin signaling which was previously described in mouse embryos^{27,28}. Yet, these structures failed to undergo axial morphogenesis, suggesting that culture conditions allowing epiblast-like cyst formation were not permissive for further development.

The epiblast is the domain that forms the embryo proper. However, contribution from extraembryonic tissues is required since development is halted in the absence of extraembryonic tissues^{29,30}. Studies accounting for this necessity have therefore established hybrid embryoid models, combining embryonic stem cells with trophoblast stem cells (TSCs) and/or extraembryonic endoderm cells (XENs)³¹⁻³⁵. Among these, *blastoids* aimed to recapitulate pre-implantation mouse embryonic development by combination of mESCs and TSCs in agarose microwell arrays³¹. When the cells are seeded at optimal numbers, the resulting structures cavitated to exhibit a group of mESC-derived cells on the inside, surrounded by TSC-derived cells on the outside, resembling inner cell mass (ICM) and trophectoderm of E3.5 blastocysts, respectively (**Fig. 1f, 2f**). Although *blastoids* could induce decidualization when transplanted in mouse uterus, they failed to develop further. Recent attempts are exploring ways to prolong *blastoid* culture until gastrulation stages with the induction of extraembryonic endoderm cells within differentiating mESCs³².

Other hybrid embryoid approaches aimed to model post-implantation development. When mESCs and TSCs are combined in three-dimensional Matrigel, they came together to form structures that morphologically similar to pre-gastrulation stage embryos. The hybrid *ETS-*

embryos demonstrated pro-amniotic cavity formation and symmetry breaking³³ (**Fig. 1g, 2g**), however, the occurrence frequency of these structures was relatively low, owing to the incidental nature of the culture system. A more recent version used an aggregation-based strategy to combine mESCs, TSCs and XENs. Resulting structures, termed *ETX embryos*³⁴ (**Fig. 1h, 2h**), did not require extracellular matrix input for cavitation, as ESC-XEN interaction allowed epiblast polarization and epithelialization. Moreover, ETX-embryos demonstrated formation of anterior visceral endoderm-like and primordial germ cell-like cells that resembled E6.5 embryos. Assembly of these three cell types on a shaker platform resulted in formation of similar structures that could initiate decidualization upon transplantation in pseudo-pregnant mouse uterus³⁵. However, in both approaches, formation of *ETX-embryos* was infrequent and there were no signs of axial morphogenesis.

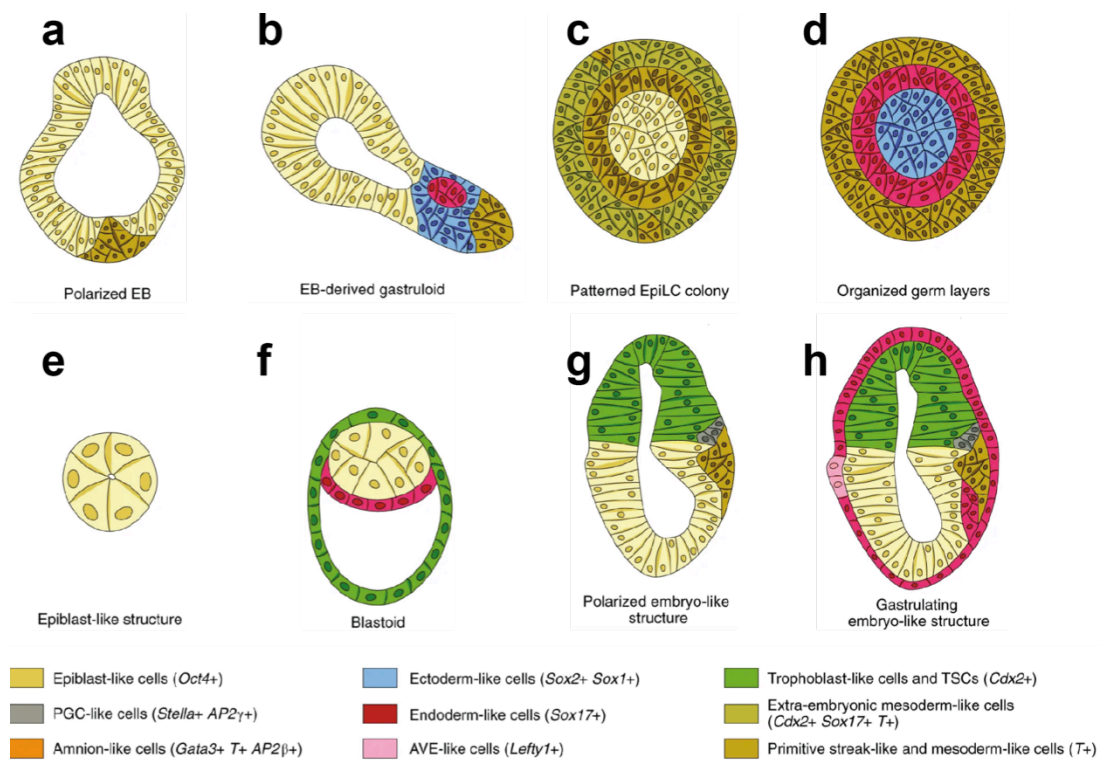


Figure 1: Schematic representation of current *in vitro* models of mouse embryonic development. Figure was reproduced from³⁶.

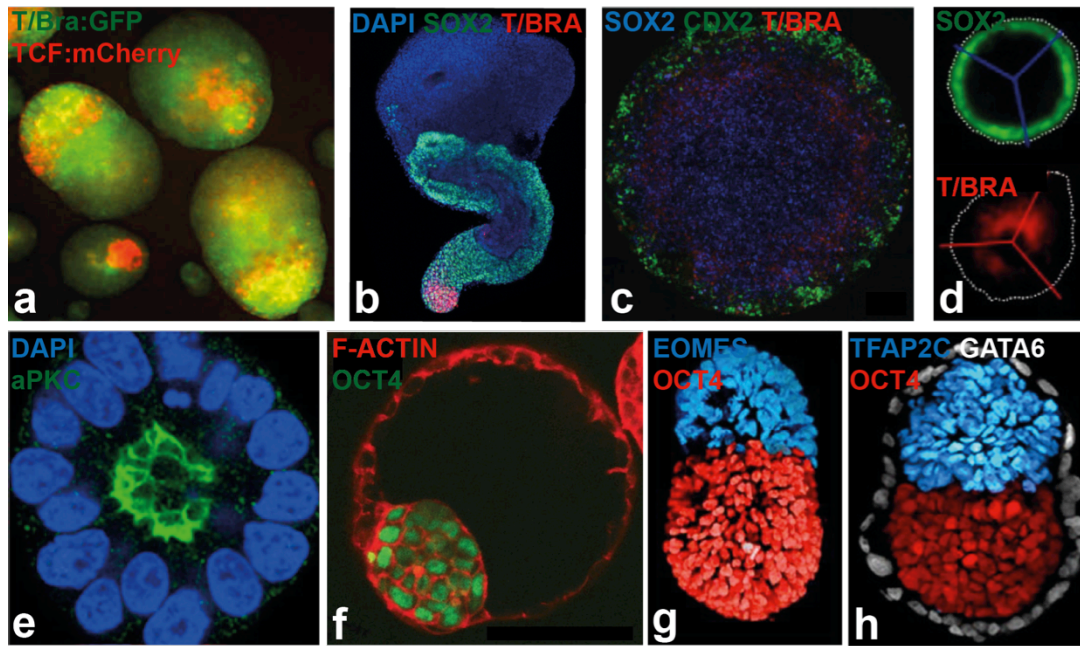


Figure 2: Representative images of *in vitro* models described. Images were reproduced from: **a)**³⁷, **b)**¹⁸, **c)**²³, **d)**²⁴, **e)**²⁵, **f)**³¹, **g)**³³, **h)**³⁴.

Altogether, the efforts described so far were aiming to recapitulate early mouse pre- or post-implantation embryonic development with a potential of direct comparison to the real embryo. However, such direct comparison does not apply with human embryos. Currently, it is legally not possible to culture human embryos beyond 14 days^{38,39}. Therefore, *in vitro* models of early human development promise a vast potential.

When human ESCs were embedded in three-dimensional Matrigel, just like mESCs, they formed cavitated cysts and further exhibited symmetry breaking to demonstrate antero-posterior axis determination and limited signs of epithelial-to-mesenchymal transition (EMT)⁴⁰ (**Fig. 3a**). A more controlled model of human epiblast used microfluidic tools to establish patterning along amnion-epiblast axis⁴¹(**Fig. 3b**). The epiblast cells in this model showed extensive migratory behavior, suggesting a better recapitulation of gastrulation and EMT. A different approach explored culture of human ESCs on geometrically confined substrates. When treated with BMP4, human ESCs on these micropatterns demonstrated radial patterning of germ layer markers: ectoderm on the inside, surrounded by a mesoderm ring and endoderm on the outside⁴²(**Fig. 3c**). Remarkably, trophoblast-like cells could also be generated within these self-organizing tissues. The diameter of the micropatterns was identified as an important regulator for the extent of cell fate patterning. More recent bioengineering advancements could build on the micropattern system by providing gradients of signaling molecules to be able to control the symmetry breaking and cell fate patterning⁴³

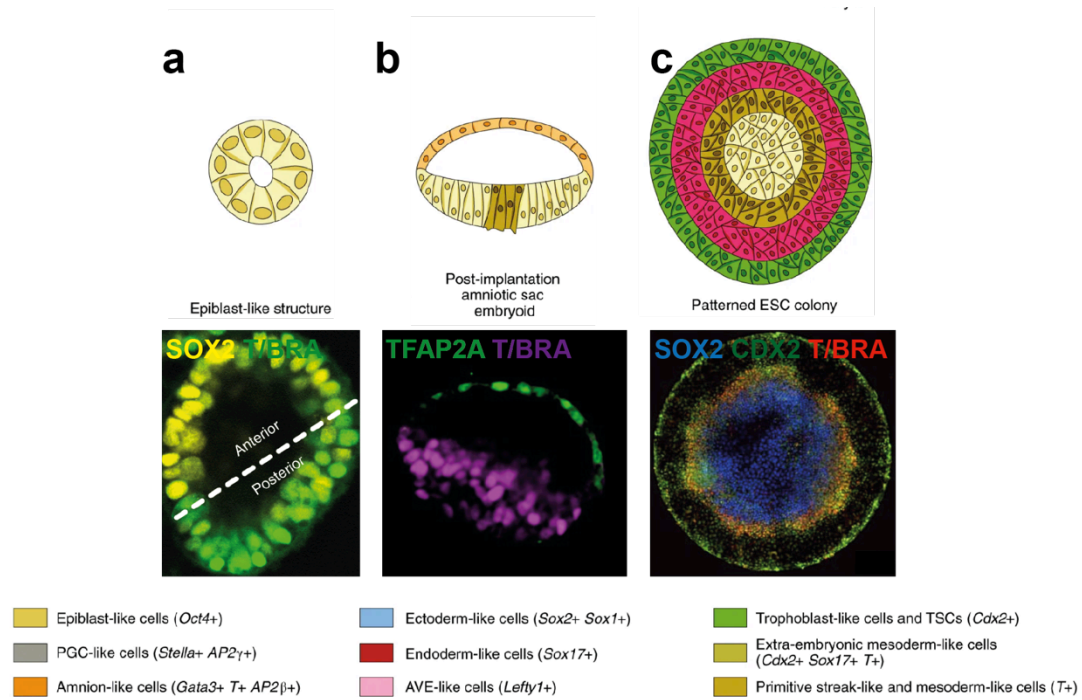


Figure 3: Schematic representation of current *in vitro* models of human embryonic development (top panel). Figure was reproduced from³⁶. Representative images of *in vitro* models described (bottom pane). Images were reproduced from: **a)**⁴⁰, **b)**⁴¹, **c)**⁴².

For decades, scientists have been trying to understand the mechanisms that govern mouse and human embryonic development. Pioneering work relied on gene editing strategies (i.e. loss of function, gain of function, cell tracing) to identify the roles of genes in the developing model organisms. Although these methods were definitive, the scalability and labor-intensive nature of *in vivo* biology prompted scientists to look for new avenues. The newly emerging field of synthetic embryology is now taking a different approach than the traditional developmental biology; by deconstructing the embryo into simplified pieces, in order to conduct large-scale studies with easier accessibility than the embryos. The methodologies described above are paving the way towards establishing *in vitro* simplified embryo-like structures. The future holds great promise for the application of such models for potential embryotoxicity and drug screening assays or generation of transplantable cells types that are not possible to generate with conventional differentiation approaches.

Objective and Aims

By combining insights from developmental biology and advanced bioengineering methodologies, the overarching goal of this PhD thesis is to develop a set of innovative *in vitro* mouse embryonic stem cell (ESC)-based models for the study of post-implantation mouse development. A specific focus will be on overcoming key limitations of previous *in vitro* models, such as the absence of anterior neural tissues in mouse *gastruloids*. The application of these new tools should open up exciting perspectives for the study of early mouse development, with implications for future applications of *in vitro* stem cell culture technology in drug testing and disease modeling.

Aim 1: To improve and extend *gastruloid* culture towards embryo-like multi-axial patterning. The culture of conventional *gastruloids* is limited to 120 hours, hampering exploration of later, more advanced developmental stages such as the establishment of the body plan through the spatiotemporally orchestrated expression of Hox gene clusters. Here, I will aim at improving the existing *gastruloid* culture methodology to prolong *gastruloid* lifespan up to at least one week (168 hours). I will characterize the multi-axial patterning potential and the establishment of Hox gene transcription program in the advanced *gastruloids*.

Aim 2: To generate ‘artificial epiblasts’ for the formation of *gastruloids* bearing anterior neural tissues. Existing *gastruloids* do not form any anterior neural regions. To overcome this limitation, I will establish a new culture system by *i)* modifying the medium composition with regards to key developmental signaling factors, and *ii)* devise a high-throughput mouse ESC aggregation platform to generate epiblast-like (EPI) aggregates as a starting entity for subsequent *gastruloid* formation. I will characterize to which extent such EPI aggregates can undergo axial elongation and give rise to anterior neural tissues.

Aim 3: To combine embryonic and extraembryonic stem cell aggregates for the generation of embryoids with axial patterning potential. The mouse epiblast develops in conjunction with extraembryonic ectoderm. *Gastruloids* and EPI aggregates do not contain any extraembryonic tissue. I will thus combine EPI aggregates with aggregates of trophoblast stem cells and assess the potential of these hybrid structures to undergo gastrulation-like processes. In particular, I will explore the propensity of these novel embryoids to undergo axial elongation and form anterior brain-like domains.

References

1. STEVENS, L. C. Embryology of testicular teratomas in strain 129 mice. *J. Natl. Cancer Inst.* **23**, 1249–1295 (1959).
2. PIERCE, G. B., DIXON, F. J. & VERNEY, E. L. Teratocarcinogenic and tissue-forming potentials of the cell types comprising neoplastic embryoid bodies. *Lab. Invest.* **9**, 583–602 (1960).
3. PIERCE, G. B. & DIXON, F. J. Testicular teratomas. II. Teratocarcinoma as an ascitic tumor. *Cancer* **12**, 584–589 (1959).
4. STEVENS, L. C. Embryonic potency of embryoid bodies derived from a transplantable testicular teratoma of the mouse. *Developmental Biology* **2**, 285–297 (1960).
5. KLEINSMITH, L. J. & PIERCE, G. B. MULTIPOTENTIALITY OF SINGLE EMBRYONAL CARCINOMA CELLS. *Cancer Res.* **24**, 1544–1551 (1964).
6. Martin, G. R. & Evans, M. J. Differentiation of clonal lines of teratocarcinoma cells: formation of embryoid bodies in vitro. *Proceedings of the National Academy of Sciences* **72**, 1441–1445 (1975).
7. Martin, G. R. & Evans, M. J. Multiple differentiation of clonal teratocarcinoma stem cells following embryoid body formation in vitro. *Cell* **6**, 467–474 (1975).
8. Evans, M. J. & Kaufman, M. H. Establishment in culture of pluripotential cells from mouse embryos. *Nature* **292**, 154–156 (1981).
9. Martin, G. R. Isolation of a pluripotent cell line from early mouse embryos cultured in medium conditioned by teratocarcinoma stem cells. *Proceedings of the National Academy of Sciences* **78**, 7634–7638 (1981).
10. Doetschman, T. C., Eistetter, H., Katz, M., Schmidt, W. & Kemler, R. The in vitro development of blastocyst-derived embryonic stem cell lines: formation of visceral yolk sac, blood islands and myocardium. *J Embryol Exp Morphol* **87**, 27–45 (1985).
11. Bain, G., Kitchens, D., Yao, M., Huettner, J. E. & Gottlieb, D. I. Embryonic Stem Cells Express Neuronal Properties in Vitro. *Developmental Biology* **168**, 342–357 (1995).
12. Kubo, A. *et al.* Development of definitive endoderm from embryonic stem cells in culture. *Development* **131**, 1651–1662 (2004).
13. Boheler, K. R. *et al.* Differentiation of pluripotent embryonic stem cells into cardiomyocytes. *Circ. Res.* **91**, 189–201 (2002).
14. Berge, ten, D. *et al.* Wnt Signaling Mediates Self-Organization and Axis Formation in Embryoid Bodies. *Stem Cell* **3**, 508–518 (2008).

15. Marikawa, Y., Tamashiro, D. A. A., Fujita, T. C. & Alarcón, V. B. Aggregated P19 mouse embryonal carcinoma cells as a simple in vitro model to study the molecular regulations of mesoderm formation and axial elongation morphogenesis. *Genesis* **47**, 93–106 (2009).
16. van den Brink, S. C. *et al.* Symmetry breaking, germ layer specification and axial organisation in aggregates of mouse embryonic stem cells. *Development* **141**, 4231–4242 (2014).
17. Turner, D. A. *et al.* Anteroposterior polarity and elongation in the absence of extra-embryonic tissues and of spatially localised signalling in gastruloids: mammalian embryonic organoids. *Development* **144**, 3894–3906 (2017).
18. Beccari, L. *et al.* Multi-axial self-organization properties of mouse embryonic stem cells into gastruloids. *Nature* **562**, 272–276 (2018).
19. Santini, S., Boore, J. L. & Meyer, A. Evolutionary conservation of regulatory elements in vertebrate Hox gene clusters. *Genome Research* **13**, 1111–1122 (2003).
20. Hiramatsu, R. *et al.* External Mechanical Cues Trigger the Establishment of the Anterior-Posterior Axis in Early Mouse Embryos. *Developmental Cell* **27**, 131–144 (2013).
21. Kolahi, K. S. *et al.* Effect of substrate stiffness on early mouse embryo development. *PLoS ONE* **7**, e41717 (2012).
22. Rozario, T. & DeSimone, D. W. The extracellular matrix in development and morphogenesis: A dynamic view. *Developmental Biology* **341**, 126–140 (2010).
23. Morgani, S. M., Metzger, J. J., Nichols, J., Siggia, E. D. & Hadjantonakis, A.-K. Micropattern differentiation of mouse pluripotent stem cells recapitulates embryo regionalized cell fate patterning. *Elife* **7**, 1040 (2018).
24. Poh, Y.-C. *et al.* Generation of organized germ layers from a single mouse embryonic stem cell. *Nature Communications* **5**, 4000–12 (2014).
25. Bedzhov, I. & Zernicka-Goetz, M. Self-Organizing Properties of Mouse Pluripotent Cells Initiate Morphogenesis upon Implantation. *Cell* **156**, 1032–1044 (2014).
26. Shahbazi, M. N. *et al.* Pluripotent state transitions coordinate morphogenesis in mouse and human embryos. *Nature* **552**, 239–243 (2017).
27. Stephens, L. E. *et al.* Deletion of beta 1 integrins in mice results in inner cell mass failure and peri-implantation lethality. *Genes & Development* **9**, 1883–1895 (1995).

28. Miner, J. H., Li, C., Mudd, J. L., Go, G. & Sutherland, A. E. Compositional and structural requirements for laminin and basement membranes during mouse embryo implantation and gastrulation. *Development* **131**, 2247–2256 (2004).
29. Donnison, M. *et al.* Loss of the extraembryonic ectoderm in Elf5 mutants leads to defects in embryonic patterning. *Development* **132**, 2299–2308 (2005).
30. Rodriguez, T. A., Srinivas, S., Clements, M. P., Smith, J. C. & Beddington, R. S. P. Induction and migration of the anterior visceral endoderm is regulated by the extra-embryonic ectoderm. *Development* **132**, 2513–2520 (2005).
31. Rivron, N. C. *et al.* Blastocyst-like structures generated solely from stem cells. *Nature* **557**, 106–111 (2018).
32. Vrij, E. J. *et al.* Chemically-defined induction of a primitive endoderm and epiblast-like niche supports post-implantation progression from blastoids. *bioRxiv* **120**, 510396 (2019).
33. Harrison, S. E., Sozen, B., Christodoulou, N., Kyprianou, C. & Zernicka-Goetz, M. Assembly of embryonic and extraembryonic stem cells to mimic embryogenesis in vitro. *Science* **356**, eaal1810 (2017).
34. Sozen, B. *et al.* Self-assembly of embryonic and two extra-embryonic stem cell types into gastrulating embryo-like structures. *Nature Cell Biology* **20**, 979–989 (2018).
35. Zhang, S. *et al.* Implantation initiation of self-assembled embryo-like structures generated using three types of mouse blastocyst-derived stem cells. *Nature Communications* **10**, 1–17 (2019).
36. Shahbazi, M. N. & Zernicka-Goetz, M. Deconstructing and reconstructing the mouse and human early embryo. *Nature Cell Biology* **20**, 878–887 (2018).
37. Berge, ten, D. *et al.* Wnt signaling mediates self-organization and axis formation in embryoid bodies. *Cell Stem Cell* **3**, 508–518 (2008).
38. Deglincerti, A. *et al.* Self-organization of the in vitro attached human embryo. *Nature* **533**, 251–254 (2016).
39. Shahbazi, M. N. *et al.* Self-organization of the human embryo in the absence of maternal tissues. *Nature Cell Biology* **18**, 700–708 (2016).
40. Simunovic, M. *et al.* A 3D model of a human epiblast reveals BMP4-driven symmetry breaking. *Nature Cell Biology* **21**, 900–910 (2019).
41. Zheng, Y. *et al.* Controlled modelling of human epiblast and amnion development using stem cells. *Nature* **573**, 421–425 (2019).

42. Warmflash, A., Sorre, B., Etoc, F., Siggia, E. D. & Brivanlou, A. H. A method to recapitulate early embryonic spatial patterning in human embryonic stem cells. *Nat. Methods* **11**, 847–854 (2014).
43. Manfrin, A. *et al.* Engineered signaling centers for the spatially controlled patterning of human pluripotent stem cells. *Nat. Methods* **16**, 640–648 (2019).

CHAPTER II

MULTI-AXIAL SELF-ORGANISATION PROPERTIES OF MOUSE EMBRYONIC STEM CELLS INTO GASTRULOIDS

MULTI-AXIAL SELF-ORGANISATION PROPERTIES OF MOUSE EMBRYONIC STEM CELLS INTO GASTRULOIDS

Leonardo Beccari^{1*}, Naomi Moris^{2*}, Mehmet Girgin^{3*}, David A. Turner², Peter Baillie-Johnson^{2,4}, Anne-Catherine Cossy³, Matthias P. Lutolf³,
Denis Duboule^{1,3} ¶ and Alfonso Martinez Arias². ¶

¹Department of Genetics and Evolution, University of Geneva, Geneva, Switzerland.

²Department of Genetics, University of Cambridge, Cambridge, UK.

³School of Life Sciences, Federal Institute of Technology EPFL, Lausanne, Switzerland.

⁴Current address: Wellcome Trust-Medical Research Council Cambridge Stem Cell Institute,
University of Cambridge, UK.

*Shared first authorship, ¶Shared last authorship

Correspondence to: Alfonso Martinez-Arias (ama11@hermes.cam.ac.uk) and Denis Duboule
(denis.duboule@epfl.ch)

Author contribution: M.G established extended gastruloid culture protocol, performed immunostaining and confocal imaging on gastruloids and produced figures.

Post-print version of the article published in Nature can be found at: Beccari, L. et al. Multi-axial self-organization properties of mouse embryonic stem cells into gastruloids. Nature 562, 272–276 (2018). <https://doi.org/10.1038/s41586-018-0578-0>.

Abstract

The emergence of multiple axes is an essential element in the establishment of the mammalian body plan. This process takes place shortly after implantation of the embryo within the uterus and relies on the activity of gene regulatory networks that coordinate transcription in space and time. Whereas genetic approaches have revealed important aspects of these processes¹, a mechanistic understanding is hampered by the poor experimental accessibility of early post-implantation stages. Here we show that small aggregates of mouse embryonic stem cells (ESCs), when stimulated to undergo gastrulation-like events and elongation in vitro, can organize a post-occipital pattern of neural, mesodermal and endodermal derivatives that mimic embryonic spatial and temporal gene expression. The establishment of the three major body axes in these ‘gastruloids’^{2,3} suggests that the mechanisms involved are interdependent. Specifically, gastruloids display the hallmarks of axial gene regulatory systems as exemplified by the implementation of collinear Hox transcriptional patterns along an extending anteroposterior axis. These results reveal an unanticipated self-organizing capacity of aggregated ESCs and suggest that gastruloids could be used as a complementary system to study early developmental events in the mammalian embryo.

Results and Discussion

Recent work on organoids derived from stem cells has revealed a surprising autonomy in the development of particular tissues and organs^{4,5}. When around 250 ESCs are aggregated, given a pulse of the Wnt agonist CHIR99021 (Chi) between 48 and 72 h after the start of culture, and returned to N2B27 medium (Fig. 1a), a pole of *Bra* (brachyury, also known as *T*) expression emerges reproducibly⁶ (Fig. 1b, Extended Data Fig. 1), resembling the elongating embryonic tail bud. The aggregates continue to elongate up to 120 h after aggregation (AA), when they display a ‘rostral’ cell-dense region and a polar extension towards a ‘caudal’ extremity, reaching up to 500 μm in size (Fig. 1b). Shaking the culture enables aggregates to grow to 850–1,000 μm in length at 168 h AA (Fig. 1c, d). At 120 h AA, a *Gata6*-positive domain is visible opposite to a *Bra* and *Cdx2*-expressing region, probably corresponding to the cardiac crescent, which delimits the embryonic post-occipital region⁷ (Fig. 1b–d, Extended Data Fig. 1). By contrast, at 120–168 h AA *Sox1/Sox2*-positive cells are localized centrally, with the exception of those at the rostral extremity (Fig. 1c, d).

To characterize the transcriptional programmes of these gastruloids, we carried out RNA-sequencing (RNA-seq) analysis on duplicate pools of gastruloids and compared their profiles with those of developing mouse embryos from E6.5 to E9.5. Because gastruloids display hallmarks of post-occipital embryos⁶ (Fig. 1b–d) we excluded the anterior portion of E7.5–E9.5 embryos (Fig. 1e, left). Principal component analysis (PCA) demonstrated reproducibility between samples and a clear clustering along principal component 1 (PC1) corresponding to their temporal order (Fig. 1e), whereas embryo samples segregated from gastruloids along PC2 only.

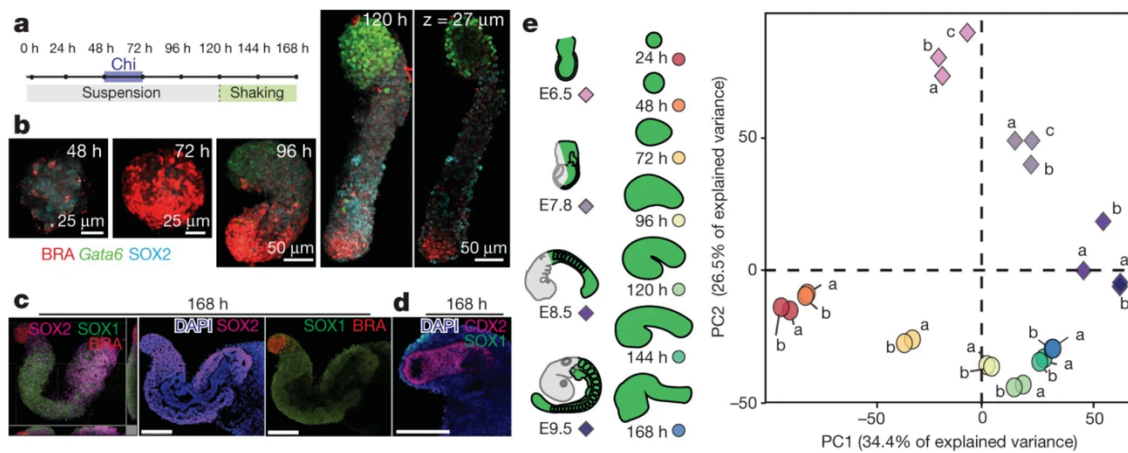


Figure 1: Elongation of Gastruloids. **a)** Schematic of the culture protocol: 200–300 ESCs were allowed to aggregate; the Wnt agonist CHIR99201 (Chi) was added between 48 h and 72 h AA; gastruloids were cultured in suspension until 120 h AA (grey rectangle) and transferred into shaking cultures until 168 h AA. **b)** Three-dimensional renderings and confocal sections of gastruloids at different times showing the elongation and expression of BRA, SOX2 and Gata6H2B-Venus (green). The right-most panel is a confocal section of the 3D rendering of the neighbouring 120 h AA gastruloid. Scale bars, 25 μ m (48 h, 72 h), 50 μ m (96 h, 120 h). Each image is representative of an experiment with seven biological replicates showing the same expression pattern. **c,d)** Three-dimensional rendering (**c**, left) and confocal sections (**c**, centre, right and **d**, tail region) of gastruloids at 168 h AA, showing the localization of CDX2, SOX2, SOX1 and BRA proteins. Scale bar, 150 μ m. Each image is representative of an experiment performed in 20 biological replicates. The reported expression pattern was observed in at least 80% of the cases. **e)** PCA analysis of RNA-seq datasets using time-pooled gastruloids from 24 to 168 h AA ($n = 2$ replicates per time point) and pooled mouse embryos at E6.5 ($n = 3$), E7.8 ($n = 3$), E8.5 (12–14 somites, $n = 2$ replicates) and E9.5 (~24 somites, $n = 2$ replicates). Each replicate was derived from an independent sample. For E7.8 embryos, only their posterior half was used. For E8.5 and E9.5, the post-occipital embryonic domain was dissected. In all cases, the portion used for RNA extraction is coloured in pale green. All autosomal genes were considered for this analysis. PC1 shows a strong temporal component whereas PC2 discriminates between gastruloids or embryonic samples.

The main (top 100) clustering determinants of gastruloid samples included several pluripotency-related genes, epiblast markers and genes involved in gastrulation. They also comprised different *Hox* genes and other transcription factors usually expressed in post-occipital structures of the developing mouse embryo such as *Cdx1*, *Cdx2*, *Meis1*, *Meis2*, *Meox1*, *Bra* and *Gata4* (Fig. 2a). Twenty-five of these 100 PCA determinants were identified independently in both gastruloid and embryonic temporal series (Fig. 2a, genes in red), supporting the idea that gastruloids and embryos elongate by implementing similar transcriptional programs. The analysis of specific genes associated with particular developmental landmarks confirmed this point (Fig. 2b, Extended Data Fig. 2a, b). For instance, genes associated with gastrulation, such as *Mixl1*, *Eomes*, *Gsc* (goosecoid) or *Chrd* (chordin) were transiently and orderly transcribed at around 48 h AA (Fig. 2b, Extended Data Fig. 2b), suggesting that at this stage the gastruloid transcriptome resembles that of mouse epiblast at the onset of gastrulation. By 72 h AA, we observed an increase in the complexity of gene-expression profiles, with the appearance of markers for different embryonic lineages, including mesendoderm and neuroectoderm, and the transcription of *Hox* gene clusters (Fig. 2a, b, Extended Data Fig. 2a, b; see below). Genes associated with either extra-embryonic structures or anterior neural plate derivatives were not (or were poorly) expressed in gastruloids (Fig. 2b).

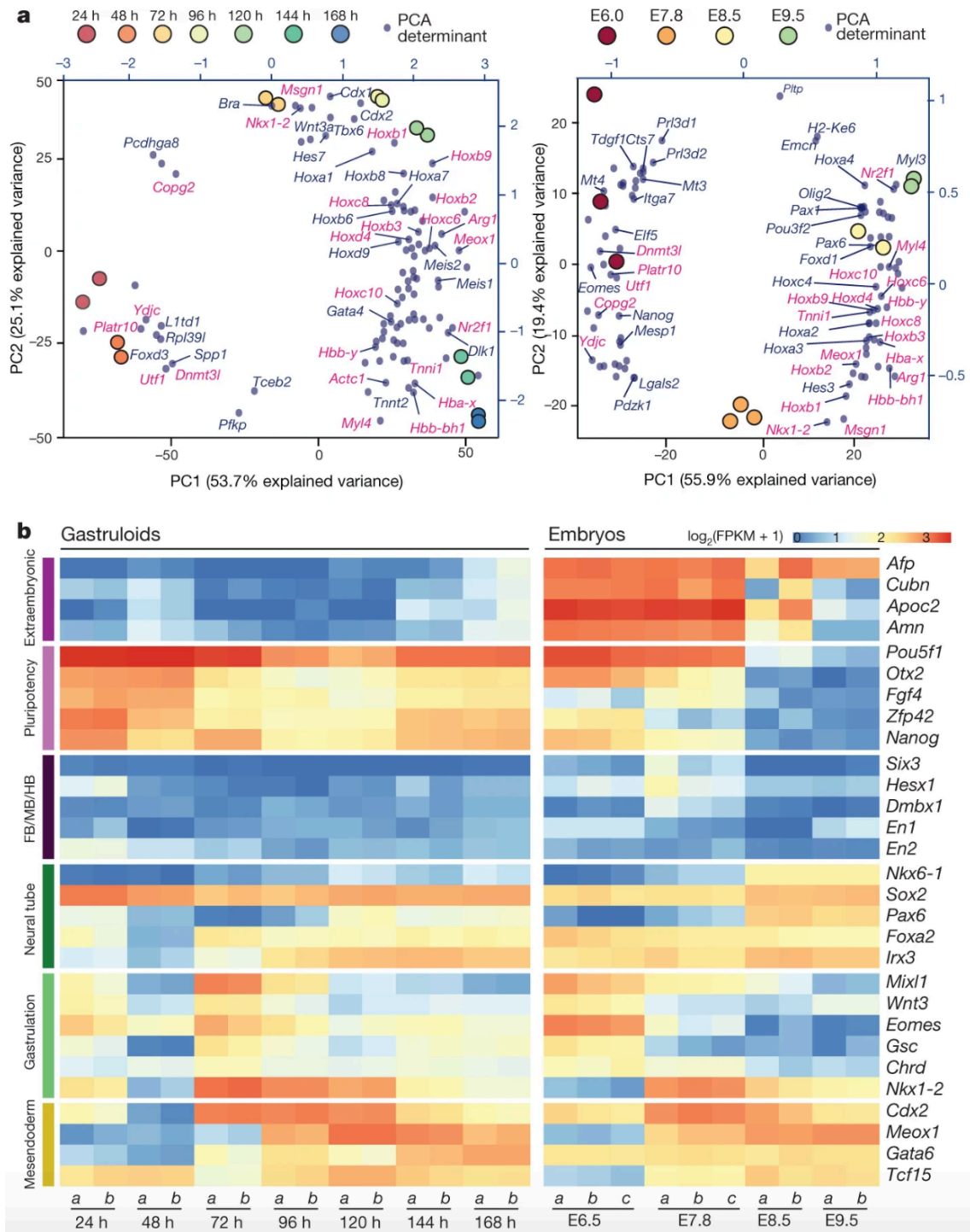


Fig. 2: Temporal patterns of gene expression in gastruloids. **a)** PCA of either pooled gastruloids during temporal progression from 24 h to 168 h AA (left) or mouse embryos from E6.5 to E9.5 (right). The 100 top contributing genes to the first two principal components are labelled, with those common to both gastruloid and embryo datasets in red. *Tceb2* is also known as *Elob*. **b)** Heat map of scaled expression of genes associated with development of different embryonic structures in pooled gastruloids and embryos over time. The replicates represented in these graphs were derived from biologically independent samples, as in Fig. 1e. FB, forebrain; MB, midbrain; HB, hindbrain.

PCA analysis using single gastruloids revealed robust clustering at all assessed developmental stages and a correspondence with the pooled RNA-seq datasets (Extended Data Fig. 2c), showing that the population of gastruloids was comparatively homogenous at the time points analysed, and hence that the pooled RNA-seq datasets reflected the transcriptional status of single gastruloids. Transcriptome analyses of gastruloids revealed mRNAs that are usually associated with neural, endodermal and mesodermal derivatives, including paraxial, cardiac, intermediate and haematopoietic progenitors as well as neural crest (for example, see ref.⁸) (Fig. 2b, Extended Data Figs. 2b, 3). We also observed an antero-posterior pattern of differentiation along these lineages, reminiscent of the pattern in the embryo. For example, the sequential expression of *Bra–Msgn1–Meox1–Tcf15* recapitulates the spatio-temporal differentiation pattern of paraxial mesoderm⁹ (Extended Data Fig. 3a, b). Genes associated with spinal cord development (Extended Data Fig. 3c, d), such as *Irx3*, *Sox1*, *Sox2* and *Lfng* (lunatic fringe) were expressed in a continuous domain along the extension of the gastruloid. Within this domain, *Hes5* and *Dll1* (marking different neural progenitors) were strongly expressed, whereas terminally differentiating cells (*Phox2a/Mnx1*-positive) formed an apparent anterior-to-posterior density gradient and were almost completely absent from the posterior-most aspect (Extended Data Fig. 3c, d), reflecting the organization in the embryo¹⁰. Nevertheless, these ordered patterns of gene expression did not correlate with any precise morphogenesis. For example, neural progenitors did not properly form a neural tube (Fig. 3, Extended Data Figs. 3d, 4a–c), even though sporadic tubular structures were observed (Extended Data Fig. 4a (white arrowheads), c (right)). We observed clumps of cells positive for either SOX1 and OLIG2, SOX1 and PAX3, or SOX1 and PAX7, indicative of dorsal and ventral neural tube progenitors¹¹ (Extended Data Fig. 4d); however, they lacked a clear segregation along the dorso-ventral extension of the SOX1 domain. Similarly, *Tcf15*-expressing cells did not condense into somites (Extended Data Fig. 3b).

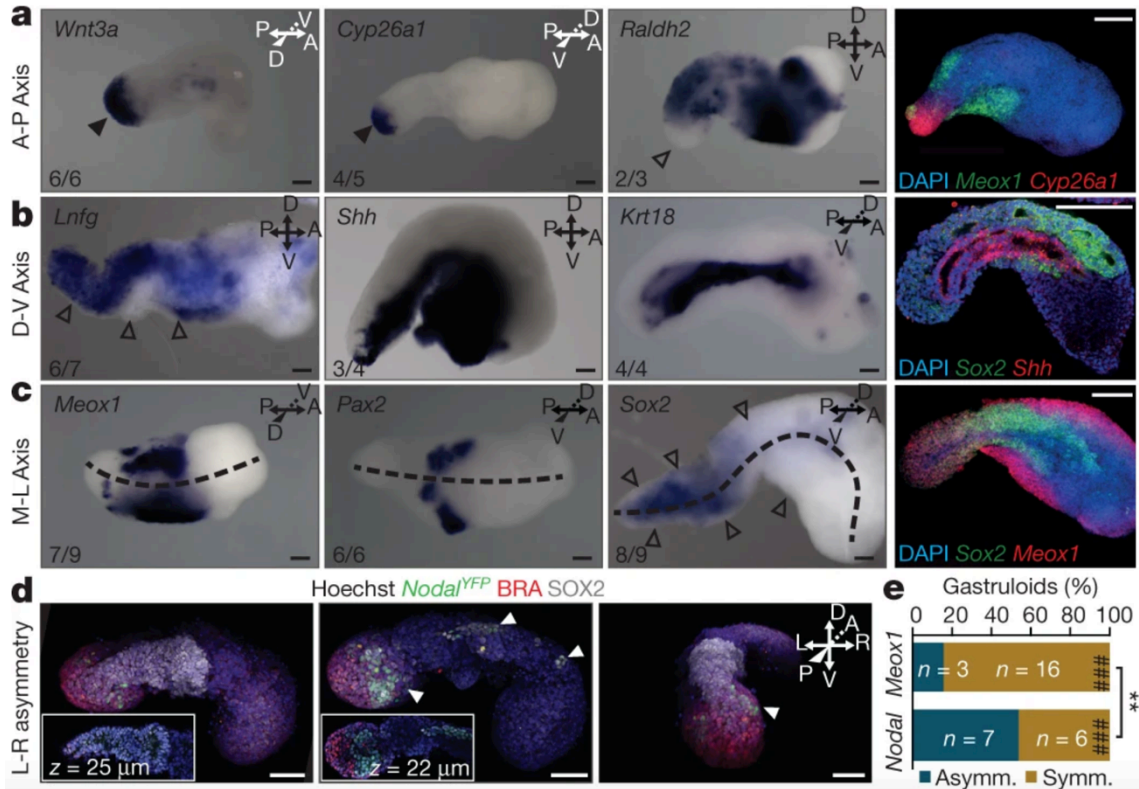


Fig. 3: Multi-axial organization of gastruloids. a–c, Gene expression in gastruloids at 144 h AA, showing their axial organization. **a**, *Wnt3a* and *Cyp26a1* expression (arrowhead) at the posterior end, where *Raldh2* is not transcribed (empty arrowhead). Double-fluorescence in situ hybridization (FISH) staining of *Meox1* and *Cyp26a1* (**a**, far right). **b**, Dorso-ventral axis revealed by the ventral expression of *Shh* and *Krt18*, and of *Lnfg* dorsally (empty arrowheads mark the ventral *Lnfg*-negative domain). Double FISH staining of *Sox2* and *Shh* confirms a dorso-ventral segregation, with *Shh* expressed exclusively in endoderm precursors (**b**, far right). **c**, Medio-lateral axis of symmetry (dotted line) revealed by the bilateral expression of *Meox1* and *Pax2*, complementary to the central distribution of *Sox2* transcripts (empty arrowheads). For each gene, the proportion of gastruloids exhibiting the reported pattern is shown. Scale bar, 100 μ m. A, anterior; P, posterior; D, dorsal; V, ventral. **d**, Three-dimensional renderings of confocal stacks of 120 h AA gastruloids containing a *Nodal*YFP reporter gene, stained for SOX2 (white) and BRA (red) proteins and imaged from the dorsal (left), ventral (middle) and posterior (right) side of the gastruloid; insets show a confocal section of the posterior region. Reporter-gene expression within the Bra-expressing domain on the ventral surface is suggestive of a node-like structure (middle; Extended Data Fig. 6). Additional expression of *Nodal* in a bilaterally asymmetric cluster of cells (white arrowheads) is reminiscent of the asymmetric *Nodal* expression in the embryo. Data are representative of two independent experiments with similar results (n = 13). Additional samples are shown in Extended Data Fig. 6e. L, left; R, right. Scale bar, 30 μ m. **e**, Bar graph showing the frequency distribution of asymmetric and symmetric expression of *Nodal* or *Meox1* in 120 h AA gastruloids. At this stage, *Nodal* expression was significantly less symmetrical than *Meox1* expression, suggesting that gastruloids may also implement the start of left-right asymmetry. **P < 0.0001. The hybrid Wilson/Brown method was used to calculate the confidence intervals.

Analysis of different endodermal markers revealed temporal dynamics that were also reminiscent of those in the embryo¹² (Extended Data Figs. 3e, f, 4e, f). Transcripts of *Gsc* and *Cdx2*, markers of definitive endoderm^{13,14}, were upregulated soon after Chi induction (72 h AA), followed by upregulation of *Cer1* (cerberus) (96–120 h AA) and subsequently *Sorcs2*, *Pax9* or *Shh* (120–144 h AA). All assayed endoderm-expressed genes were active in the ventral-like domain of gastruloids (Extended Data Figs. 3f, 4e, f), resembling expression in the embryo. In a majority of cases, gut-endoderm progenitors appeared as a continuous tubular

structure (Extended Data Fig. 4a, e, f; red arrowheads), often spanning the entire antero-posterior extension, reminiscent of an embryonic digestive tract. We next investigated this unanticipated level of organization and capacity to self-organize an integrated axial system by assessing the expression of genes associated with the developing embryonic axes (Fig. 3). Transcripts of *Wnt3a* and *Cyp26a1* were detected at the caudal extremity of gastruloids, similar to those of *Bra* and *Cdx2* (compare Fig. 3a and Extended Data Fig. 5a with Fig. 1c, d and Extended Data Figs. 3b, 4f), and complementary to the localization of *Raldh2* (also known as *Aldh1a2*) mRNAs (Fig. 3a)—further supporting the existence of an antero-posterior axis. This was also supported by the spatial segregation of the presomitic mesoderm-like domain (marked by *Cyp26a1*) and the *Meox1* somitic mesoderm (Fig. 3a (right), Extended Data Fig. 5a). On the other hand, *Lfng*, *Sox1* and *Sox2* were transcribed in a central and dorsal domain at 144 h AA (Fig. 3b, Extended Data Figs. 3d, 4a), in a complementary fashion to the ventrally located intestinal tract markers (Fig. 3b, Extended Data Figs. 3d, 4e, f, 5b). Additional signs of multi-axial organization were provided by the expression of mesoderm-specific genes *Osr1*, *Pecam1*, *Meox1* and *Pax2* in a medio-lateral symmetry flanking the centrally located *Sox2*-positive domain (Fig. 3c, Extended Data Fig. 3b). Double staining of *Sox2* and *Meox1* (Fig. 3c (right), Extended Data Fig. 5c) and cross-sections (Extended Data Fig. 4b) confirmed the non-overlapping medio-lateral and dorso-ventral distribution of neural and mesodermal progenitors. *Nodal* expression was confined to a small and compact region on the ventral most posterior aspect at 120 h AA (Extended Data Figs. 6, 7). These *Nodal*-expressing cells displayed high levels of *Cdh1* (also known as E-cadherin) and dense phalloidin staining (Extended Data Fig. 6a, b), suggestive of a node-like identity¹⁵, a hypothesis supported by the presence of *Nodal* mRNA in a domain comparable to that of *Gsc*, *Bra* and *Chrd* at 96 h AA (Extended Data Fig. 6c, d). *Nodal* mRNA in these cells rapidly decreased and was almost undetectable at 144 h AA. However, despite these signs of a node-like structure, we did not observe any notochord derivatives, which usually originate from the node. The downregulation of *Nodal* in the presumptive node-like cells at 120 h AA coincided with the appearance of patches of *Nodal*-expressing cells along the posterior half of extending gastruloids, which were often distributed in an asymmetric manner (Fig. 3d, Extended Data Figs. 6d, e, 7) at 120 h and 144 h AA. *Cer1* also displayed a left-right asymmetric expression, particularly evident at 144 h AA (Extended Data Fig. 6f). This pattern was not observed with *Meox1*, which was predominantly expressed on both sides (Fig. 3d, e.) Together, these data suggest that besides the establishment of a medio-lateral axis, gastruloids may also implement the beginning of left–

right asymmetry. The formation and patterning of post-occipital embryonic territories is associated with the sequential activation of clustered *Hox* genes. Because these genes appeared to be differentially regulated in the RNA-seq time course (Fig. 2a, Extended Data Fig. 2a, b), we assessed whether their sequential activation in time and space¹⁶ was also recapitulated. A pooled PCA analysis using only *Hox* transcripts revealed robust clustering along the time axis (81% variance) and a close correspondence with the dynamic activation of these genes in embryos (Fig. 4a, Extended Data Fig. 8a–c). The variability in *Hox* mRNA content among gastruloids was evaluated using ten individual specimens from three different stages (Extended Data Fig. 9a). Gastruloids at identical time points clustered tightly together based solely on their *Hox* transcripts. Transcript profiles over *Hox* clusters revealed signs of collinear activation, the hallmark of this gene family¹⁷. In E6.5 embryos, some *Hoxa* and *Hoxd* genes are expressed before gastrulation in extra-embryonic tissues¹⁸ (Extended Data Fig. 8a). Between E7 and E9.5, *Hox* genes start to be transcribed in an order that reflects their 3' to 5' position within each cluster (Extended Data Fig. 8a, b). RNA-seq profiling revealed an activation dynamic comparable to that observed in embryos (Fig. 4a, Extended Data Fig. 8c). For instance, whereas *Hoxa* RNA was not detected until 48 h AA, *Hoxa1* to *Hoxa3* expression was robust at 72 h, and was followed by sustained transcription of *Hoxa5*, *Hoxa7* and *Hoxa9* at 96–120 h. *Hoxa10* and *Hoxa11* RNA appeared at 144 h AA, at the same time that *Hoxa1*, *Hoxa2* and *Hoxa3* transcripts started to disappear (Fig. 4b, Extended Data Fig. 8c). Similar dynamics were observed for *Hoxd* genes (Extended Data Fig. 8c–e). The early transcription of 5' *Hoxa/Hoxd* genes (Extended Data Fig. 8a, b) was not observed in gastruloids (Extended Data Figs. 4b, 8c, d), consistent with the absence of extra-embryonic derivatives.

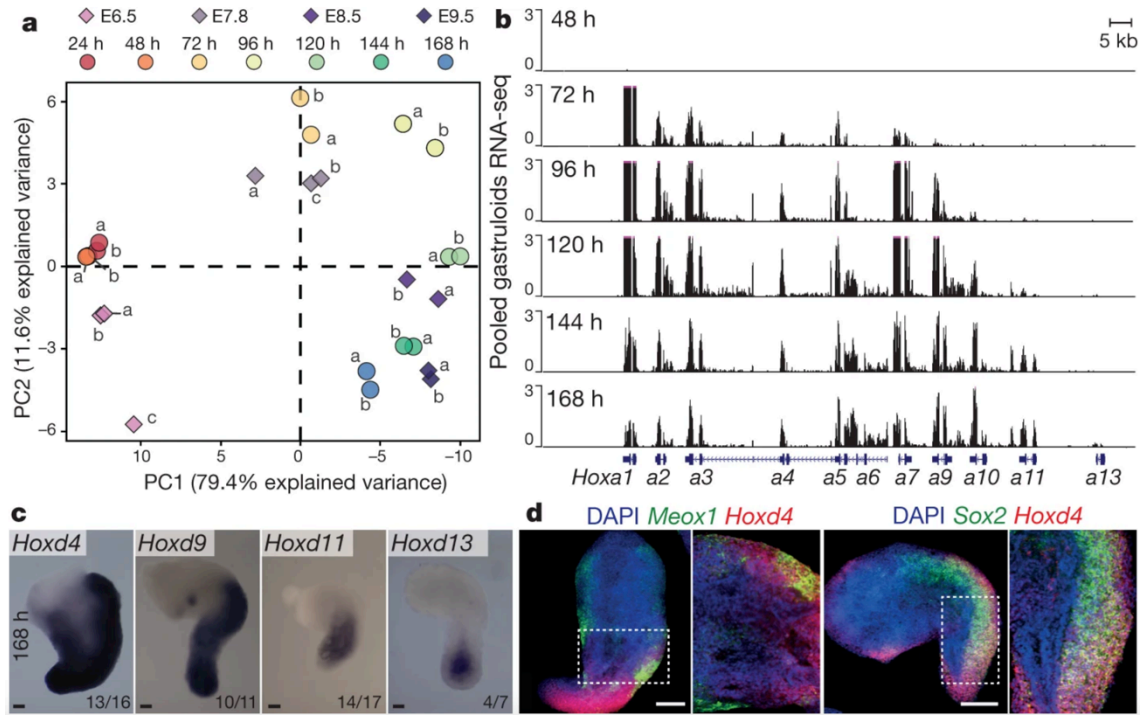


Fig. 4: Collinear *Hox* gene expression in gastruloids. **a)** PCA plot based solely on *Hox* transcripts datasets extracted from pooled gastruloids and embryonic data across time points. For gastruloids, $n = 2$ independent biological replicates per time-point; for E6.5 and E7.8 embryos, $n = 3$ independent biological replicates; For E8.5 and E9.5 embryos, $n = 2$ independent biological replicates. **b)** Transcript profiles over the *HoxA* cluster, using time-sequenced pooled gastruloids. A progressive wave of transcription through *Hoxa* genes is observed between the 72 h and 168 h AA time points. The arrangement of the *Hoxa* cluster is shown schematically below the x axis. **c)** In situ hybridization of 168 h AA gastruloids using probes for various *Hoxd* genes. Expression becomes spatially restricted along the antero-posterior axis in parallel with the respective position of the genes in the cluster. For each gene, the proportion of gastruloids displaying the reported expression pattern is shown in the bottom right corner of the image, expressed as a fraction of the total number of gastruloids analysed. Scale bar, 100 μm . **d)** Double-FISH staining of *Hoxd4* with *Sox2* or *Meox1* (marking the neural and mesodermal precursors, respectively) showed that *Hoxd4* expression colocalized with both markers, suggesting that gastruloids implement both neural and mesodermal *Hoxd* gene expression. The expression patterns are representative of four independent experiments. Scale bar, 200 μm .

Comparable expression profiles were observed when single gastruloids were examined (Extended Data Fig. 9a, b), again revealing the reproducibility of this activation process. In the embryo, this temporal activation is paralleled by a collinear distribution of transcripts in space¹⁷. Likewise, *Hoxa4/Hoxd4* displayed an antero-posterior boundary near the anterior aspect of the gastruloid, whereas *Hoxa9/Hoxd9*, *Hoxa11/Hoxd11* and *Hoxd13* exhibited successively posterior boundaries (Fig. 4c, Extended Data Fig. 9c). Notably, *Hoxd13* transcripts appeared in cells that were located centrally at the posterior extremity, resembling *Hoxd13* expression in the embryonic cloacal area (Fig. 4c). *Hoxa13* expression was also detected at 168 h AA in the posterior aspect, yet rarely (one in 20 gastruloids examined), consistent with the low transcript levels detected in the pooled RNA-seq analysis (Extended Data Fig. 9c). Double staining for *Hoxd4* and either *Sox2* or *Meox1* revealed *Hoxd4* expression in both neural and mesodermal derivatives (Fig. 4d, Extended Data Fig. 5d, e). The implementation in space and time of the

Hox gene network confirmed the surprisingly high level of organization in the processing of gene regulatory networks, particularly given the absence of extra-embryonic components¹⁹. We tested the ability of several induced pluripotent stem cell (iPSC) lines to produce gastruloids (Extended Data Fig. 10), observing a similar elongation process in one of them. Thus, iPSCs can generate gastruloids; yet these gastruloids had reduced elongation rates, particularly between 48 and 96 h AA (Extended Data Fig. 10a, b). The expression dynamics of *Bra* were nevertheless similar to their ESC counterparts (Extended Data Fig. 10c, d) and *Cdx2* and the neural markers *Sox1* and *Sox2* were also expressed as in ESC-derived gastruloids (Extended Data Fig. 10d, compare with Fig. 1b, c). Furthermore, iPSC gastruloids implemented temporal and spatial collinear expression of *Hoxd*, albeit with a delay in the onset of expression and a spatial collinearity that was not as clearly organized as in ESC-derived gastruloids (Extended Data Fig. 9d, e). When compared to single-tissue organoids (for example, see refs.²⁰⁻²³), gastruloids exhibit an integrated structure that can specify all major embryonic axes in a coordinated manner, complementing recent reports in which stem cells were used to recapitulate morphological and transcriptional events of early blastocyst, but not of subsequent embryonic stages^{19,24}. However, the activation of tissue-specific expression patterns in our gastruloids was not paralleled by a clear internal organization of the corresponding embryonic tissue layers. This observation suggests that caution is needed when considering the possibility of a direct causal relationship between transcriptional programs and early morphogenesis. One potential reason for the low level of tissue organization in gastruloids may be the absence of mechanical interactions and constraints that characterize the developing embryonic context²⁵. The autonomy in the patterns of gene expression reported here highlights the potential of gastruloids for studying complex regulatory circuits, particularly during early post-implantation development and the emergence of body axes.

Acknowledgements

We thank members of the Duboule, Lutolf and Martinez-Arias laboratories for sharing material and discussions, J. Deschamps for DNA clones, D. Trono for the *Oct4::GFP* iPSC line, the histology platform and the Gene Expression Core Facility (EPFL) as well as the genomics platform at Geneva University. This work was supported by funds from the BBSRC (No. BB/M023370/1 and BB/P003184/1 to A.M.A.), an NC3Rs David Sainsbury Fellowship (No. NC/P001467/1 to D.A.T.), an Engineering and Physical Sciences Research Council (EPSRC) Studentship (to P.B.-J.), a Company of Biologists Development Travelling Fellowship (DEVTF-151210 to P.B.-J.), a Newnham College Constance Work Junior Research Fellowship (to N.M.), the École Polytechnique Fédérale de Lausanne (D.D. and M.P.L.), the University of Geneva (D.D.), the Swiss National Research Fund (No. 310030B_138662 to D.D.) and the European Research Council grants ERC MOFDH (No. 250316 to A.M.A.), *RegulHox* (No 588029 to D.D.) and STEMCHIP (No 311422 to M.P.L.).

Materials and Methods

Culture of gastruloids

E14Tg2a (ref.²⁶), (E14), *Bra*^{GFP} (ref.²⁷), *Gata6*^{H2B-Venus} (ref.²⁸), *Nodal*^{YFP} (ref.²⁹) and *Sox1*^{eGFP};*Bra*^{mCherry} double reporter (SBR³⁰) mouse embryonic stem (ES) cells were cultured on gelatinized tissue-culture flasks in a humidified incubator (5% CO₂, 37 °C) as previously described^{3, 6, 31}. The E14Tg2A ESC line was obtained from the group of A. Smith. The *Bra*^{GFP} ESC line was obtained from the Keller laboratory. The *Gata6*^{H2B-Venus} ESC line was generated by the laboratories of A. Martinez Arias and C. Schröter. The *Nodal*^{YFP} cell line was obtained from the Collignon laboratory. The SBR ESC line was obtained through mutual transfer agreement from the laboratory of D. Suter.

The different cell lines used in this study were validated as follows: for the *Bra*^{GFP} ESC line, stimulation with Activin/Chi resulted in an increase of the GFP reporter which overlapped with the signal of the anti-BRA antibody; for the *Nodal*^{YFP} ESC line, we tested whether expression of the reporter was upregulated after Activin stimulation, while its expression was blocked by Nodal inhibitor SB43; the *Gata6*^{H2B-Venus} and SBR ESC lines were validated by genotyping and via co-staining with GATA6 and BRA antibodies, respectively. All cell lines were routinely tested and confirmed to be free of mycoplasma via the MYCOPLASMACHECK service of GATC Biotech.

The E14, *Bra*^{GFP}, *Gata6*^{H2B-Venus} and *Nodal*^{YFP} mouse ESC lines were cultured in GMEM supplemented with 10% fetal bovine serum (FBS), non-essential amino acids (NEAA), sodium pyruvate, GlutaMax, beta-mercaptoethanol (β -ME) and LIF (ESL). The SBR cell line was cultured in DMEM supplemented with 10% FBS, NEAA, sodium pyruvate, β -ME, 3 μ M Chi³², 2 μ M PD025901 (PD03) and LIF. If cells were not being passaged, half the medium was replaced with fresh medium. Gastruloids were generated as previously described^{3, 6, 33} with modifications (a detailed protocol describing gastruloid culture has been deposited in the Protocol Exchange repository³⁴). Mouse ES or iPSCs were collected from tissue-culture flasks, centrifuged and washed twice with warm PBS (containing Ca²⁺ and Mg²⁺). After the final wash, cells were resuspended in 3–4 ml fresh and warm N2B27 (NDiff) and the cell concentration was determined. For ESCs, the number of cells required to form gastruloids with a diameter of \sim 150 μ m at 48 h AA (\sim 300 cells) was determined and seeded in each well of a round-bottomed, low-adherence 96-well plate as 40 μ l droplets of N2B27. For iPSCs, we performed a titration of the initial number of cells required to form gastruloids capable of elongating until at least 144 h AA. Amongst the different conditions tested (200, 400, 600, 800 and 1,200 cells per well) the best results were obtained with a starting number of 800 cells per well. In all cases, a 24 h pulse of 150 μ l 3 μ M Chi was added at 48 h AA. Medium (150 μ l) was replaced with the same volume of fresh N2B27 daily. To extend the culture period, gastruloids were transferred onto low-attachment 24-well plates in 700 μ l fresh N2B27 at 120h and cultured in an incubator-compatible shaker for 48 h at 40 r.p.m. Four hundred microlitres medium was replenished at 144 h, and gastruloids fixed at 168 h. Gastruloids for the different time-points analysed in this study were allocated randomly. Only gastruloids showing clear signs of apoptosis were removed from the experimental group before processing/analysis of the samples. No statistical methods were used to predetermine sample size. Blinding was not relevant to the present study because any specific assumption or hypothesis was postulated a priori, nor was any specific comparison between different treatments or genotypes performed.

Animal experimentation

Mouse embryos for RNA-seq and whole-mount in situ hybridization (WISH) experiments were obtained from CD1 wild-type animals crossed in-house. Adult animals of 3 to 5 months old were used for the crosses. Embryos were collected at E6.5, E7.8, E8.5 and E9.5 dpc. All experiments were performed in agreement with the Swiss law on animal protection (LPA) under license number GE 81/14 (to D.D.) after approval by the Comité Consultatif pour l'Expérimentation Animale du Canton de Genève (the empowered authority).

RNA extraction and RNA-seq libraries preparation and sequencing

Pooled gastruloids derived from either ESCs or iPSCs were collected in 15-ml Falcon tubes and pelleted by centrifuging at 1,000 r.p.m. for 5 min. After washing with cold PBS, gastruloids were resuspended in 100 μ l of RNA later (Thermo Fisher) and stored at -80°C until RNA extraction. The number of ESC gastruloids collected for each RNA-seq replicate varied depending on their size: 295 at 24 h AA; 105 at 48 h AA; 37 at 72 h AA; 14 at 96 h AA and 5 at 120, 144 and 168 h AA. For quantitative PCR analysis, approximately 30 ESC/iPSC-derived gastruloids of 24–96 h, 15 of 120 h and 5 of 144 h AA were pooled for a single RNA extraction. The RNA was extracted using the RNeasy mini kit (Qiagen), following the manufacturer's instructions. Contaminant DNA was eliminated using on-column DNase digestion (Qiagen RNase free DNase set) and RNA was eluted in RNase-free water. RNA was quantified with the Qubit HS RNA quantification kit (Thermo Fisher) and the integrity was assessed with a Bio-analyser. For each replicate, RNA-seq libraries were prepared from 100 ng pure total RNA using the TruSeq Stranded mRNA protocol from Illumina with poly-A selection. Libraries were sequenced on a HiSeq 2500 machine as single-read, 100 bp reads. For RNA-seq of individual gastruloids, at least 10 from each stage (24 h, 72 h and 120 h AA) were collected individually and transferred to 1.5 ml Eppendorf tubes. After centrifugation, each gastruloid was washed once with cold PBS, resuspended in lysis buffer, and RNA was extracted immediately using the RNeasy micro kit (Qiagen) with on-column DNase digestion. RNA was quantified with the Qubit HS RNA quantification kit (Thermo fisher) and the integrity was assessed with the Bio-analyser. For each of the replicates of the 24 h AA gastruloids, a total of 0.65 ng RNA was used for the library preparation, whereas 8 ng total RNA was used for the RNA sequencing of the replicates of 72 h and 120 h AA. Libraries were prepared using the SMART-seq v4 Ultra Low Input RNA Kit for Sequencing (Clontech) and the Nextera XT library preparation kit (Illumina), following the manufacturer's instructions, and sequenced on an Illumina

NextSeq500 machine as single-read 75-bp reads.

qPCR analysis

Purified RNA from iPSC-derived gastruloids was reverse transcribed using the Promega GoScript Reverse Transcription Kit. Quantitative PCR analysis of mRNA levels for different *Hoxd* genes, *Bra* and the housekeeping gene *Hmbs* was performed using the SYBR Select Master Mix for CFX (Thermo Fisher) kit according to the manufacturer's instructions with specific primers^{6, 35}. The Biorad CFX96 thermocycler was used. At least two technical (PCR) replicates and two biological replicates were analysed per time point after aggregation.

RNA-seq data processing

No biological replicate was excluded from the RNA-seq analysis. Mitochondrial and non-autosomal genes were excluded as they were not relevant for the biological question addressed in this study. These exclusion criteria were established before the analysis of the data. RNA-seq reads were aligned on the mouse mm10 genome assembly (https://www.ncbi.nlm.nih.gov/assembly/GCF_000001635.20/) using TopHat 2.0.9³⁶, implemented in Galaxy³⁷. TopHat output files were processed with SAMTools³⁸ and BedTools³⁹. RNA-seq coverages were normalized to the millions of reads mapped for each sample. For the replicates of pooled gastruloids RNA-seq samples, average coverage files were calculated from the normalized coverages of each replicate. We used HTseq⁴⁰ implemented in the Galaxy server to count the number of uniquely mapped reads attributable to each gene (based on genomic annotations from Ensembl release 82⁴¹). We used DESeq2 to perform differential expression analyses. Specifically, we contrasted a generalized linear model that explains the variation in read counts for each gene, as a function of gastruloid stage, to a null model that assumes no effect of the treatment time. We ran the Wald test and the *P* values were corrected for multiple testing with the Benjamini–Hochberg approach. We computed reads per kilobase of exon per million mapped reads gene-expression levels using Cufflinks⁴². Fragments per kilobase of transcript per million mapped reads (FPKM) levels were log₂-transformed after adding an offset of 1 to each value. The log₂-transformed values were centred across samples before PCA; no variance scaling was performed. For single-gastruloid PCA, only the 1,000 most highly expressed genes were used. For this, an average FPKM expression level of all the replicates of the different time points was calculated and the genes were ordered accordingly.

For cluster analysis of the most variably expressed genes, the top 250 most variable genes were determined by row variance using the `genefilter::rowVars` function. All heat map clustering, as identified by accompanying dendrogram, was performed using Euclidean distances and complete hierarchical clustering. For each gene cluster, enrichment of gene ontology (GO) terms was performed using Gorilla⁴³, by comparing the unranked list of gene of each cluster versus the totality of GO-term-annotated genes and by using a P value threshold of $P < 10^{-4}$ and a false discovery rate (FDR) < 0.05 . When more than 10 GO-term categories satisfying these criteria were identified, we used the REVIGO tool⁴⁴ to summarize them, using an allowed similarity threshold of 0.7.

Probe cloning, in vitro transcription and in situ hybridization

Specific primers (Supplementary Information File 1) were used to amplify fragments of approximately 400–700 bp of the genes analysed using Taq DNA polymerase. The PCR fragments were gel-purified using the Qiagen Gel Extraction Kit and cloned in the pGEM-T Easy Vector System (Promega). Positive clones were verified by standard Sanger sequencing. For antisense RNA probe synthesis, the plasmids were digested with specific enzymes (Supplementary Information File 1) and purified with the Qiagen PCR purification kit. A total of 2 μ g of the digested plasmid was used for in vitro transcription using either T7, T3 or Sp6 polymerase (Promega) and the Sigma DIG labelling mix or fluorescein labelling mix. The probes were purified using Qiagen RNeasy mini kit.

Fluorescent and non-fluorescent whole mount in situ hybridization

Gastruloids at different stages AA and E8.5–E9.5 wild-type mouse embryos were collected in 5-ml tubes, fixed overnight at 4 °C in 4% paraformaldehyde (PFA) and stored in methanol at –20 °C. In situ hybridization on whole-mount gastruloids was performed as previously described⁴⁵, with some modifications. For non-fluorescent in situ hybridization, gastruloids or embryos were transferred into 12-well Costar Netwell permeable insets (ref. 3477) and rehydrated through a series of decreasing methanol concentrations. After washing in TBST (20mM Tris 137mM NaCl, 2.7mM KCl, 0.1% Tween, pH = 7.4), gastruloids were digested in proteinase K solution and post-fixed in 4% PFA. The duration and concentration of the proteinase K treatment depended on the developmental stage of the embryo or the gastruloid time point after aggregation. E8 and E9 mouse embryos were incubated for 5 and 7 min in a 5 μ g/ml proteinase K solution. Gastruloids at 72–120 h AA and 144–168 h AA were incubated for 1 or 2 min, respectively, in a 1.6 μ g/ml proteinase K solution. Proteinase K treatment was

stopped by rinsing embryos or gastruloids 3 times in a 2 mg/ml glycine-TBST solution. After post-fixation, gastruloids were prehybridized at 68 °C for 4 h to block non-specific RNA-probe interactions and incubated overnight at 68 °C with specific probes at approximately 200 ng/ml. The next day, probe washes were performed at 68 °C and the gastruloids were transferred to blocking solution at room temperature to impair nonspecific antibody recognition. Subsequently, digoxigenin (DIG)-labelled RNA probes were detected using anti-DIG antibody coupled to alkaline phosphatase (Sigma) at 1:3,000 dilution for 4 h at room temperature. Non-specific antibody background was removed by washing overnight in MABT (100 mM maleic acid, 150 mM NaCl, 0.1% Tween, pH 7.5). The next day, gastruloids were washed 3 times with TBST and 3 times in alkaline phosphatase buffer (0.1 M Tris pH 9.5, 100 mM NaCl, 0.1% Tween) and stained with BM purple solution (Sigma). For fluorescent in situ hybridization, gastruloids were processed as described above up to the antibody incubation step, but a higher probe concentration was used (500–700 ng/ml). In this protocol, fluoroscein-labelled and DIG-labelled probes targeting each of the two genes to be detected were incubated simultaneously. After probe washing (see above), gastruloids were incubated in blocking solution containing anti-fluorescein antibody coupled to horseradish peroxidase (HRP) 1:100 (Perkin Elmer) for 3–4 h at room temperature. Gastruloids were subsequently washed several times in MABT overnight. The next day, gastruloids were washed 3 times for 5 min in TBST and 3 times in TNT solution (0.1 M Tris pH 7.5, 150 mM NaCl, 0.05 Tween). The fluoroscein-labelled probe was then developed using the TSA PLUS Fluorescein system (Perkin Elmer) for 10–12 min, following the manufacturer's instructions. To stop the first developing reaction, the anti-fluorescein-coupled HRP was inactivated by washing the gastruloid 2 times (5 min each) in PBS-Triton 0.3% followed by one hour incubation with PBS-Triton 0.3% + 1% H₂O₂, and post-fixing the gastruloid for 35 min in 4% PFA solution. After 3 washes in TBST and 2 washes in MABT (5 min each), gastruloids were again incubated in blocking solution with anti-DIG antibody coupled to HRP (1:200; Perkin Elmer) for 4 h at room temperature. Subsequently, gastruloids were washed overnight in MABT. The next day, gastruloids were washed 3 times for 5 min in TBST and 3 times in TNT solution. The DIG-labelled probe was then developed using the TSA PLUS Cyanine 3.5 system (Perkin Elmer) for 10 min, following the manufacturer's instructions. The developing reaction was stopped as described above.

Histology

Histology was performed on the EPFL platform (Lausanne). For cryostat sectioning after WISH, gastruloids were placed in Histogel (Thermo Fisher) and oriented under a binocular microscope. Solidified gels were placed in a plastic mould filled with Cryomatrix (Thermo Fisher) and frozen with isopentane. Sections with a thickness of 8 μm were obtained with a Leica CM3050S cryostat. For paraffin section and haematoxylin staining, 5- μm -thick sagittal or coronal sections were used following standard procedures.

Immunostaining and confocal microscopy

Gastruloids were fixed and either Hoechst 33342 or DAPI was used to mark the nuclei. The primary and secondary antibodies used are listed in Supplementary Information File 1. Confocal images of gastruloids were generated using an LSM700 (Zeiss) on a Zeiss Axiovert 200M primarily using a 40 \times EC Plan-NeoFluar 1.3 NA DIC oil-immersion objective. For some samples, either an EC Plan-NeoFluar 10 \times /0.3 or a Plan-Apochromat 20 \times /0.8 was used. Hoechst 33342, Alexa Fluor 488, Alexa Fluor 568 and Alexa Fluor 633 were sequentially excited with 405, 488, 555 and 639-nm lasers, respectively, as previously described⁶. Data capture was carried out using Zen2010 v6 (Carl Zeiss Microscopy) and z stacks were acquired with a z interval of 0.5 μm . Images were analysed using the ImageJ image processing package FIJI⁴⁶. For FISH samples, FITC and Cy3.5 were excited with 488 and 555 nm lasers, respectively.

Left-right asymmetry quantification methods

Gastruloids formed from *Nodal*^{YFP} ESCs were fixed at 120 h AA, stained for YFP (indicating nodal expression), *Bra* and *Sox2*, and z stacks were acquired from two opposite directions, 0° and 180°. The stacks from both sides of the gastruloid were then aligned and registered in FIJI⁴⁶. Gastruloids were scored as having a node-like structure if a region of nodal expression was found on the ventral surface directly opposite the dorsal expression of *Sox2*, and near the posterior *Bra*-expressing region. The ‘left’ or ‘right’ sides of the gastruloid were then inferred from the expression of *Sox2* (dorsal-ventral axis) and *Bra* (antero-posterior axis), and the frequency of those displaying asymmetric *Nodal*^{YFP} expression on the bilateral axis was quantified. To test the significance of this asymmetry, the occurrence of asymmetry in a control gene, *Meox1* (probed by WISH), which is usually expressed on both sides, was quantified and a binomial test of expected versus observed was performed. The fraction of gastruloids displaying symmetric or asymmetric *Nodal* and *Cer1* expression after WISH detection was visually inferred under a stereoscope (Leica MZ205). In these cases, as for *Meox1*, no reference

gene was used to determine the left and right side of the gastruloid. In all cases, the frequency of gastruloids displaying symmetric versus asymmetric gene expression was contrasted with the expected frequency based on the expression of these genes in wild-type embryos (*Meox1*: 100% symmetric; *Nodal* and *cerberus*: 100% asymmetric). The observed proportions of *Nodal* and *Cer1* expression pattern in gastruloids were then compared to those of *Meox1*, using the latter as expected frequency for laterally symmetric expression. The Wilson/Brown hybrid test was used to determine the confidence interval.

References

1. Rossant, J. & Joyner, A. L. Towards a molecular-genetic analysis of mammalian development. *Trends Genet.* **5**, 277–283 (1989). ^[1]_[SEP]
2. Simunovic, M. & Brivanlou, A. H. Embryoids, organoids and gastruloids: new approaches to understanding embryogenesis. *Development* **144**, 976–985 (2017). ^[1]_[SEP]
3. van den Brink, S. C. et al. Symmetry breaking, germ layer specification and axial organisation in aggregates of mouse embryonic stem cells. *Development* **141**, 4231–4242 (2014). ^[1]_[SEP]
4. Sasai, Y., Eiraku, M. & Suga, H. In vitro organogenesis in three dimensions: self-organising stem cells. *Development* **139**, 4111–4121 (2012). ^[1]_[SEP]
5. Turner, D. A., Baillie-Johnson, P. & Martinez Arias, A. Organoids and the genetically encoded self-assembly of embryonic stem cells. *BioEssays* **38**, 181–191 (2016). ^[1]_[SEP]
6. Turner, D. A. et al. Anteroposterior polarity and elongation in the absence of extraembryonic tissues and spatially localised signaling in gastruloids, mammalian embryonic organoids. *Development* **144**, 3894–3906 (2017). ^[1]_[SEP]
7. Zhao, R. et al. Loss of both GATA4 and GATA6 blocks cardiac myocyte differentiation and results in acardia in mice. *Dev. Biol.* **317**, 614–619 (2008). ^[1]_[SEP]
8. Carninci, P. et al. The transcriptional landscape of the mammalian genome. *Science* **309**, 1559–1563 (2005). ^[1]_[SEP]
9. Chal, J. et al. Recapitulating early development of mouse musculoskeletal precursors of the paraxial mesoderm in vitro. *Development* **345**, dev157339 (2018). ^[1]_[SEP]
10. Olivera-Martinez, I. et al. Major transcriptome re-organisation and abrupt changes in signaling, cell cycle and chromatin regulation at neural differentiation *in vivo*. *Development* **141**, 3266–3276 (2014). ^[1]_[SEP]
11. Dessaud, E., McMahon, A. P. & Briscoe, J. Pattern formation in the vertebrate neural tube: a sonic hedgehog morphogen-regulated transcriptional network. *Development* **135**, 2489–2503 (2008). ^[1]_[SEP]
12. Wang, P. et al. A molecular signature for purified definitive endoderm guides differentiation and isolation of endoderm from mouse and human embryonic stem cells. *Stem Cells Dev.* **21**, 2273–2287 (2012). ^[1]_[SEP]
13. Beck, F., Erler, T., Russell, A. & James, R. Expression of Cdx-2 in the mouse embryo and placenta: possible role in patterning of the extra-embryonic membranes. *Dev. Dyn.* **204**, 219–227 (1995). ^[1]_[SEP]

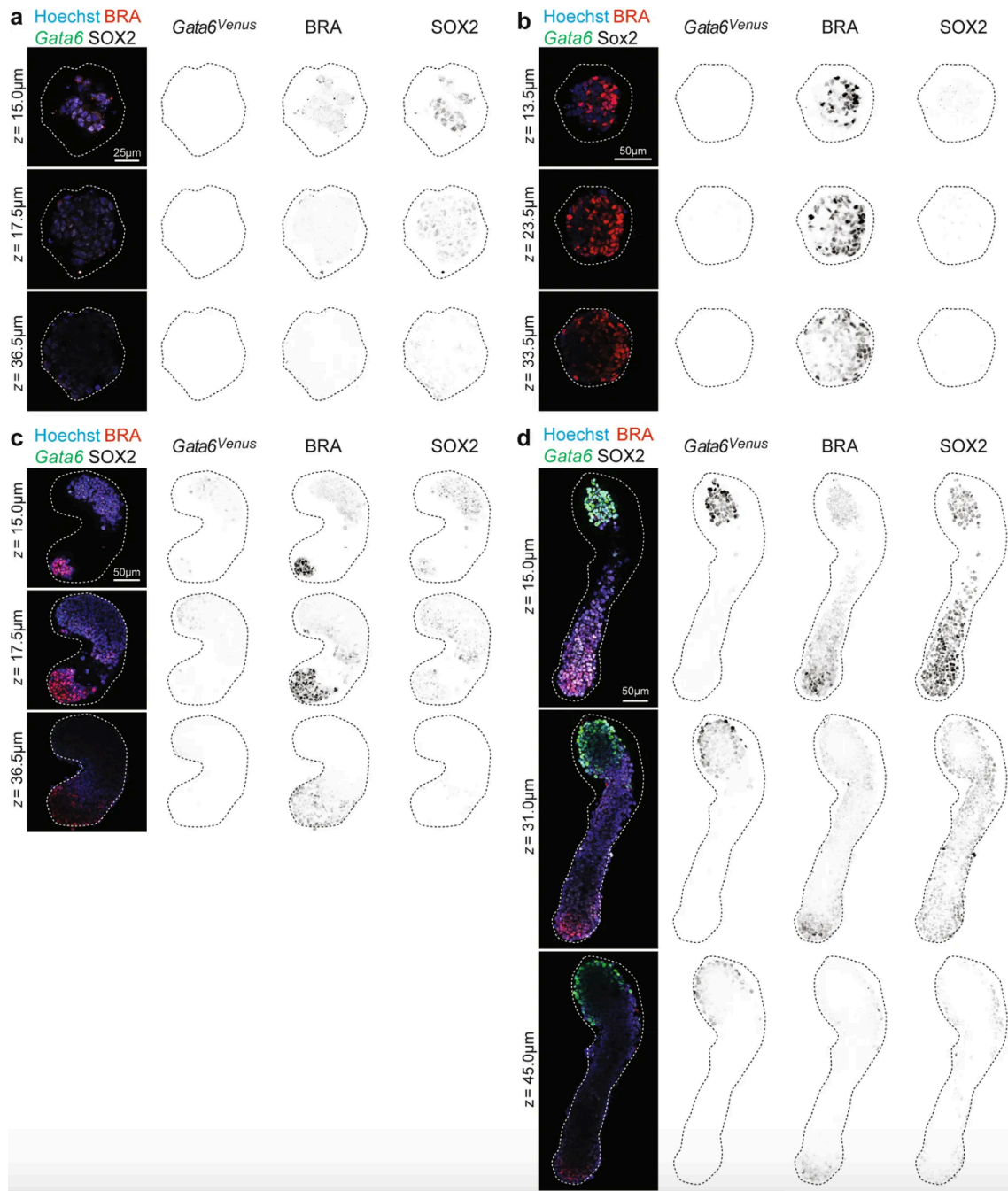
14. Blum, M. et al. Gastrulation in the mouse: the role of the homeobox gene goosecoid. *Cell* **69**, 1097–1106 (1992). ^[1]_{SEP}
15. Lee, J. D. & Anderson, K. V. Morphogenesis of the node and notochord: The cellular basis for the establishment and maintenance of left–right asymmetry in the mouse. *Dev. Dyn.* **237**, 3464–3476 (2008). ^[1]_{SEP}
16. Deschamps, J. & van Nes, J. Developmental regulation of the Hox genes during axial morphogenesis in the mouse. *Development* **132**, 2931–2942 (2005). ^[1]_{SEP}
17. Deschamps, J. & Duboule, D. Embryonic timing, axial stem cells, chromatin dynamics, and the Hox clock. *Genes Dev.* **31**, 1406–1416 (2017). ^[1]_{SEP}
18. Scotti, M. & Kmita, M. Recruitment of 5' Hoxa genes in the allantois is essential for proper extra-embryonic function in placental mammals. *Development* **139**, 731–739 (2012). ^[1]_{SEP}
19. Harrison, S. E., Sozen, B., Christodoulou, N., Kyprianou, C. & Zernicka-Goetz, M. Assembly of embryonic and extra-embryonic stem cells to mimic embryogenesis in vitro. *Science* **356**, eaal1810 (2017).
20. Sato, T. et al. Single Lgr5 stem cells build crypt-villus structures *in vitro* without a mesenchymal niche. *Nature* **459**, 262–265 (2009).
21. Kadoshima, T. et al. Self-organization of axial polarity, inside-out layer pattern, and species-specific progenitor dynamics in human ES cell-derived neocortex. *Proc. Natl Acad. Sci. USA* **110**, 20284–20289 (2013).
22. Eiraku, M. et al. Self-organizing optic-cup morphogenesis in three-dimensional culture. *Nature* **472**, 51–56 (2011).
23. Lancaster, M.A. et al. Cerebral organoids model human brain development and microcephaly. *Nature* **501**, 373–379 (2013).
24. Rivron, N.C. et al. Blastocyst-like structures generated solely from stem cells. *Nature* **557**, 106–111 (2018).
25. Heisenberg, C.P. & Bellaiche, Y. Forces in tissue morphogenesis and patterning. *Cell* **153**, 948–962 (2013).
26. Hooper, M., Hardy, K., Handyside, A., Hunter, S. & Monk, M. HPRT-deficient (Lesch–Nyhan) mouse embryos derived from germline colonization by cultured cells. *Nature* **326**, 292–295 (1987).
27. Fehling, H. J. et al. Tracking mesoderm induction and its specification to the hemangioblast during embryonic stem cell differentiation. *Development* **130**, 4217–4227 (2003).

28. Freyer, L. et al. A loss-of-function and H2B-Venus transcriptional reporter allele for *Gata6* in mice. *BMC Dev. Biol.* **15**, 38 (2015).
29. Papanayotou, C. et al. A novel *Nodal* enhancer dependent on pluripotency factors and Smad2/3 signaling conditions a regulatory switch during epiblast maturation. *PLoS Biol.* **12**, e1001890 (2014).
30. Deluz, C. et al. A role for mitotic bookmarking of SOX2 in pluripotency and differentiation. *Genes Dev.* **30**, 2538–2550 (2016).
31. Turner, D. A. et al. Wnt/ β -catenin and FGF signaling direct the specification and maintenance of a neuromesodermal axial progenitor in ensembles of mouse embryonic stem cells. *Development* **141**, 4243–4253 (2014).
32. Ring, D. B. et al. Selective glycogen synthase kinase 3 inhibitors potentiate insulin activation of glucose transport and utilization in vitro and in vivo. *Diabetes* **52**, 588–595 (2003).
33. Baillie-Johnson, P., van den Brink, S.C., Balayo, T., Turner, D. A. & Martinez Arias, A. Generation of aggregates of mouse embryonic stem cells that show symmetry breaking, polarization and emergent collective behaviour *in vitro*. *J. Vis. Exp.* **105**, e53252 (2015).
34. Girgin, M. et al. Generating gastruloids from mouse embryonic stem cells. *Protoc. Exch.* <https://doi.org/10.1038/protex.2018.094> (2018).
35. Guerreiro, I. et al. Reorganisation of *Hoxd* regulatory landscapes during the evolution of a snake-like body plan. *eLife* **5**, e16087 (2016).
36. Kim, D. et al. TopHat2: accurate alignment of transcriptomes in the presence of insertions, deletions and gene fusions. *Genome Biol.* **14**, R36 (2013).
37. Blankenberg, D. et al. Galaxy: a web-based genome analysis tool for experimentalists. *Curr. Protoc. Mol. Biol.* **89**, 19.10.1–19.10.21 (2010).
38. Li, H. et al. The Sequence Alignment/Map format and SAM tools. *Bioinformatics* **25**, 2078– 2079 (2009).
39. Quinlan, A. R. BEDTools: The Swiss-army tool for genome feature analysis. *Curr. Protoc. Bioinformatics* **47**, 1–34 (2014).
40. Anders, S., Pyl, P.T. & Huber, W. HTSeq—a Python framework to work with high-throughput sequencing data. *Bioinformatics* **31**, 166–169 (2014).
41. Yates, A. et al. Ensembl 2016. *NucleicAcidsRes.* **44**, D710–D716(2016).
42. Roberts, A., Trapnell, C., Donaghey, J., Rinn, J. L. & Pachter, L. Improving RNA-seq expression estimates by correcting for fragment bias. *Genome Biol.* **12**, R22 (2011).^{[1][SEP]}

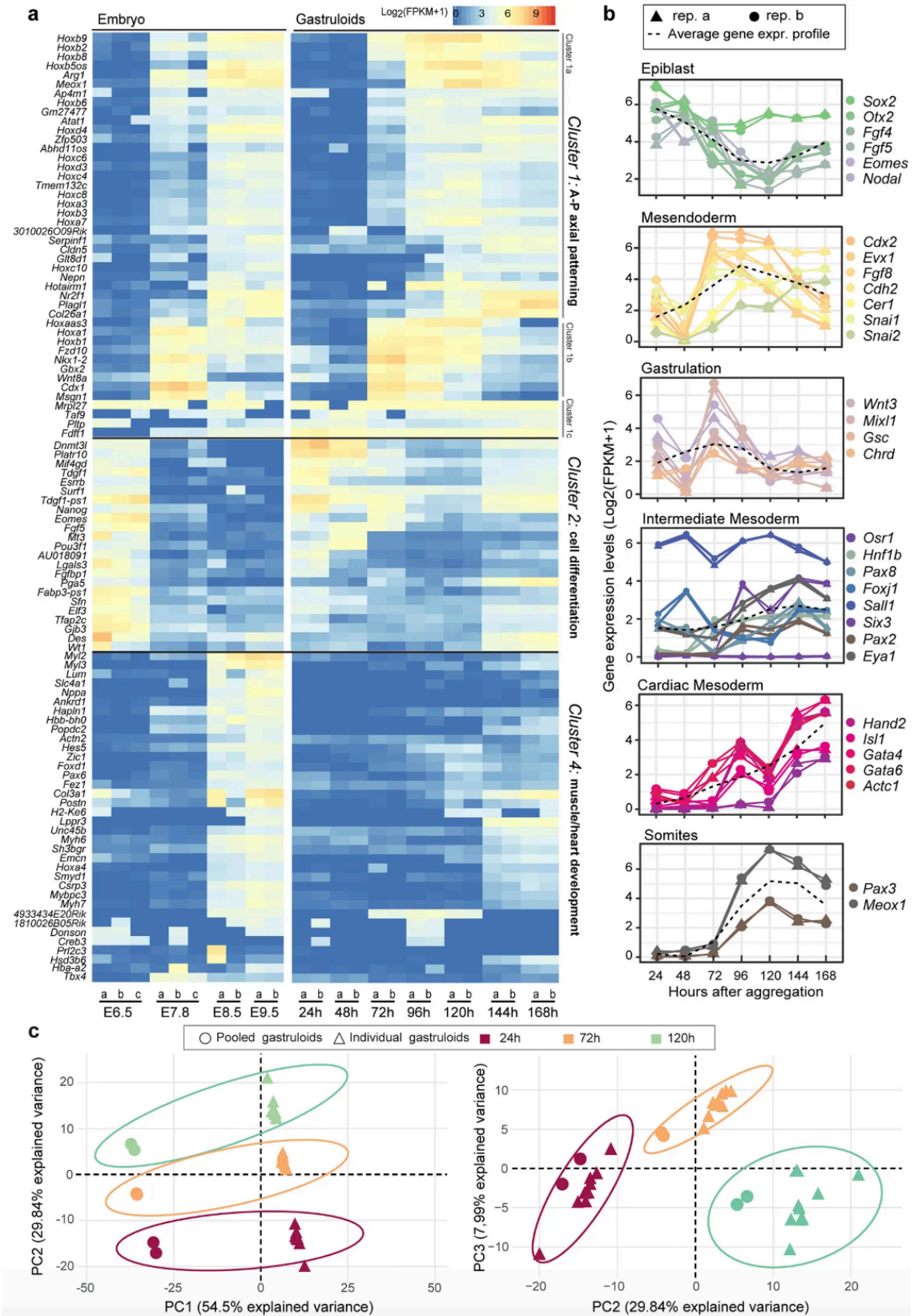
43. Eden, E., Navon, R., Steinfeld, I., Lipson, D. & Yakhini, Z. GOrilla: a tool for discovery and visualization of enriched GO terms in ranked gene lists. *BMC Bioinformatics* **10**, 48 (2009).^{[1][SEP]}
44. Supek, F., Bosnjak, M., Skunca, N. & Smuc, T. REVIGO summarizes and visualizes long lists of gene ontology terms. *PLoS ONE* **6**, e21800 (2011).
45. Woltering, J. M., Noordermeer, D., Leleu, M. & Duboule, D. Conservation and divergence of regulatory strategies at *Hox* loci and the origin of tetrapod digits. *PLoS Biol.* **12**, e1001773 (2014).^{[1][SEP]}
46. Schindelin, J. et al. Fiji: an open-source platform for biological-image analysis. *Nat. Methods* **9**, 676–682 (2012).^{[1][SEP]}
47. Shawlot, W., Deng, J. M. & Behringer, R. R. Expression of the mouse *cerberus*-related gene, *Cerr1*, suggests a role in anterior neural induction and somitogenesis. *Proc. Natl Acad. Sci. USA* **95**, 6198–6203 (1998).

SUPPORTING INFORMATION FOR CHAPTER II:

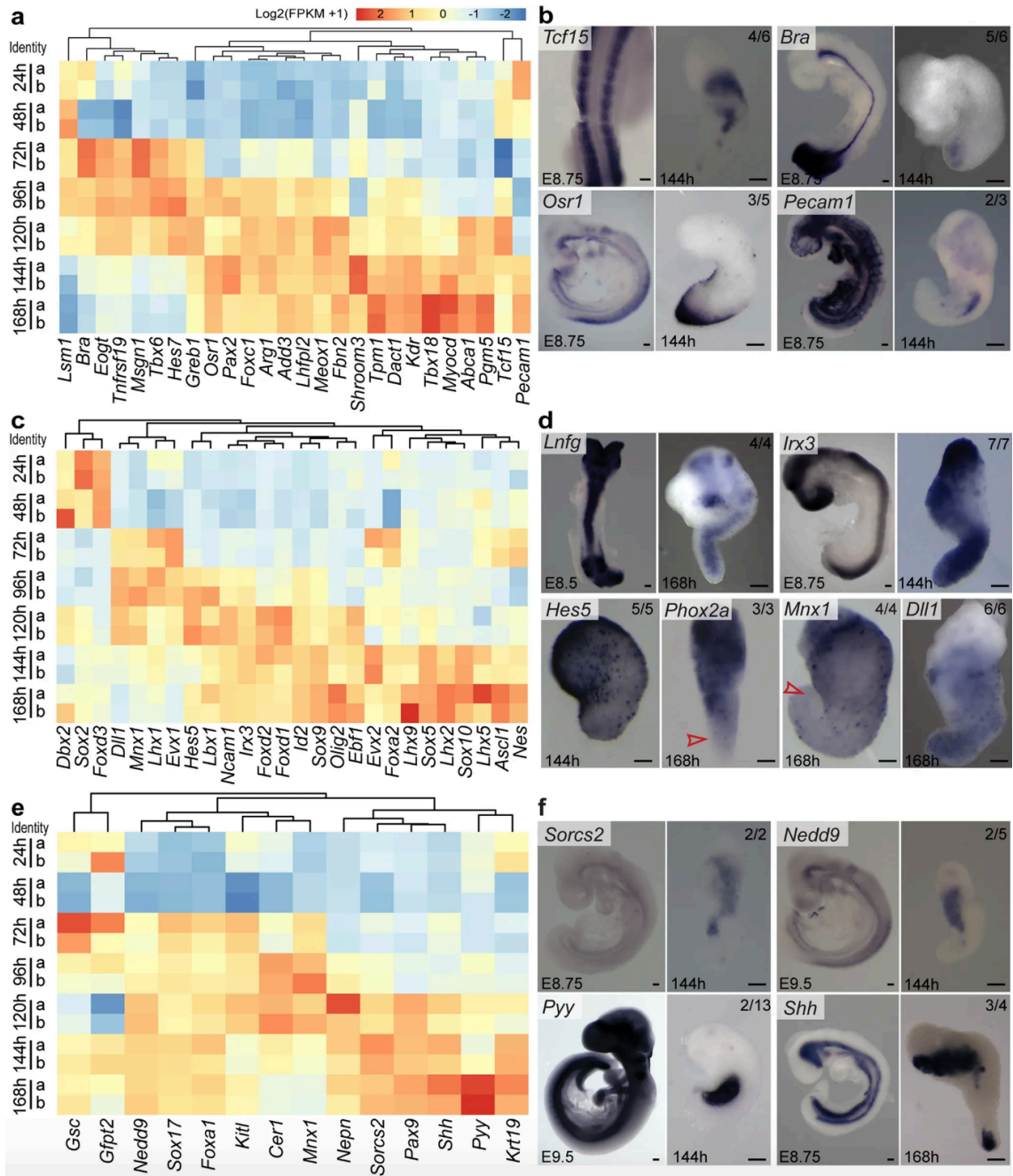
MULTI-AXIAL SELF-ORGANISATION PROPERTIES
OF MOUSE EMBRYONIC STEM CELLS INTO GASTRULIDS



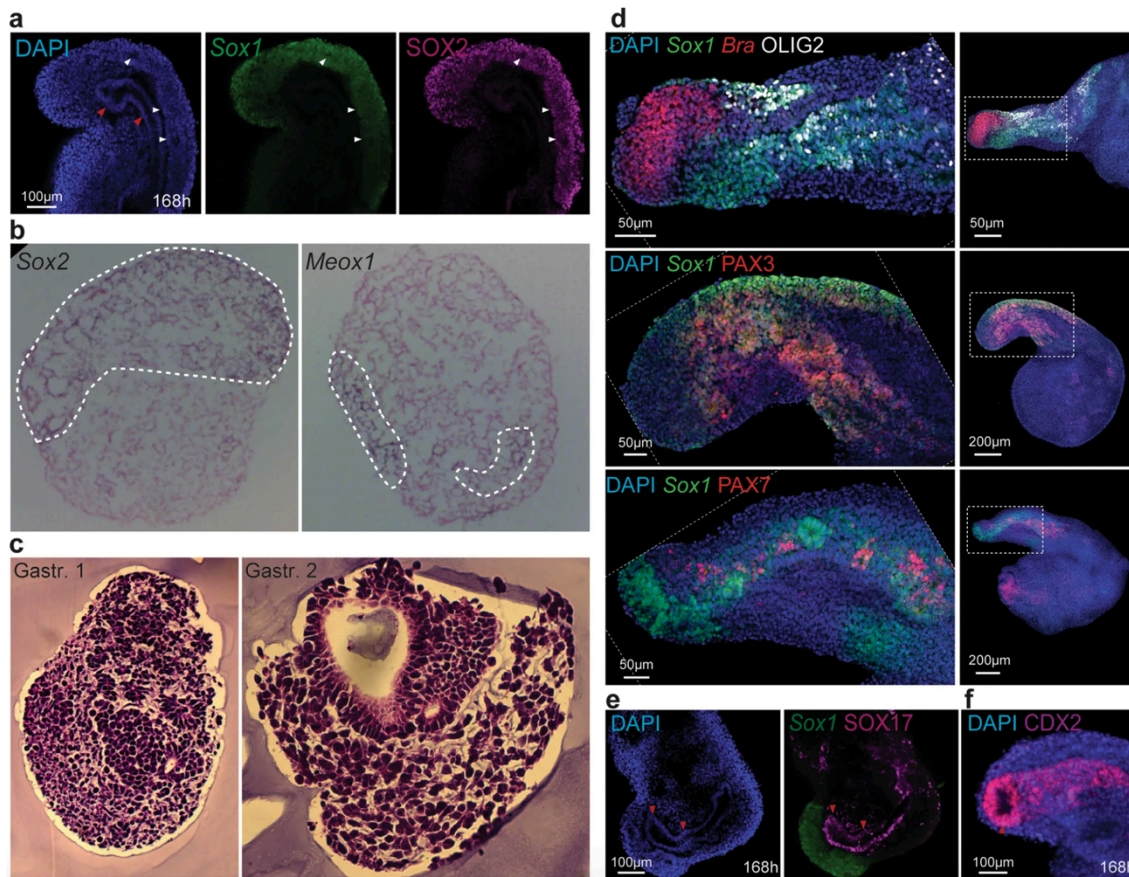
Extended Data Fig. 1: z stacks used for 3D rendering of gastruloids. a–d), Gastruloids produced using Gata6H2B-Venus ESCs treated with a pulse of the GSK3 inhibitor Chi between 48 h and 72 h AA and fixed at 48 h (a), 72 h (b), 96 h (c) or 120 h AA (d) and imaged by confocal microscopy. BRA and SOX2 proteins are stained in red and white, respectively. VENUS signal (green) reports Gata6 expression and Hoechst 33342 (blue) marks the nuclei. Gastruloids correspond to the 3D renderings shown in Fig. 1a. Each fluorescent channel is displayed to the right of the merged image. Gata6 (a) or Gata6 and SOX2 (b) signals were undetectable, and are therefore not shown. Three z sections are shown for each gastruloid. The bright-field outline of each gastruloid is indicated by the dashed lines. Each panel is representative of an experiment performed in parallel in seven independent biological replicates showing the same expression pattern. Scale bars are as indicated.



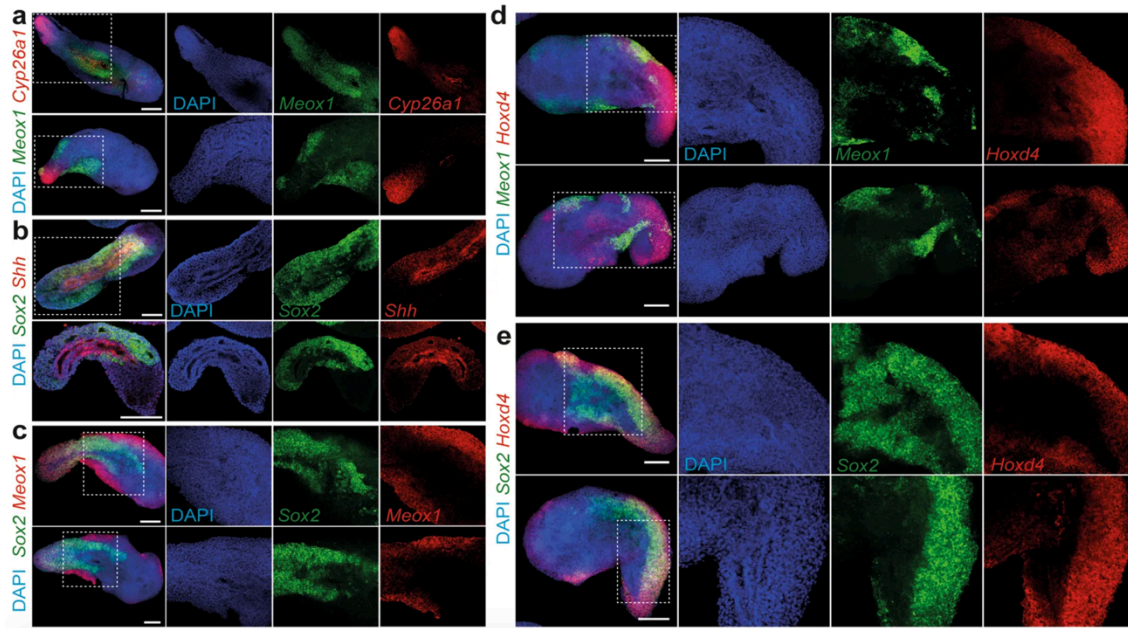
Extended Data Fig. 2: Transcriptional profiling of mouse embryos and *gastruloids*. **a)** Heat map showing the temporal evolution of 97 out of the 250 most variable genes throughout embryonic development from E6.5 to E9.5 (left) and their corresponding expression over the gastruloid time course, from 24 h to 168 h AA (right). Expression levels are indicated by colour scale from blue to red (bottom left). Genes were clustered according to their expression behaviour in the embryo. Enriched GO term categories were identified for each cluster using the Gorilla and REVIGO tools. Finally, a functional classification of each cluster was established based on the identified GO term categories and literature-based evidence. **b)** Expression of markers for different embryonic tissues through the gastruloid time course. The two replicates of each time point are represented by a triangle and a circle, respectively. The black dotted line in each plot represents the average behaviour of the genes displayed in the plot. For *gastruloids*, $n = 2$ independent biological replicates per time point; for E6.5 and E7.8 embryos, $n = 3$ independent biological replicates; for E8.5 and E9.5 embryos, $n = 2$ independent biological replicates. **c)** PCA analysis of RNA-seq datasets from either pooled or individual *gastruloids* using the top 1,000 most highly expressed genes. Despite different strategies used for RNA-seq of pooled versus individual *gastruloids* (accounting for the sample segregation across PC1), their clustering illustrates both the homogeneity of gastruloid cultures and the representativeness of pooled samples to single gastruloid samples. For individual gastruloid RNA-seq: $n = 10$ independent biological replicates per time point.



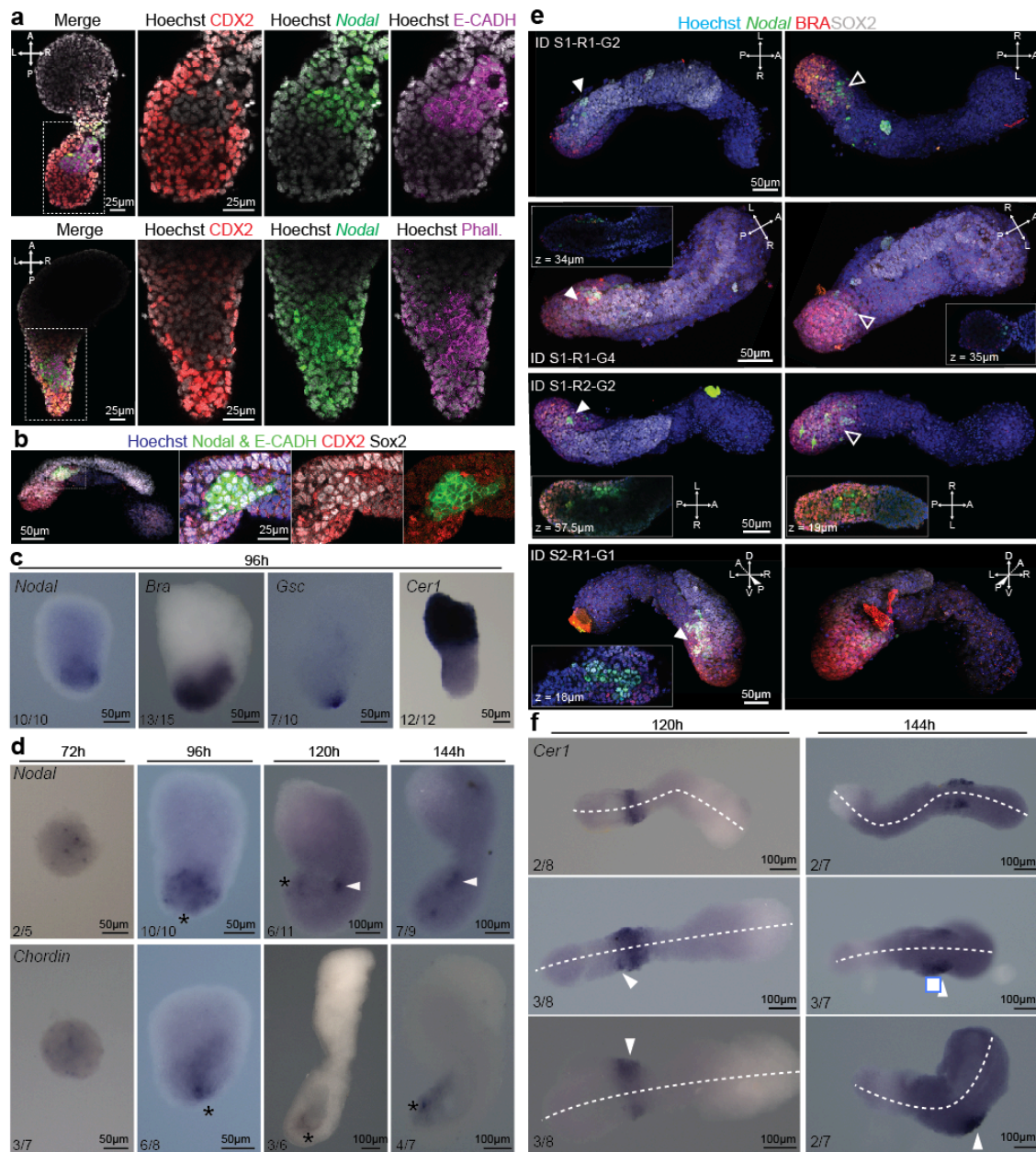
Extended Data Fig. 3: *Gastruloids* display spatio-temporal organization in the expression profiles of neural, mesodermal and endodermal marker genes. **a–f)** The expression profiles of several genes usually expressed in the embryonic neural, mesodermal and endodermal domains were analysed by plotting RNA-seq data from the pooled *gastruloids* in heat maps of scaled gene expression (2 independent biological replicates per time point) (**a, c, e**) and/or by WISH (**b, d, f**). **a,b)** Genes usually expressed in different types of mesoderm precursors in the embryo (for example, *Tcf15* in paraxial somatic mesoderm, *Osrl* in intermediate mesoderm, *Bra* in tail bud, notochord and presomitic mesoderm, and *Pecam1* in lateral plate mesoderm) were expressed in reproducible and spatially restricted domains within the *gastruloids*. **c,d)** Expression of different neural markers was detected in our RNA-seq (**c**). Transcripts of genes such as *Lfng* or *Irx3* formed continuous and homogenous domains located in the central and dorsal portion of the *gastruloids*, reminiscent of their expression domains in the embryo (**d**, top panels). Genes involved in Notch signaling in neural progenitors (*Hes5*, *Dll1*) and in the terminal differentiation of neural precursors (*Phox2a*, *Mnx1*) displayed a salt-and-pepper expression pattern, consistent with the lack of an organized neural-tube structure (see also Extended Data Figs. 4a, c, 5). However, the latter mRNAs also displayed a graded distribution along the anterior-to-posterior extension of the gastruloid axis and were absent from its posterior half (empty red arrowheads). **e,f)** Endoderm-specific genes were also expressed in *gastruloids*. In particular, genes expressed in the embryonic digestive tract were consistently found on the ventral side of *gastruloids*. For each gene, the proportion of *gastruloids* displaying the reported expression pattern is shown in the upper right corner of the image, expressed as a fraction of the total number. Scale bar, 100 μ m.



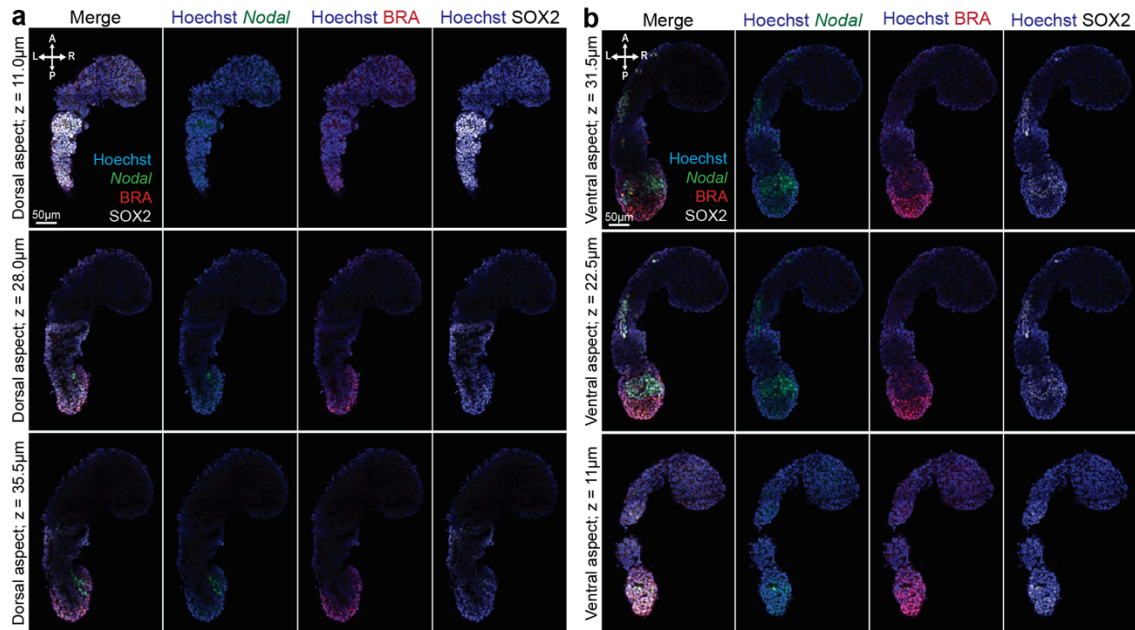
Extended Data Fig. 4: Tissue organization in gastruloids. **a)** *Gastruloids* formed from Sox1GFP;BramCherry (SBR) line and stained for Sox2 expression (Sox1GFP and SOX2 signals are displayed in green and magenta, respectively). White arrowheads indicate tubular SOX2/Sox1-positive neural structures. Red arrowheads point to the presumptive digestive tube. **b)** WISH on 8-μm transverse cryosections of *gastruloids* at 144 h AA using Sox2 and Meox1 antisense probes, counter-stained with Nuclear Fast Red. Sox2-positive cells localized predominantly in a compact dorsal domain, whereas Meox1 signals were found in two bilateral domains. The domain of expression of each gene is outlined with white dashed lines. **c)** Haematoxylin and eosin staining of transverse paraffin sections of different *gastruloids* at 120 h AA, showing the diversity of cell types and several levels of tissue organization. **d)** *Gastruloids* formed from Sox1GFP;BramCherry ESCs were fixed and stained at 168 h AA for OLIG2 (top, white), PAX3 (middle, red) and PAX7 (bottom, red). Scale bars as indicated. **c,d)** *Gastruloids* formed from Sox1GFP; BramCherry ESCs collected at 168 h AA and stained for SOX17 (magenta, **c**) or CDX2 (magenta, **d**). Scale bars as indicated. All immunostaining experiments were repeated twice, with three biological replicates per experiment, with similar results.



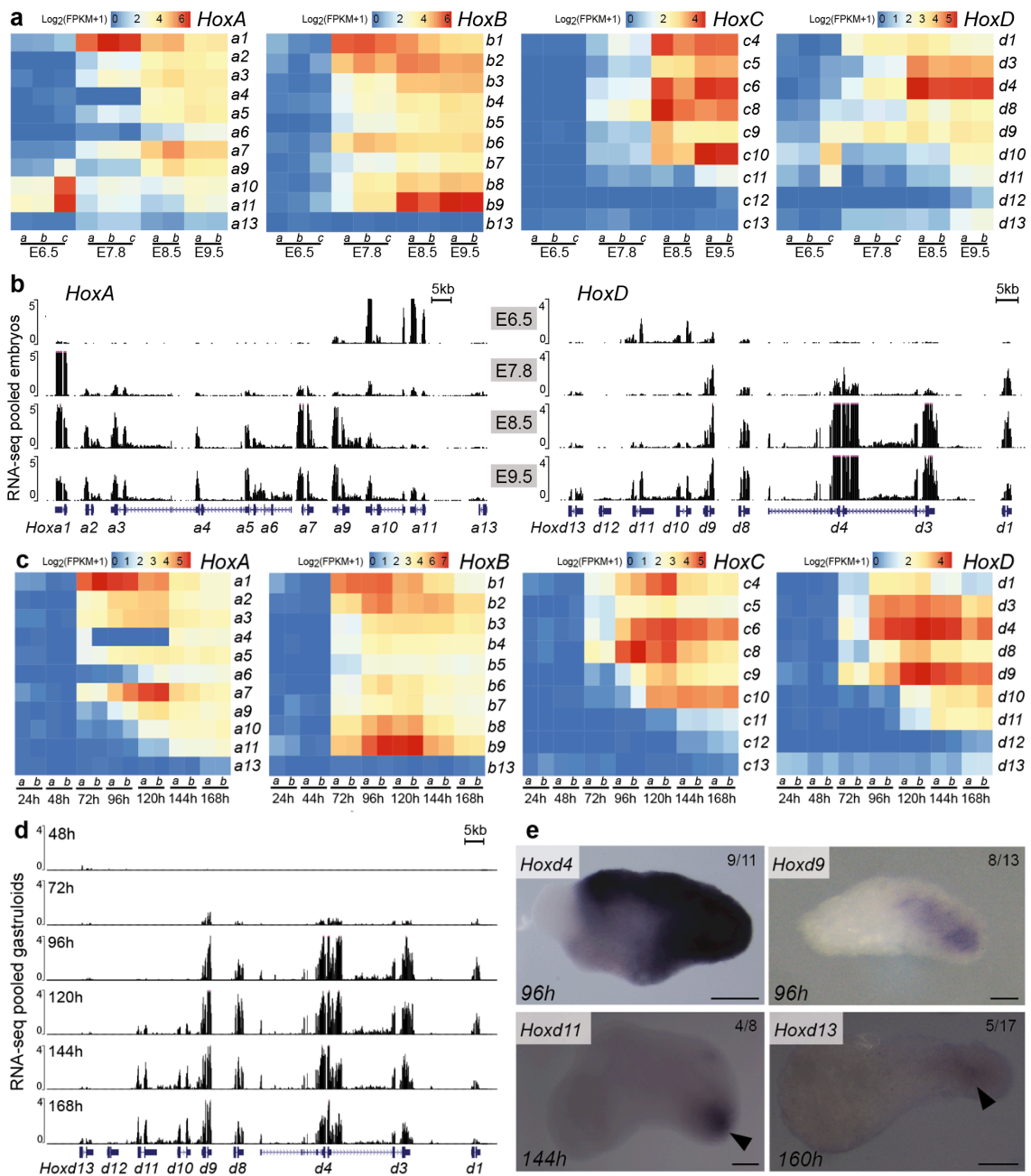
Extended Data Fig. 5: Double-FISH staining shows organized gene expression across the three main gastruloid axes. a–e Double-FISH staining of *gastruloids* at 144 h AA with Meox1 and Cyp26a1 (a), Sox2 and Shh (b), Sox2 and Meox1 (c), Meox1 and Hoxd4 (d) or Sox2 and Hoxd4 (e). **a–e** Experiments were repeated twice in three biological replicates with similar results. Scale bar, 200 μ m.



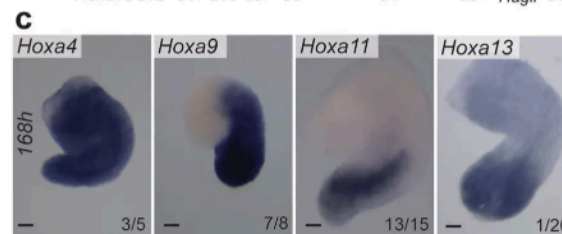
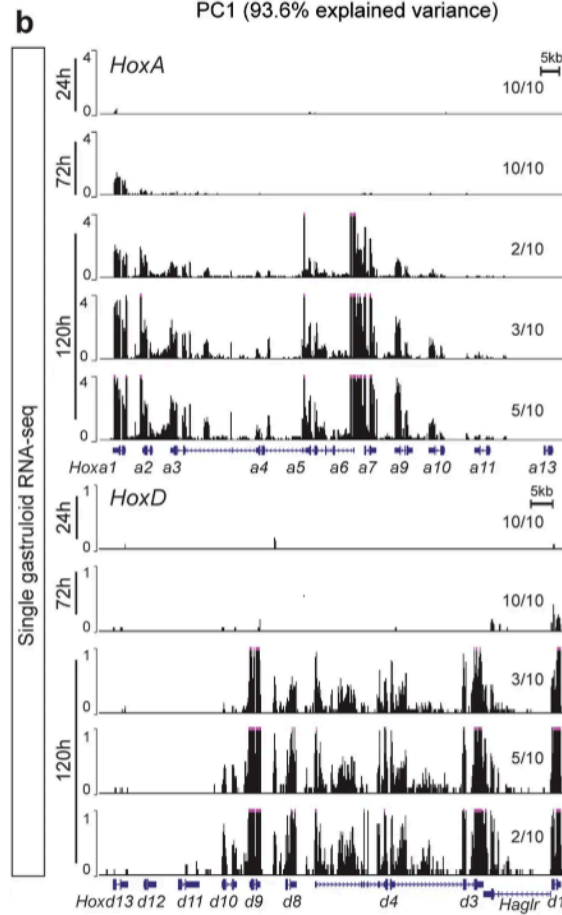
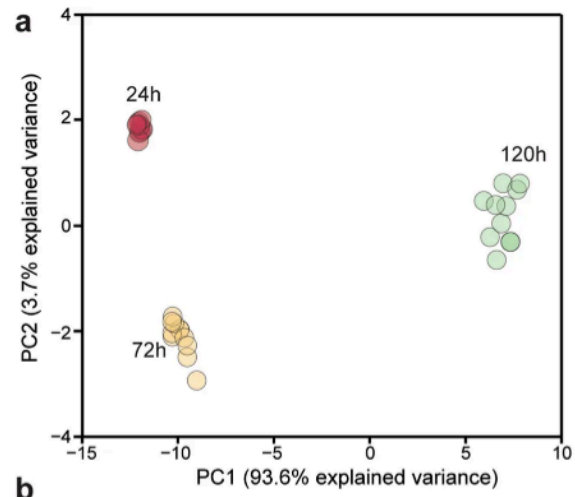
Extended Data Fig. 6: A node-like structure and left–right asymmetry in *gastruloids*. **a,b)** *Gastruloids* formed from NodalYFP ESCs were fixed at 120 h AA. They were stained for CDX2, YFP (NodalYFP) and E-cadherin (**a**, top panel), CDX2, YFP (NodalYFP, green) and phalloidin (**a**, bottom panel) or for CDX2, YFP and E-cadherin (both with an Alexa-488 secondary antibody), and SOX2 (**b**). Maximum intensity projection of a representative *gastruloid* in **b**, with the node-like structure highlighted. Hoechst 33342 labels the nuclei (greyscale in **a**, blue in **b**). Data are representative of one experiment performed in three independent biological replicates. **c,d)** In situ hybridization showing expression of the indicated genes in *gastruloids* at different time-points AA. *, presumptive node-like cells. White arrowheads point towards Nodal-expressing cells distributed asymmetrically, on the lateral side of the *gastruloid*. Whereas Nodal was expressed in the presumptive node region from 96 h AA, no clear asymmetry in transcript distribution was observed at that stage. **e)** Three-dimensional renderings of confocal stacks of 120 h *gastruloids* containing a NodalYFP reporter gene (green) and stained for SOX2 (white) and BRA (red) proteins. SOX2 signal identifies dorsal cells. Left and right panels show the same *gastruloid*, imaged from two different polar directions that is, top (dorsal) and bottom (ventral) or ‘left’ and ‘right’, depending on the orientation of the *gastruloid*. Insets in specific panels show a cross-section through the *gastruloid* at the indicated z plane. White arrowheads indicate the region of biased Nodal expression. Empty white arrowheads point to the node-like cells marked by the NodalYFP reporter gene (see also Fig. 4d). These results are consistent with the asymmetric distribution of Nodal transcripts at 120–144 h AA. **f)** In situ hybridization showing expression of *Cer1* in 120 h AA (left) and 144 h AA (right) *gastruloids*. The *gastruloid* midline is marked by a dashed white line. At this stage, *Cer1* is expressed in the presumptive embryonic somitic territory⁴⁷ and the pattern in *gastruloids* may reflect this specificity. In **c**, **d** and **f**, the proportion of *gastruloids* displaying the reported expression pattern is shown at the bottom left corner of each image, expressed as a fraction of the total number of specimens analysed.



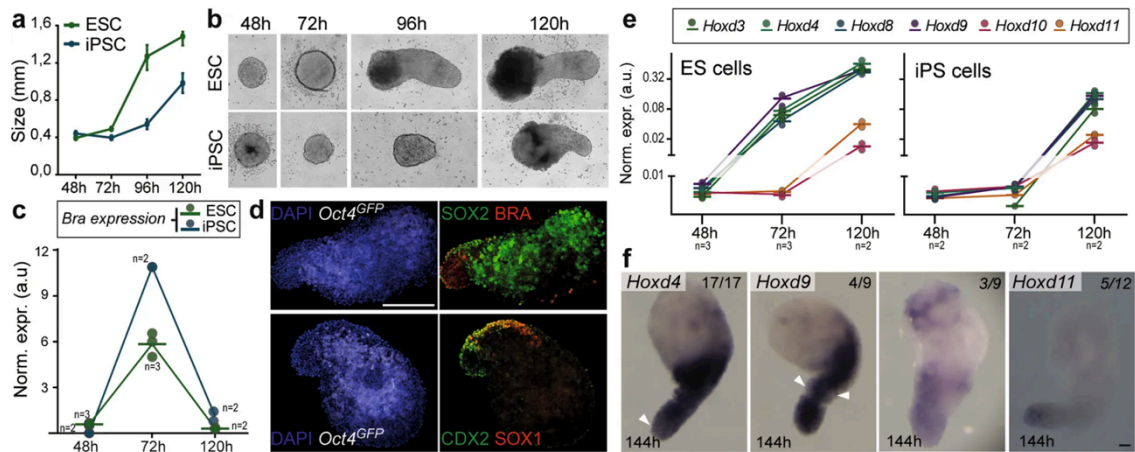
Extended Data Fig. 7: z stacks used for 3D rendering of *gastruloids*. **a,b)** Dorsal (**a**) and ventral (**b**) sections of the same representative *gastruloid* shown in the 3D renderings in Fig. 3d, fixed and stained at 120 h for NodalYFP (green), BRA (red) and SOX2 (white). Hoechst 33342 was used to label nuclei. Data are representative of two independent experiments with n = 13 biological replicates in total. Scale bar, 100 μm.



Extended Data Fig. 8: Hox expression profiles in mouse embryos and *gastruloids*. **a)** Heat map of unscaled gene expression in E6.5–E9.5 mouse embryos, showing levels of *Hox* gene transcripts over time. Between 2 and 3 independent biological replicates were used for each time point (indicated below each graph). **b)** RNA-seq mapping showing *Hoxa* and *Hoxd* gene expression in these embryos. After a first wave of transcription of 5' *Hoxa* and *Hoxd* genes, which is likely to reflect their activation in extra-embryonic tissues, the *HoxA* and *HoxD* clusters were progressively transcribed between E7.8 and E9.5, when expression of *Hox13* paralogues was detected. Each profile was averaged from independent biological replicates indicated in **a**. **c)** Heat map of unscaled gene expression in pooled *gastruloids*, showing *Hox* gene transcript levels over time. Two independent biological replicates were used per time point. **d)** RNA-seq mapping showing *Hoxd* gene expression in pooled *gastruloids* at different time points. Sub-groups of *Hoxd* genes are progressively activated between 72 h and 168 h AA, when expression of *Hoxd13* starts to be detected (**e**). This resembles the temporal activation described in vivo (**a**, **b**). Each profile represents the average of two independent biological replicates. **e)** WISH of *gastruloids* collected at different time points, showing the detectable initiation of expression of different *Hoxd* genes. Each panel shows the earliest stage at which the indicated gene was detected (black arrowhead). Expression of *Hoxd4* was already strong at 96 h AA, indicating that its transcripts are rapidly upregulated compared to *Hoxd9*, which is expressed at low levels at this stage. Scale bar, 100 μ m. The fraction of *gastruloids* displaying the reported expression pattern is indicated in the upper right corner of each image.



Extended Data Fig. 9: Homogeneity in Hox transcript profiles for individual *gastruloids*. **a)** PCA based on Hox-transcript datasets only, extracted from individually sequenced *gastruloids* across time points (10 individual *gastruloids* per time point, representing independent biological replicates). The analysis was carried out using the log2-transformed FPKM+1 value of all 39 Hox genes. Replicate batches of *gastruloids* primarily cluster according to their age at collection. The clustering revealed the low sample-to-sample variation. however, replicates were clearly separated by the temporal parameter, representing 93.6% of total sample variation. **b)** Comparison of Hoxa (top) and Hoxd (bottom) gene-expression profiles among individual *gastruloids* confirmed the low inter-sample variation among time points, illustrated with the 120 h AA condition. **c)** WISH of 168 h AA *gastruloids* showing the expression of different Hoxa paralogues. The proportion of *gastruloids* displaying the reported expression pattern is shown in the upper right corner of the image, expressed as a fraction of the total number. Scale bar, 100 μ m.



Extended Data Fig. 10: Axial extension and spatio-temporal Hox expression patterns in iPSC-derived *gastruloids*. **a)** Dot plot representing the progression in the measured longitudinal extension of *gastruloids* produced either from ESCs or from iPSCs. In each case, 10 different *gastruloids* were measured at the different time points indicated. The median (round points) and the interquartile range (vertical bars) are reported. **b)** Light microscopy images showing representative examples of *gastruloids* at the different time points analysed in **a**. Zoom: 10 \times . Note that iPSC-derived *gastruloids* exhibit delay in their longitudinal extension rate and at 120 h AA they are markedly smaller than their ESC-derived counterparts. For this analysis, *gastruloids* were produced starting from the same number of cells (800 cells per well). **c)** Dot plots representing the Bra mRNA levels, showing comparable dynamics of this gene in both types of *gastruloids*. Circles represent individual data points and the short horizontal line represents the mean. The number of biological independent replicates (n) per condition is indicated. **d)** Confocal images showing the expression of Oct4, SOX2 and BRA (top) or of Oct4, SOX1 and CDX2 (bottom) in 120 h AA *gastruloids* derived from the iPSC line Oct4::Gfp (IpSL40N). iPSC-derived *gastruloids* were fixed and stained for SOX2 and BRA (top) and CDX2 and SOX1 (bottom). Oct4::GFP signal is shown in grey. Scale bar, 200 μ m. In each case, data are representative of one experiment with three independent biological replicates. **e)** Dot plots representing the Hoxd mRNA levels in ESC- or iPSC-derived *gastruloids* collected at different time points AA. Each circle represents an independent biological replicate, the horizontal bars represent the mean value of the replicates. Both sets of *gastruloids* sequentially activated Hoxd gene expression. However, their temporal activation seemed to be delayed in iPSC *gastruloids* (especially that of the most 3' Hoxd paralogues). **f)** WISH of 144 h AA *gastruloids* showing the expression of different Hoxd paralogues. Even though iPSC-derived *gastruloids* reproduced the antero-posterior Hoxd collinear expression, the Hoxd9 expression domain often extended more anteriorly in comparison to that in ESC-derived *gastruloids* (see Fig. 4c), occupying roughly the same domain as Hoxd4. Patches of Hoxd-negative cells were often observed within the Hoxd4/Hoxd9 expression domain (white). The fraction of *gastruloids* displaying the reported expression pattern is indicated in the upper right corner of each image. Scale bar, 100 μ m.

Probe	Primer Forward	Primer Reverse
<i>Sox2</i>	CAGTAGACTGCACATGGCCCAG	GGCAGCCTGATTCCAATAACAGAG
<i>Krt18</i>	TCGCTCTCCTCTCCAGACAA	GAGCCCTCAGGTCTTCGATG
<i>Meox1</i>	AACAACCTCCGTGCCCCGATAG	CTGCCCCGGCTTCTGAGATAG
<i>Pax2</i>	CTGCCTATGACCGCCACTAG	AGCTCATCCACCTGAACTGC
<i>Lnfg</i>	CAGCTGGACCGGGAGCCTCG	CATCTCCTTGTGGCGCGAGATC
<i>Wnt3a</i>	TGGCAGAATGAGGCATGGAG	CTTGTGGCAGATGGGCTGTA
<i>Tcf15</i>	CTGCTGAGCGAGGACGAG	ACAGAAGGTGCAGATGGAGC
<i>Sorcs2</i>	TTCAGAATGCCCAGAGCTGG	CTGCTGTTTGGCACACTCAC
<i>Osr1</i>	GTGGGCAAAAAGAAGGGCT	TCTTCTTCCACACGCCAGAC
<i>Bra</i>	CCCAGGCTCCCAGACAGCTG	CGTCAACTGTTCTGCCCTTGGA
<i>Chrd</i>	TGTCTTCAGCAGCCTCTGAG	GAACCCCTGGTGCTGAGTGA
<i>Nedd9</i>	GTGGGCAAAAAGAAGGGCT	TCTTCTTCCACACGCCAGAC
<i>Irx3</i>	ATGTCAATCAGAGCCCGGAG	GTGCCCCGTACACTGATGAA
<i>Dll1</i>	GTGCCCCGTACACTGATGAA	ACCGGTCTAGAACACTCTGGGAG
<i>Hes5</i>	GAGGCGGTACAGTTCCTGAC	GGGCCCTGAAGAAAGTCCTC
<i>Pecam</i>	CGTCCATGTCCCGAGAAGAG	CCTGGGAAACAGCTCAGACC
<i>Mnx1</i>	CACTTCCCTGCGGACTACAG	AGCTGCTGCCGAATAACTGT
<i>Phox2a</i>	CAAGTTCCGCAAACAGGAGC	AGGGAGGGATAATGCCAGGT
<i>Pyy</i>	CCTCCTGCTCATCTTGCTTC	CACACAGCCCTCCAGTCTG

Primers used for the cloning of cDNA probes: Forward and reverse primers used to clone the probes for the different genes tested in this study.

Probe	Digest with:	Transcribe with:
<i>Hoxd4</i>	EcoRI	Sp6
<i>Hoxd9</i>	BamHI	T7
<i>Hoxd11</i>	EcoRI	T7
<i>Hoxd13</i>	PvuII	T7
<i>Hoxa4</i>	HindIII	T7
<i>Hoxa9</i>	SpeI	T7
<i>Hoxa11</i>	NcoI	Sp6
<i>Hoxa13</i>	NotI	T7
<i>Sox2</i>	NcoI	Sp6
<i>Lnfg</i>	SpeI	T7
<i>Krt18</i>	NcoI	Sp6
<i>Shh</i>	HindIII	T3
<i>Meox1</i>	SpeI	T7
<i>Pax2</i>	SpeI	T7
<i>Wnt3a</i>	SpeI	T7
<i>Raldh1a2</i>	EcoRI	T3
<i>Cyp26a1</i>	NcoI	Sp6
<i>Tcf15</i>	SpeI	Sp6
<i>Sorcs2</i>	NcoI	Sp6
<i>Osr1</i>	SpeI	T7
<i>Bra</i>	SpeI	T7
<i>Chrd</i>	NcoI	SP6
<i>Nedd9</i>	SpeI	T7
<i>Irx3</i>	Irx3	Sp6
<i>Dll1</i>	SpeI	T7
<i>Hes5</i>	SpeI	T7
<i>Pecam</i>	SpeI	T7
<i>Mnx1</i>	SpeI	T7
<i>Phox2a</i>	NcoI	Sp6
<i>Pyy</i>	ApaI	Sp6
<i>Cer1</i>	SalI	Sp6
<i>Gsc</i>	PstI	T3

In vitro probe synthesis: Enzymes used for plasmid digestion and in vitro transcription for probe synthesis.

	Target	Species	Dilution	Cat. No.	Supplier
Primary	anti-Brachyury	Goat	1:200	sc-17743	Santa Cruz Biotechnologies
	anti-CDX2	Rabbit	1:200	MA5-14494	ThermoFisher
	anti-E-Cadherin	Rat	1:100	M108	Takara
	anti-GFP	Chicken	1:2000	A11122	Molecular Probes
	anti-Olig2	Rabbit	1:500	AB9610	Merck Millipore
	anti-Pax3	Mouse	1:25	Pax3	DSHB
	anti-Pax7	Mouse	1:25	Pax7	DSHB
	anti-Sox17	Goat	1:500	AF1924	R&D Systems
	anti-Sox2	Rabbit	1:200	AB5603	Millipore
Secondary	anti-Chicken-A488	Goat		A11039	Molecular Probes
	anti-Goat-A568	Donkey	1:500	A11057	
	anti-Rabbit-A647	Donkey		A31573	
Dyes	Phalloidin-647	n/a	1:40	A22287	Invitrogen (ThermoFisher)
	DAPI	n/a	1:1000	D9542	Sigma-Aldrich
	Hoechst33342	n/a	1:1000	H3570	Invitrogen (ThermoFisher)

Antibodies and nuclear dyes used in immunostaining: this table summarizes the primary antibodies, secondary antibodies and nuclear dyes used in this study and their working dilutions.

CHAPTER III

ARTIFICIAL EPIBLASTS UNDERGO AXIAL MORPHOGENESIS AND FORM ANTERIOR NEURAL PROGENITORS INDEPENDENT OF EXOGENOUS WNT STIMULATION

ARTIFICIAL EPIBLASTS UNDERGO AXIAL MORPHOGENESIS AND FORM ANTERIOR NEURAL PROGENITORS INDEPENDENT OF EXOGENOUS WNT STIMULATION

Manuscript in preparation

Mehmet U. Girgin¹, Matthias P. Lutolf^{1,2*}

¹Institute of Bioengineering, Faculty of Life Sciences, Ecole Polytechnique Fédérale de
Lausanne (EPFL), Lausanne, Switzerland.

²Institute of Chemical Sciences and Engineering, School of Basic Sciences, Ecole
Polytechnique Fédérale de Lausanne (EPFL), Lausanne, Switzerland.

*Correspondence to: Matthias P. Lutolf (matthias.lutolf@epfl.ch)

Author contribution: M.U.G. and M.P.L. conceived the study, designed experiments, analyzed data and wrote the manuscript. M.U.G. performed the experiments.

Abstract

When stimulated with a pulse of an exogenous Wnt pathway activator, small aggregates of mouse embryonic stem cells (mESCs) can undergo embryo-like axial morphogenesis and patterning along the three major body axes. However, these structures, termed *gastruloids*, lack the most anterior embryonic regions such as those that belong to the brain. Here, we describe an approach to generate a new gastruloid version which displays a more complete antero-posterior development. We used bioengineered hydrogel microwell arrays to promote the robust derivation mESCs into post-implantation epiblast-like (EPI) aggregates in reproducible and scalable manner. We show that EPI aggregates break symmetry and undergo axial elongation with no external growth factor stimulation. Furthermore, inhibition of Wnt signaling at early stages resulted in formation of anterior neural progenitors that could not be generated previously in *gastruloids*. Interestingly, an epithelialization of EPI aggregates was found to substitute for Wnt inhibition, presenting an alternative approach to generate *gastruloids* with more elaborate neural development. We thus provide a new tool to study mouse post-implantation development *in vitro*, in particular, the emergence of anterior neural regions.

Introduction

Gastruloids have been useful to reveal the remarkable self-organization properties of mouse embryonic stem cells (ESCs), mimicking certain features of the developing early mouse embryo such as axial elongation and patterning¹⁻³. However, compared to the embryo, gastruloid development is restricted to the post-occipital region³. Most significantly, anterior neural regions corresponding to forebrain, midbrain and hindbrain are missing in *gastruloids*. Gastruloid derivation is based on the treatment of small mESC aggregates with the Wnt agonist CHIR99021 to induce axial elongation. This results in ubiquitous activation of Wnt signaling and expression of the primitive-streak marker *T/Bra* across the aggregate, inducing a uniform induction of mesodermal differentiation. This is in marked contrast to the mouse embryo, where Wnt signaling is activated first in a highly localized manner at the primitive streak on the posterior domain, and is tightly regulated across the epiblast by the secretion of Wnt antagonists from the anterior visceral endoderm⁴. The resulting signaling gradient thus protects the anterior epiblast from the “posteriorizing” signals and maintains it in an uncommitted (epiblast) state⁵. Indeed, mutant mouse embryos with increased Wnt activity upregulate posterior mesoderm genes at the anterior domain⁶, resulting in posterior axis duplication⁷ and failure to form forebrain⁸⁻¹⁰. Based on these results we hypothesized that the lack of anterior neural structures

in *gastruloids* might be due in part to the enhanced Wnt signaling during the initial stages of the culture.

Another major difference between *gastruloids* and the early embryo is the 3D architecture of the multicellular entity before the onset of ‘gastrulation’. *Gastruloids* are generated from dense and amorphous (*i.e.* non-polarized) spheroids aggregated from roughly 300 mESCs. The epiblast in the embryo is a columnar epithelium with a central lumen. During gastrulation, cells at the posterior domain of the epiblast undergo an epithelial-to-mesenchymal transition (EMT) and ingress through the primitive streak¹¹. The anterior epiblast is maintained as an epithelium throughout gastrulation and does not undergo EMT. The cells within this epithelial region were identified as the progenitors responsible for the subsequent brain formation^{12,13}. Indeed, previous studies have shown that aggregates of pluripotent stem cells could be successfully coaxed into brain-like¹⁴⁻¹⁶ and optic cup-like^{17,18} structures from an epithelialized stem cell aggregate (termed embryoid body). Based on these results we hypothesized that lack of anterior neural structures in *gastruloids* might be due in part to the lack of an epithelium during the initial stages of the culture.

Considering the above, here we sought to test whether *i)* lower levels of Wnt signaling or *ii)* the presence of a columnar epithelium could promote the formation of anterior neural structures in *gastruloids*. Specifically, we focused on modulating the initial aggregation stage, aiming at creating structures that transcriptionally and morphologically resemble the post-implantation epiblast. To this end, a new high-throughput cell aggregation and culture system was conceived that allowed for the formation of mESCs aggregates of defined size in high throughput.

Firstly, we specified a culture medium to induce epiblast identity by removing the Wnt agonist CHIR99021 and adding Fgf2 and Activin-A¹⁹. When cultured in serum- and growth factor-free medium, the resulting structures, termed EPI aggregates, initiated *T/Bra* expression, broke symmetry and underwent axial elongation similar to *gastruloids*, with *T/Bra*⁺ cells at the elongating (posterior) tip surrounded by *Sox1*⁺ *Sox2*⁺ neural tissue. Strikingly, when EPI aggregates were formed in the presence of a small molecule Wnt inhibitor (XAV939), *gastruloids* exhibited a surprising level of antero-posterior (A-P) development, with a population of *Sox1*⁺ and *Sox2*⁺ cells located anteriorly to the elongating *T/Bra*⁺ tip. In these culture conditions, elongation and patterning efficiencies were found to be strictly dependent on the initial aggregate size, with smaller aggregates failing to elongate and establish A-P patterning.

Secondly, to mimic the epithelial architecture of the post-implantation epiblast, we generated 3D EPI aggregates in medium supplemented with diluted (3%) laminin-111-rich Matrigel^{16,20-22}, resulting in EPI aggregates exhibiting a single layer epithelium with a central lumen. These epithelial EPI aggregates underwent axial elongation and established elaborate A-P patterning, demonstrating the role of an epithelium in anterior neural development. The initial size of epithelial EPI aggregates was again shown to be an important parameter controlling elongation and patterning, with larger aggregates failing to elongate and establish A-P patterning. Collectively, our data reveal the crucial role of the starting conditions, both with regards to the architecture and cell states of the initial mESC aggregate, in promoting morphogenesis and patterning along the A-P axis. Our new gastruloid culture approach provides a simple and versatile *in vitro* tool to study peri-gastrulation development and in particular the specification of anterior neural regions.

Results

Gastruloids exhibit posterior patterning

In conventional *gastruloid* culture^{1,2}, upon treatment with the Wnt agonist CHIR99021 between 48 h and 72 h of culture, *gastruloids* initiate *T/Bra* expression uniformly across the aggregate. By 96 h, *gastruloids* acquire an ovoid shape and exhibit polarized *T/Bra* expression that gets restricted to the tip as the elongation continues until 120h. Unlike in the previous reports^{3,23}, if the *gastruloids* are not transferred to shaking culture at this point, the elongation is not maintained and *gastruloids* acquire a rounded shape (**Fig. 1a**). In order to better understand the dynamics of the morphogenesis over time, we performed automated image analysis by fitting a spine of the *gastruloids* (white line) via connecting centers of inscribed circles (white circles) of various sizes. We calculated the elongation index by dividing the axial length (white line) to the diameter of the largest inscribed circle. The analysis revealed a peak of elongation index at 120 h that went down until 168 h as the elongated tip collapsed (**Fig. 1a,b**). However, *gastruloids* kept on increasing in length until 144h to reach over a millimeter, suggesting that loss of elongated morphology is not due to growth inhibition (**Fig. 1c**).

At 168 h, *gastruloids* showed expression of *Sox1* and *Pax6* at the elongated tip but not anteriorly beyond the “neck” (**Fig. 1d,e**, dashed lines), confirming formation of posterior neural tissue likely of a spinal cord identity. Moreover, we observed *Sox17*⁺, *Cdx2*⁺, *E-cadherin*⁺ epithelial tube-like structures below the *Sox1*⁺ neural tissue at the tail tip, resembling formation of hindgut (**Fig. 1f-h**)²⁴⁻²⁶. However, we did not detect any neural tissue on the anterior region,

which contained various cell types including *Gata4*⁺ cardiac progenitors²⁷ and *Six1*⁺ pre-placodal ectoderm-like cells²⁸ (**Fig1. i,j**), resembling the replacement of anterior neural tissue by posterior mesoderm tissue in Wnt mutant embryos⁶. Altogether these results and previous reports^{3,23} show that *gastruloids* could develop complex posterior patterning, however, do not contain any anterior neural tissues.

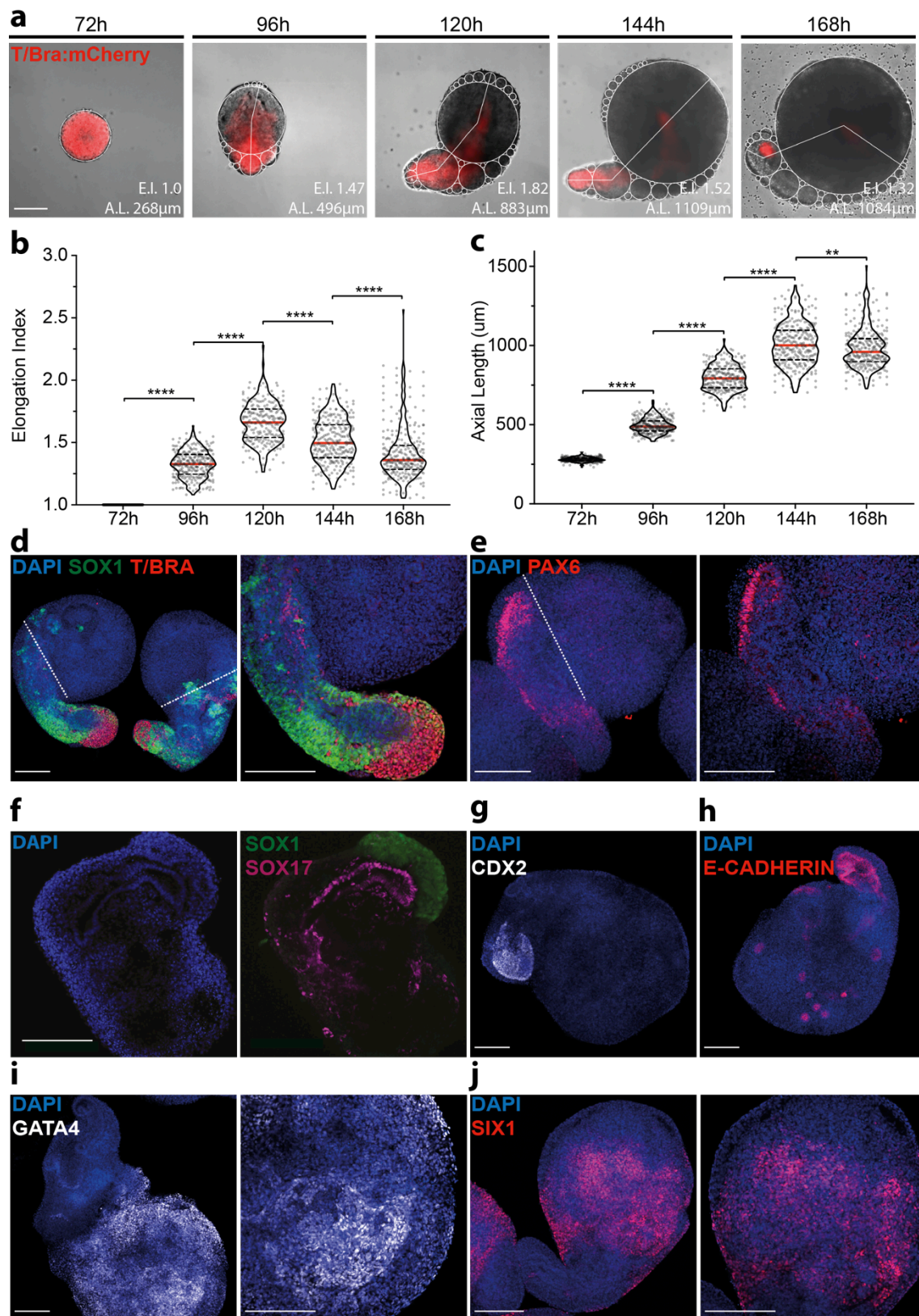


Figure 1: Dynamics of axial morphogenesis and patterning of gastruloids. **a)** Timepoint images showing *T/Bra* (red) expression dynamics and morphology analysis output (white lines and circles). **b,c)** Quantification of the elongation index (**b**) and axial length (**c**) of *gastruloids* at different timepoints. Data are shown as median. **d,e)** Confocal images showing *Sox1* (**d**) and *Pax6* (**e**) expression extending from the elongated tip until the neck (dashed lines). **f-h)** Confocal images showing *Sox17* (**f**), *Cdx2* (**g**) and *E-cadherin* (**h**) expression at the tail tip. **i,j)** Confocal images showing widespread expression of *Gata4* (**i**), and *Six1* (**j**) at the anterior domain. For all statistical analysis, one-way ANOVA followed by Bonferroni multiple comparison test was performed. Following P-value style was used: ns=not significant, P****<0.0001, P***<0.0002, P**<0.0021, P*<0.0332. Scale bars: 200µm.

High-throughput formation of EPI aggregates in hydrogel microwells

We reasoned that current gastruloid protocol is not conducive for the formation of anterior neural regions, as detailed above. Therefore, we modified the existing protocol to promote the formation of ‘artificial epiblasts’, aggregated mESCs that could mimic the post-implantation epiblast both transcriptionally and morphologically. To this end, we used poly(ethylene glycol) (PEG) microwells²⁹ to generate hundreds of aggregates of desired size (**Fig. 2a**). Moreover, to avoid excessive Wnt signaling, we formulated modified the gastruloid culture protocol and medium by removing CHIR99021 and adding Activin-A (20ng/ml), Fgf2 (12ng/ml) and Knockout Serum Replacement (1%), a medium composition that was previously shown to induce epiblast identity in differentiating mESCs¹⁹. To achieve a more homogenous epiblast identity^{30,31}, we further modified the medium by supplementing with XAV939, a small molecule inhibitor of Wnt pathway.

Starting from 25 or 100 cells/well, in both EPI and EPI+XAV medium, we successfully generated aggregates of different sizes in EPI medium (**Fig. 2b**). Aggregates formed from 100 cells/well in either media had similar average diameters by 72 h, whereas aggregates formed from 25 cells/well showed a reduced size when cultured in the presence of XAV939 (**Fig. 2c**).

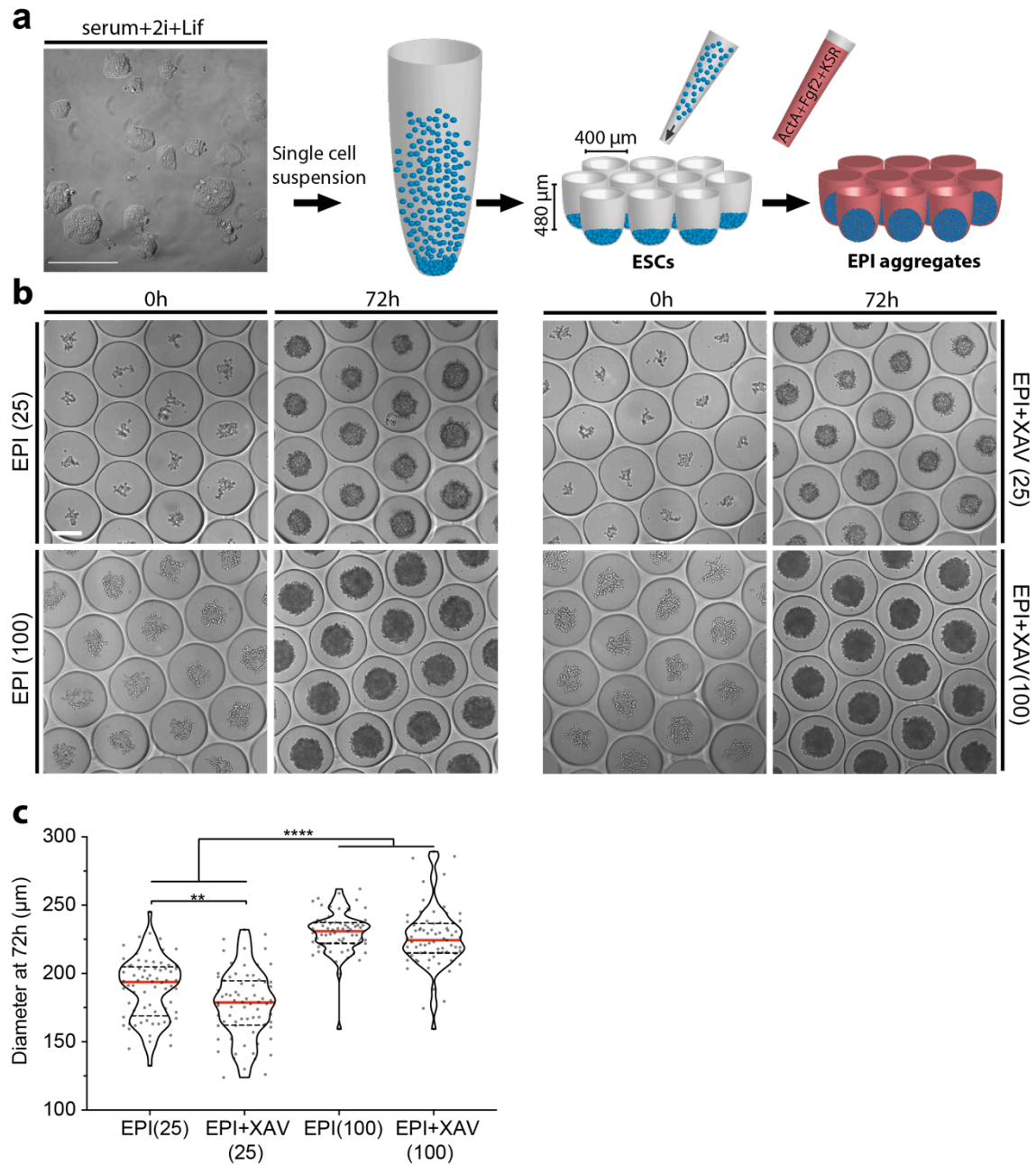


Figure 2: Formation of EPI aggregates on PEG microwells **a)** Schematic showing the experimental method to generate EPI aggregates on PEG microwells from mESCs maintained in serum+2i+lif medium. **b)** Timepoint images immediately after seeding 25 mESCs/well (top panel) and 100 mESCs/well (bottom panel) and at 72h when EPI aggregates are formed. **c)** Quantification of the diameter of EPI aggregates at 72h cultured in indicated conditions. Data are shown as median. For statistical analysis, one-way ANOVA followed by Bonferroni multiple comparison test was performed. Following P-value style was used: ns=not significant, P****<0.0001, P***<0.0002, P**<0.0021, P*<0.0332. Scale bars: 200 μ m.

To confirm that aggregates acquired the epiblast identity, we checked the expression levels of pluripotency markers in EPI aggregates by immunostaining. Aggregates formed in serum+2i+lif (s2iL) pluripotency maintenance condition demonstrated uniform expression of Oct4, Sox2 and Nanog, respectively (**Fig. 3a**, top panel). Aggregates formed in EPI medium also exhibited uniform expression of Oct4 but had lower levels of Sox2 and Nanog (**Fig. 3a**, middle panel). When XAV939 was added in the medium during aggregation, the aggregates exhibited uniform Oct4 expression and higher levels of Sox2 and Nanog, respectively, compared to EPI culture condition (**Fig. 3a**, bottom panel; **Fig. 3b,c**). qRT-PCR analysis revealed lower expression levels of pluripotency markers (Rex1, Klf4, Sox2 and Nanog) but similar Oct4 expression levels of EPI aggregates in comparison to mESCs cultured under maintenance conditions. Moreover, EPI aggregates greatly upregulated the expression of the epiblast-specific markers Fgf5 and Otx2 (**Fig. 3d**). Interestingly, aggregates formed in s2iL medium also showed considerable upregulation of the epiblast markers. We detected increased levels of *T/Bra* transcripts in EPI culture condition, which was lowered in the presence of XAV939, confirming the Wnt-dependent activation of *T/Bra* expression³². Altogether, these results demonstrate that mESC aggregates grown in EPI culture conditions acquire an epiblast identity which is further stabilized by the addition of the small molecule Wnt inhibitor XAV939, in line with previous reports³⁰.

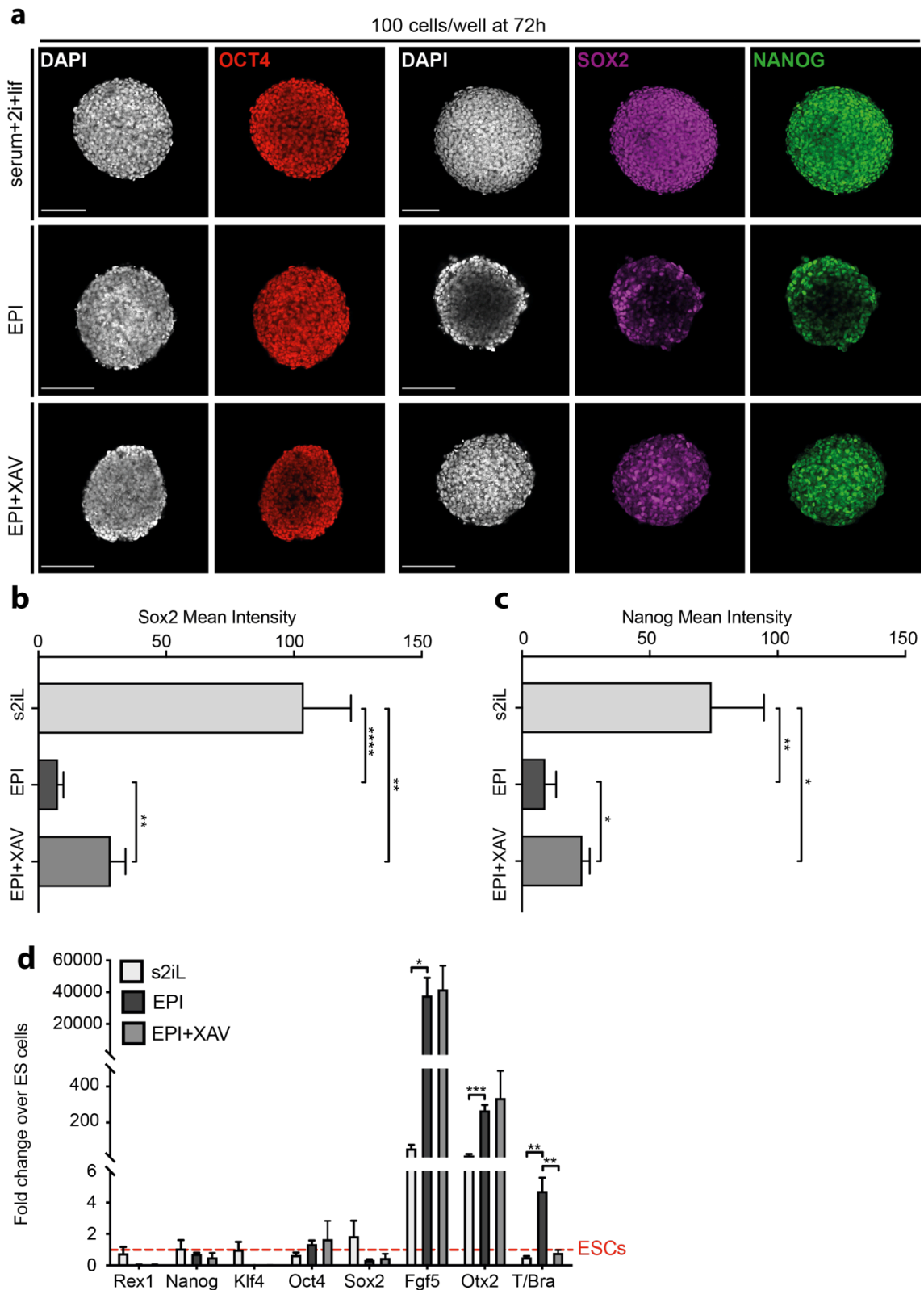


Figure 3: Characterization of the epiblast identity of EPI aggregates. **a)** Confocal images showing Oct4, Sox2 and Nanog expression in aggregates cultured under indicated conditions. **b,c)** Mean intensity value measurements of Sox2 (**b**) and Nanog (**c**) channels. **d)** qRT-PCR analysis of EPI aggregates at 72 h formed by 100 cells/well showing expression levels of pluripotency and epiblast-specific markers normalized to ESCs. Data are shown as mean with standard deviation. For statistical analysis, multiple t-tests followed by Holm-Sidak multiple comparison test (**b-d**) was performed. Following P-value style was used: ns=not significant, P****<0.0001, P***<0.0002, P**<0.0021, P*<0.0332. Scale bars: 200µm.

Axial morphogenesis of EPI aggregates

Smaller EPI aggregates, placed in low-attachment U-bottom 96-well plates at 72 h, adopted an ovoid shape by 96 h and continued to elongate until 144 h. However, in these structures elongation was not maintained up to 168 h, as aggregates were found to gradually round up, similar to conventional *gastruloids* (**Fig. 4a**, top row). In contrast, bigger EPI aggregates started to elongate later but maintained an elongated morphology at 168 h (**Fig. 4a**, second row). Surprisingly, in the presence of the Wnt inhibitor XAV939, smaller EPI aggregates did not elongate until 120 h, when they massively elongated until 144 h but failed to maintain it until 168 h (**Fig. 4a**, third row). Larger EPI aggregates grown under the same conditions showed a similar behavior, although they maintained elongation until 168 h (**Fig. 4a**, bottom row). Morphological analysis of EPI aggregates grown under the different conditions confirmed that by 168 h, larger EPI aggregates, independent of Wnt activity modulation, were significantly more elongated but smaller compared to *gastruloids* (**Fig. 4b,c**). These results show EPI aggregates can undergo axial elongation even in the absence of exogenous stimulation of Wnt activity, or any other pathway. Since elongation efficiency was higher in larger aggregates composed of initially 100 cells/well size, this condition was chosen for further characterization.

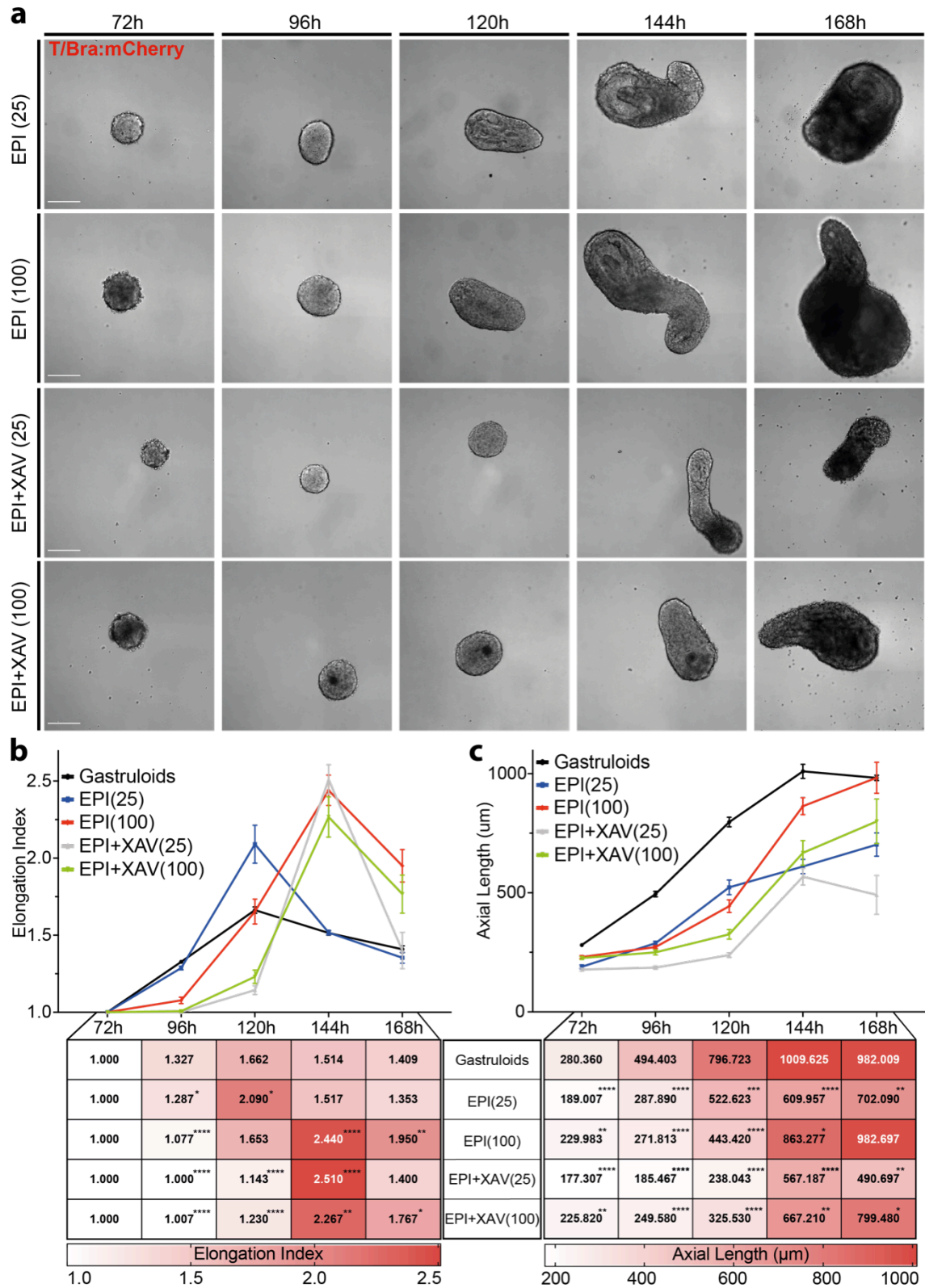


Figure 4: Axial morphogenesis of EPI aggregates. **a)** Time point images showing axial elongation dynamics of EPI aggregates formed under indicated conditions. **b,c)** Quantification of the elongation index (**b**) and axial length (**c**) of EPI aggregates at different timepoints, in comparison to *gastruloids*. Data are shown as mean with standard deviation. For statistical analysis, multiple t-tests followed by Holm-Sidak multiple comparison test was performed. Following P-value style was used: ns=not significant, P****<0.0001, P***<0.0002, P**<0.0021, P*<0.0332. Scale bars: 200μm.

Antero-Posterior patterning in EPI aggregates

Next, we used time-lapse microscopy to assess in selected EPI aggregates the emergence of *T/Bra* expression, as the first gastrulation-related event, as well as their subsequent patterning along an antero-posterior axis. Around 75% of the EPI aggregates initiated *T/Bra* expression between 100 to 105 h of culture (**Fig. 5a**, top panel, **Fig. 5b**). The expression of *T/Bra* was initially uniform across the aggregate and then got restricted to the elongating tip, resembling posterior patterning in *gastruloids* (**Fig. 5a**, top panel). Aggregates grown under Wnt inhibition exhibited a delayed onset of *T/Bra* expression, starting around 120 h (**Fig. 5a**, bottom panel, **Fig. 5c**). In this case, the expression domain of *T/Bra* expression was found to remain rather localized, i.e. did not distribute throughout the aggregate. Moreover, the domain not marking *T/Bra* started to express *Sox1* around 135 h (**Fig. 5a**, bottom panel), suggesting the formation of neural progenitors on the anterior domain of the aggregates. We refer to this asymmetric patterning profile as ‘antero-posterior (A-P) patterning’. At 144 h, the frequency of A-P patterning was highest in the presence of Wnt inhibitor, with $\approx 50\%$ of the aggregates demonstrating posterior *T/Bra* and anterior *Sox1* expression. In contrast, classical *gastruloids* never showed *Sox1* expression anteriorly to *T/Bra* and aggregates formed in EPI medium (*i.e.* without XAV939) exhibiting A-P patterning phenotype only rarely ($\approx 10\%$) (**Fig. 5d**).

At 144 h, these aggregates expressed *Sox1* and *Sox2* at the tail tip, whereas the ones cultured in the presence of Wnt inhibitor exhibited co-localized expression of *Sox1* and *Sox2* on the opposite side of the elongating tip (**Fig. 5e**). In very late structures (168 h) cultured in EPI medium, a larger domain of *Sox2* colocalizing with *Sox1* was detected, still being restricted to its posterior side (**Fig. 6a**). Strikingly, Wnt-inhibited aggregates demonstrated anterior expression of *Sox2* that extended all the way until the tail tip, marking multiple neural ‘rosettes’ on the surface (**Fig. 6b**). In some cases, we observed a *Sox1*-negative *Sox2*-low tissue anterior to these neural rosettes that could correspond to endoderm (*i.e.* foregut) derivatives (**Fig. 6b**, bottom panel). Further characterization via immunostaining for the presence of key markers such as *Pax9*, *Sox17* and *FoxA2*³³ will be necessary to verify this. Taken together, these data suggest that inhibition of Wnt signaling during *in vitro* gastrulation prevents epiblast-like aggregates to uniformly differentiate into mesoderm fate, maintaining their potential to form anterior neural progenitors. At later stages, a domain containing neural progenitors, characterized by co-expression of *Sox1* and *Sox2*, expands to cover almost the entire anterior region of the embryoids.

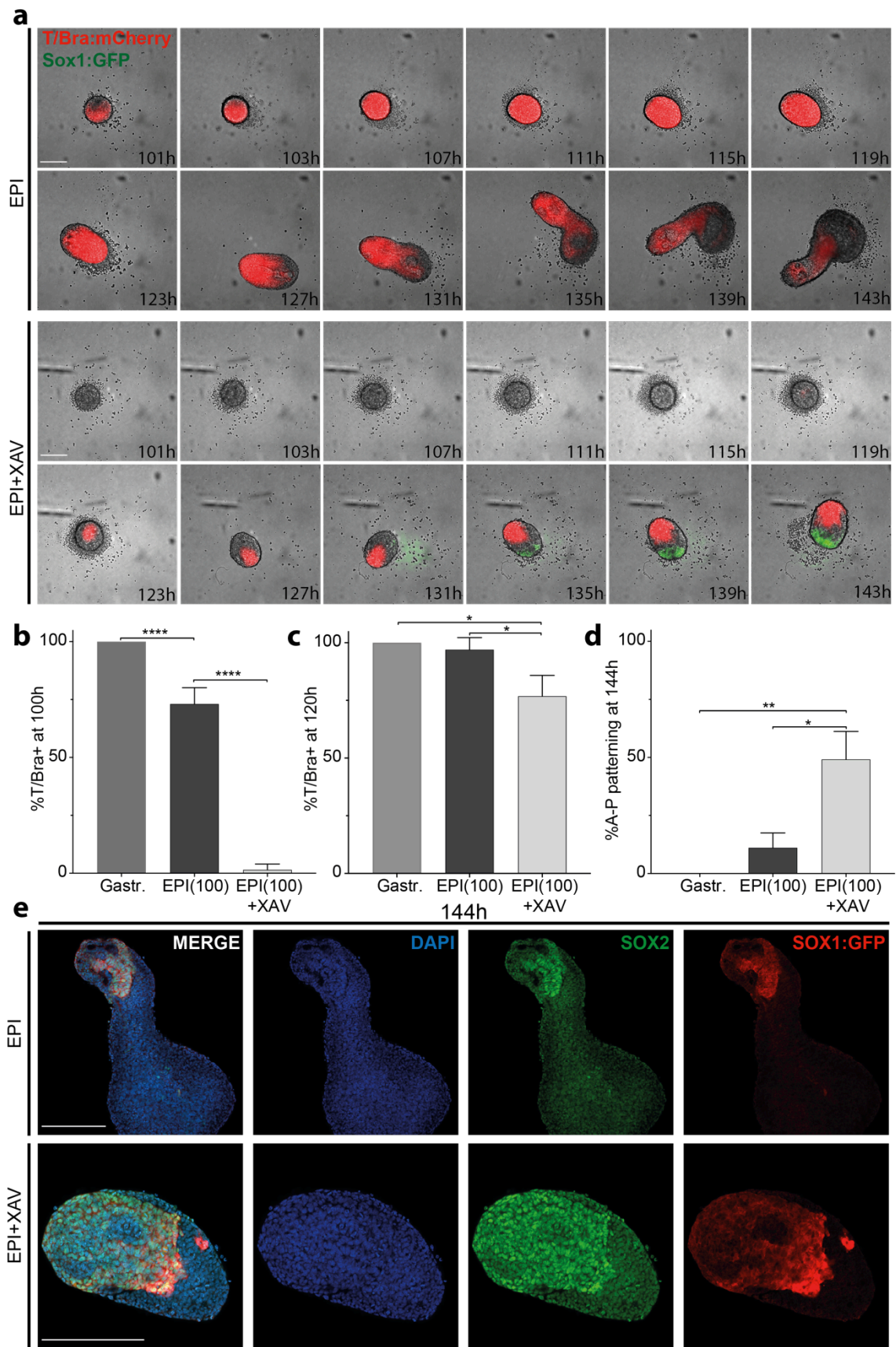


Figure 5: Antero-Posterior patterning in EPI aggregates at 144h. a) Timelapse images showing *T/Bra* and *Sox1* expression dynamics of EPI aggregates formed under indicated conditions. Images were acquired every 2 hours but representative images of 4 hours interval were displayed **b,c)** Percentage of *T/Bra*-positive aggregates at 100h (**b**) and 120h (**c**) of culture. **d)** Quantification of A-P patterning frequency described as aggregates exhibiting *T/Bra* expression and *Sox1* expression on the opposite sides. **e)** Representative confocal images at 144h showing co-localization of *Sox1* and *Sox2* expression in the posterior and anterior domain of aggregates cultured in EPI or EPI+XAV medium, respectively. For statistical analysis, multiple t-tests followed by Holm-Sidak multiple comparison test was performed. Following P-value style was used: ns=not significant, P****<0.0001, P***<0.0002, P**<0.0021, P*<0.0332. Scale bars: 200µm.

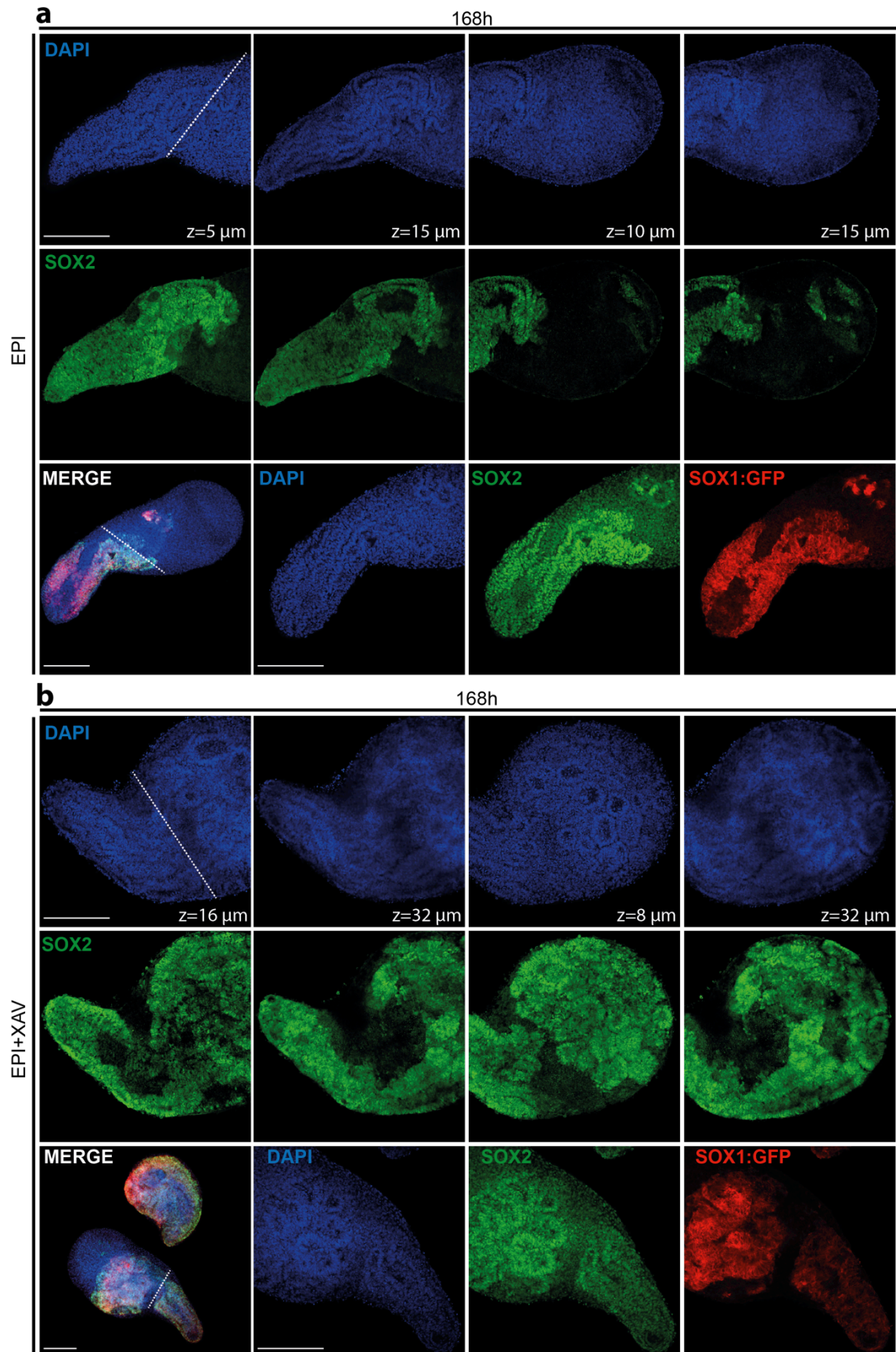


Figure 6: Antero-Posterior patterning in EPI aggregates at 168h. a,b) Representative confocal images at 168h showing *Sox2* (a) and *Sox1* (b) expression in the posterior and anterior domain of aggregates cultured in EPI or EPI+XAV medium, respectively. Dashed lines mark the neck.

High-throughput formation of epithelialized EPI aggregates

To assess whether the presence of an epithelialized structure could play a role in axial patterning, we generated EPI aggregates from 100 cells/well in medium supplemented with soluble (*i.e.* 3%, below the concentration that form a solid gel) Matrigel (**Fig. 7a**). The presence of Matrigel promoted the establishment of an apicobasally polarized and lumenized epithelium (**Fig. 7b**) that exhibited *E-cadherin*⁺ single cell layer with apical *aPKC* expression by 72 h of culture (**Fig. 7c**, left panel). Blebbistatin treatment resulted in loss of columnar epithelium, demonstrating that in these aggregates epithelialization is dependent on myosin II activity³⁴ (**Fig. 7b**, right panel). In smaller aggregates (< 100 cells/well, diameter < 200µm), multiple cavities inside a non-polarized and thick tissue were detected, suggesting a size threshold of EPI aggregates for efficient epithelialization (**Fig. 7d**). In line with earlier studies^{16,20}, Matrigel was found to be crucial for epithelialization, as in its absence EPI aggregates were smaller and disorganized, featuring multiple cavities (**Fig. 7e**). Epithelialized EPI aggregates maintained the expression of the pluripotency markers *Oct4*, *Sox2*, *Nanog* and upregulated the epiblast-specific marker *Otx2* (**Fig. 7f**). Furthermore, qRT-PCR analysis revealed an epiblast identity of epithelialized EPI aggregates, suggesting that addition of Matrigel did not alter the differentiation potential of aggregated mESCs (**Fig. 7g**).

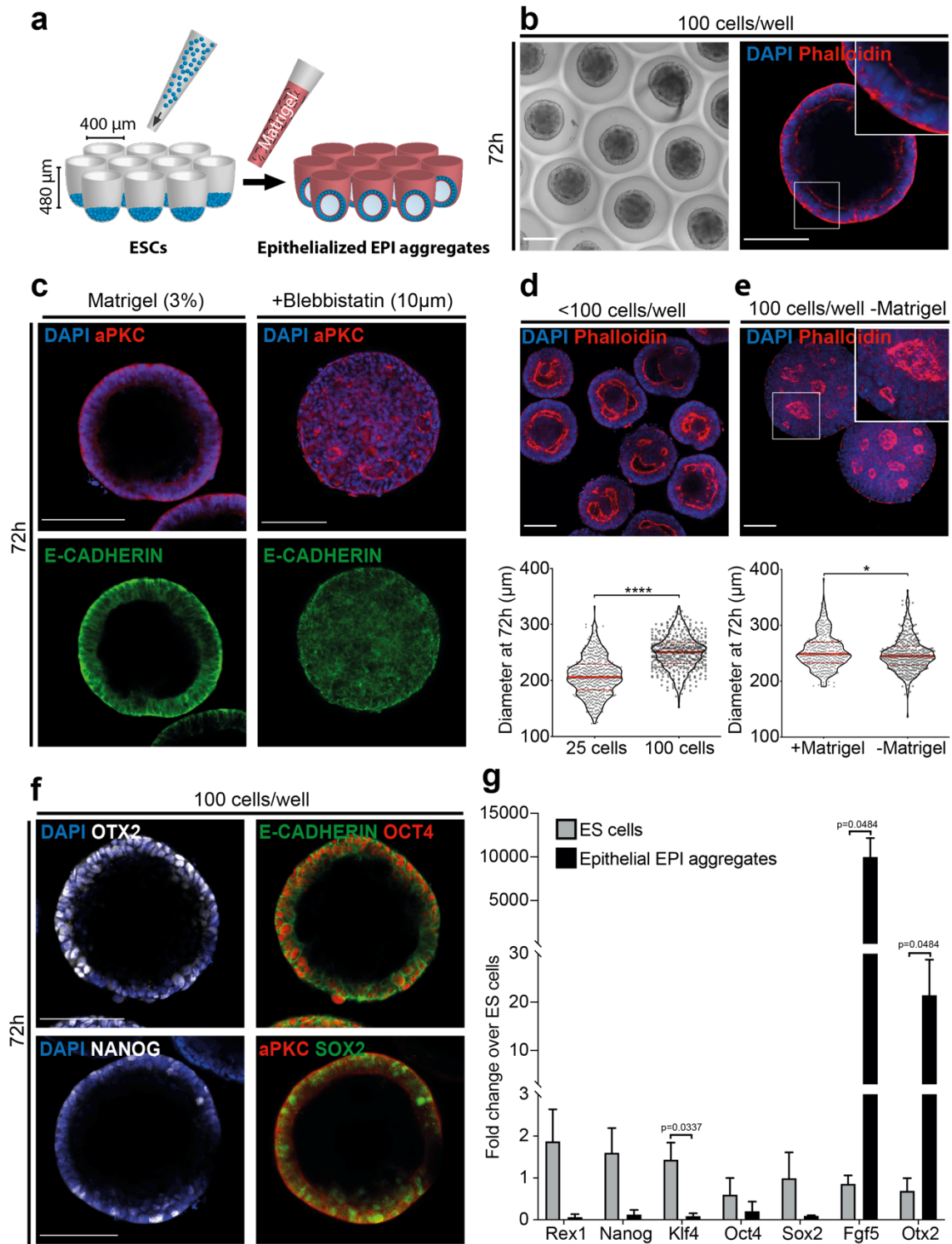


Figure 7: Formation of epithelialized EPI aggregates on PEG microwell. **a)** Schematic showing the experimental method to generate epithelial EPI aggregates on PEG microwells from mESCs. **b)** Representative image of epithelial EPI aggregates on microwells at 72h. Scale bar: 200µm. Confocal image of an EPI aggregate formed with Matrigel at 72h showing single cell layer epithelium and apicobasal polarity as evidence by apical phalloidin staining. Scale bar: 100µm. **c)** Confocal images showing aPKC and E-cadherin immunostaining in epithelial EPI aggregates at 72h treated with or without 10µm blebbistatin between 0-72h. Scale bars: 100µm. **d)** Aggregates generated from 25 cells/well showing multiple phalloidin labeled cavities and incomplete epithelialization at 72h (top). Scale bar: 100µm. Diameter quantification of aggregates formed from 25 cells/well and 100 cells/well (bottom). **e)** Aggregates formed without Matrigel showing multiple phalloidin labeled foci at 72h but no epithelium was formed (top). Scale bar: 100µm. Diameter quantification of aggregates formed with or without Matrigel (bottom). **f)** Confocal images of epithelial EPI aggregates formed from 100 cells/well with Matrigel fixed at 72 hours showing expression of *Otx2*, *Oct4*, *Sox2* and *Nanog* in the *E-cadherin*⁺ *aPKC*⁺ epithelium. Scale bars: 100µm. **g)** qRT-PCR analysis of epithelial EPI aggregates at 72 h formed from 100 cells/well showing expression levels of pluripotency and epiblast-specific genes normalized to ESCs. Data are shown as mean with standard deviation. For statistical analysis, two-tailed unpaired Student's t-test (**c,d**) or multiple t-tests followed by Holm-Sidak multiple comparison test (**g**) was performed. Following P-value style was used: ns=not significant, P****<0.0001, P***<0.0002, P**<0.0021, P*<0.0332.

Axial morphogenesis and A-P patterning of epithelialized EPI aggregates

Previous experiments suggested a correlation of initial aggregate size and axial elongation potential in non-epithelialized EPI aggregates. To test whether such a correlation applies to epithelialized EPI aggregates as well, we generated these tissues at variable size, ranging from 100µm to 270µm (**Fig. 7**). After transferring to 96-well plates in N2B27 medium at 80 h of culture, we observed a range of phenotypes that depended on the initial aggregate size (**Fig. 8a**). Aggregates with a diameter above 250µm generally remained spherical (termed 'spheroids') and maintained an epithelialized architecture, as evidenced by an intense SiR-actin signal marking the F-actin on the apical side at 144 h (**Fig. 8a**, top panel). Interestingly, aggregates with a diameter below 180µm also maintained apicobasal polarity and failed to elongate (**Fig. 8a**, bottom panel). In contrast, epithelialized EPI aggregates with initial diameter between 180 and 250µm efficiently elongated at 144 h (**Fig. 8a**, second/third panel, **Fig. 8b,c**). Within this time interval, we observed an inverse relationship between a well-established epithelium and the potential for elongation: in the presence of a complete epithelium (**Fig. 8a**, second panel), elongation efficiency was decreased, whereas aggregates containing an incomplete epithelium (*i.e.* multiple F-actin foci) elongated more efficiently (**Fig. 8a**, third panel). These results suggest that the initial aggregate size and the resulting extent of epithelialization are major determinants for the axial elongation of epithelialized EPI aggregates.

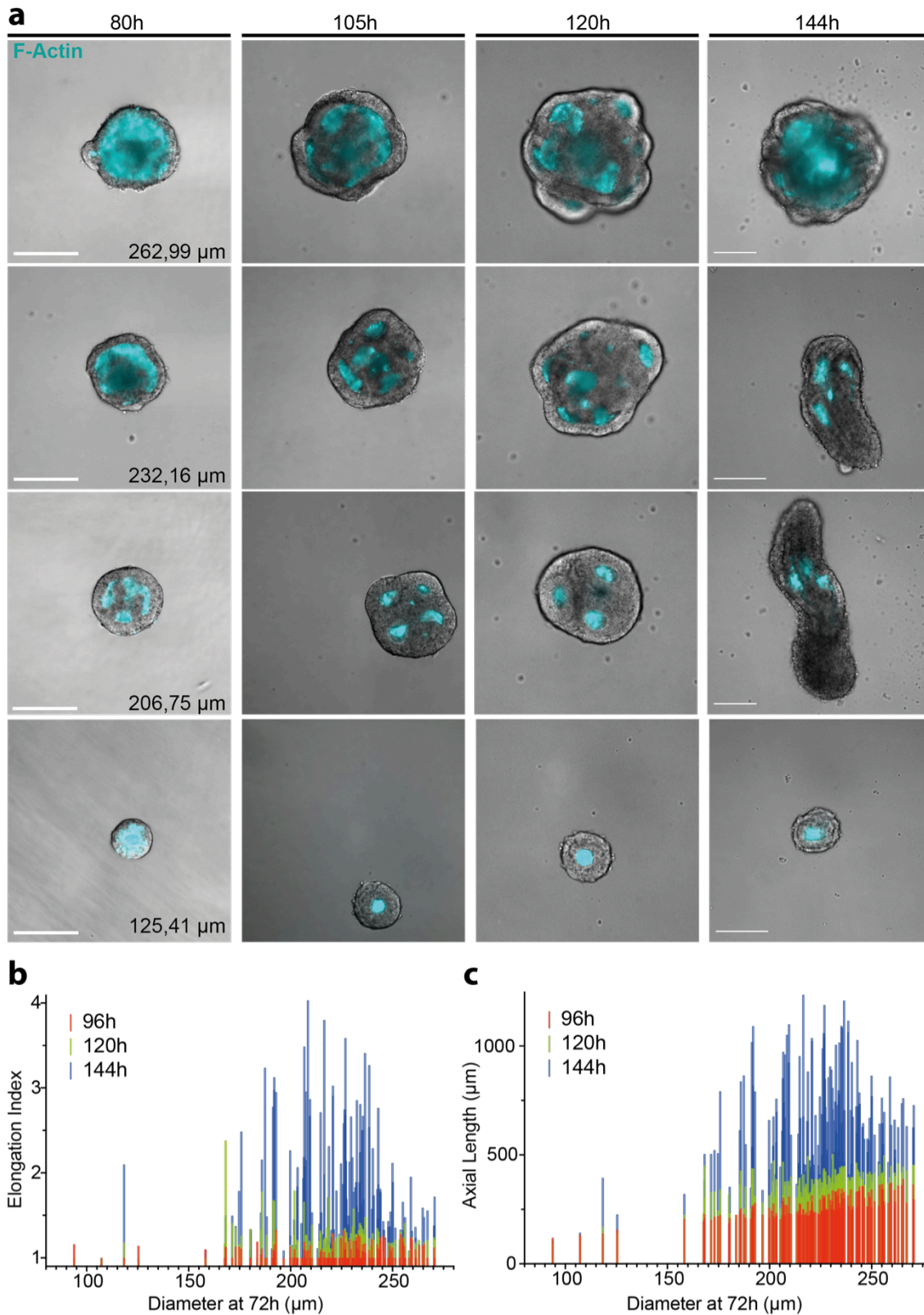


Figure 8: Axial morphogenesis of epithelial EPI aggregates. **a)** Timepoint images showing axial elongation dynamics of EPI aggregates formed from aggregates of various initial diameters as indicated. **b,c)** Quantification of the elongation index (**b**) and axial length (**c**) of EPI aggregates at 96h, 120 and 144h. Scale bars: 200 μm .

Next, we monitored the dynamics of *T/Bra* expression in developing epithelialized EPI aggregates. At 100 h, none of the aggregates showed expression of *T/Bra* (data not shown). By 120 h, larger aggregates showed a restricted domain of *T/Bra* expression. Interestingly, as the initial aggregate size got smaller, the domain of *T/Bra* increased (**Fig. 9a,b**). However, below a diameter of 180µm, *T/Bra* expression was not initiated in epithelialized EPI aggregates. Furthermore, *T/Bra*⁺ cells were found in locations where epithelialization was impaired, as evidenced by lack of F-actin signal. This suggests a requirement of epithelial breakdown to initiate *T/Bra* expression, reminiscent of epithelial-to-mesenchymal transition during gastrulation (**Fig. 9a**, middle panel). Notably, aggregates that failed to undergo axial elongation at 144 h were found to adopt a neural fate, as evidenced by uniform expression of *Sox1*. In contrast, aggregates that maintained an epithelium and could initiate *T/Bra* expression at 120 h, further elongated to give rise to an A-P patterned structure (**Fig. 9a**, second column). Conversely, aggregates that had lost an epithelialized architecture at 120 h elongated to give rise to posterior patterning (**Fig. 9a**, third column). We identified that A-P patterned structures tend to originate from aggregates that had an initial diameter between 225µm-240µm (**Fig. 9c**). In elongated epithelial EPI aggregates, confocal imaging revealed *Sox1*⁺ and *Sox2*⁺ neural rosettes on the anterior domain and with *T/Bra*⁺ cells marking the tip (**Fig. 10a**). Similar to previously characterized EPI aggregates formed in the presence of the Wnt inhibitor XAV939 (**Fig. 6b**), these elongated EPI aggregates in some cases featured non-neural tissues anterior to the rosettes that stained positive for *Sox17*. We also detected *Sox17* expression in a small pocket located at the tail tip, suggesting the involvement of aspects of endoderm development in elongated epithelialized EPI aggregates (**Fig. 10b**).

Altogether, these data suggest that the presence of an epithelium in the starting EPI aggregate is important for subsequent anterior neural commitment. However, in the presence of a complete epithelium, elongation is impaired and hence A-P patterning efficiency reduced. An initial aggregate size of around 225µm was identified that resulted in an intermediate level of epithelialization, promoting the emergence of anterior neural progenitors in the context of an axially elongating entity.

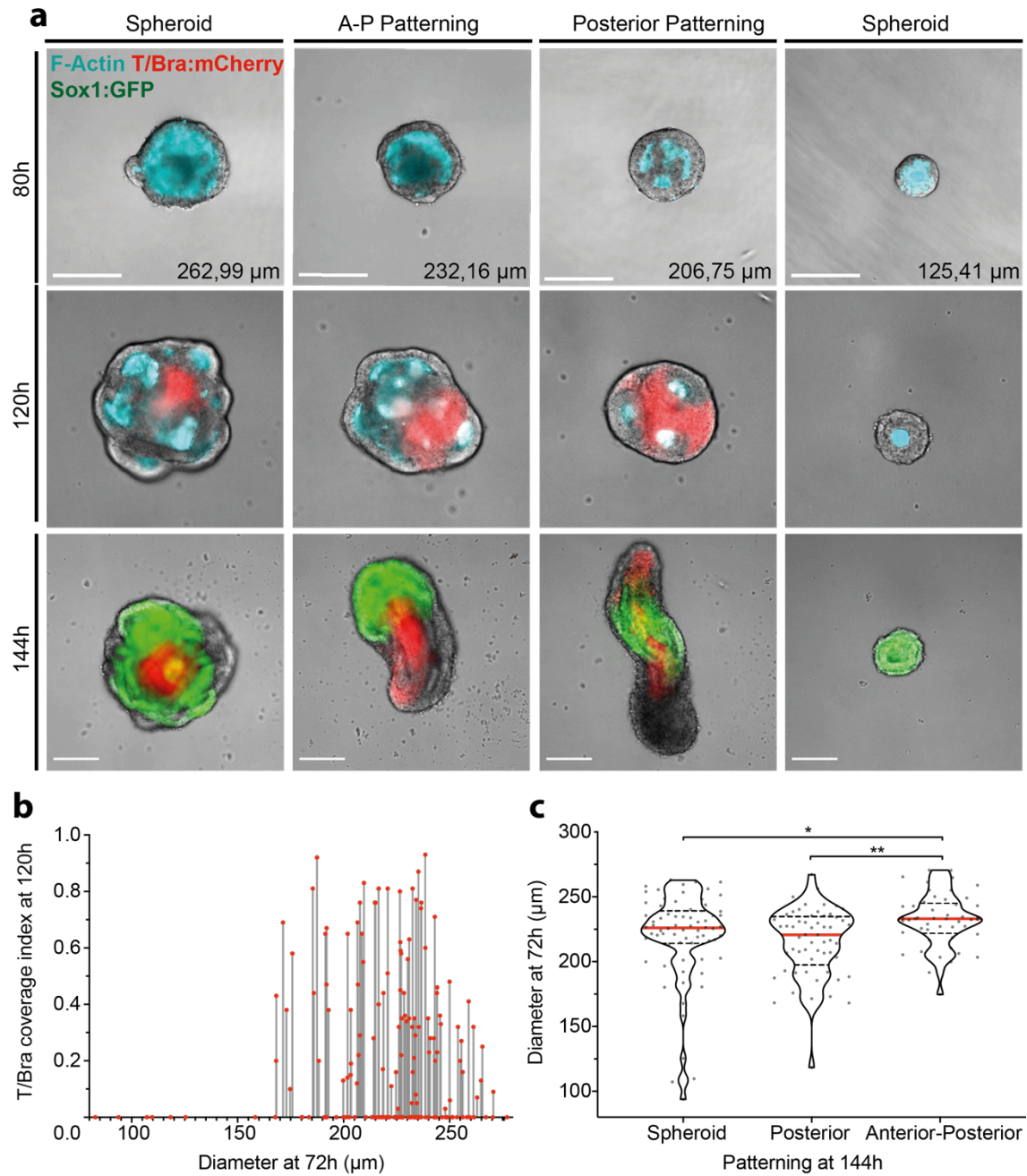


Figure 9: Antero-Posterior patterning in epithelial EPI aggregates at 144h. a) Timepoint images showing F-actin, *T/Bra* and *Sox1* expression dynamics of developing epithelial EPI aggregates of various sizes. **b)** *T/Bra* index of epithelial EPI aggregates at 120h plotted against the initial aggregate diameter at 72h. **c)** Quantification of the initial aggregate diameter of the spheroid, posterior patterned and A-P patterned epithelial EPI aggregates at 144h. Data are shown as median. For statistical analysis, one-way ANOVA followed by Bonferroni multiple comparison test was performed. Following P-value style was used: ns=not significant, P****<0.0001, P***<0.0002, P**<0.0021, P*<0.0332. Scale bars: 200μm.

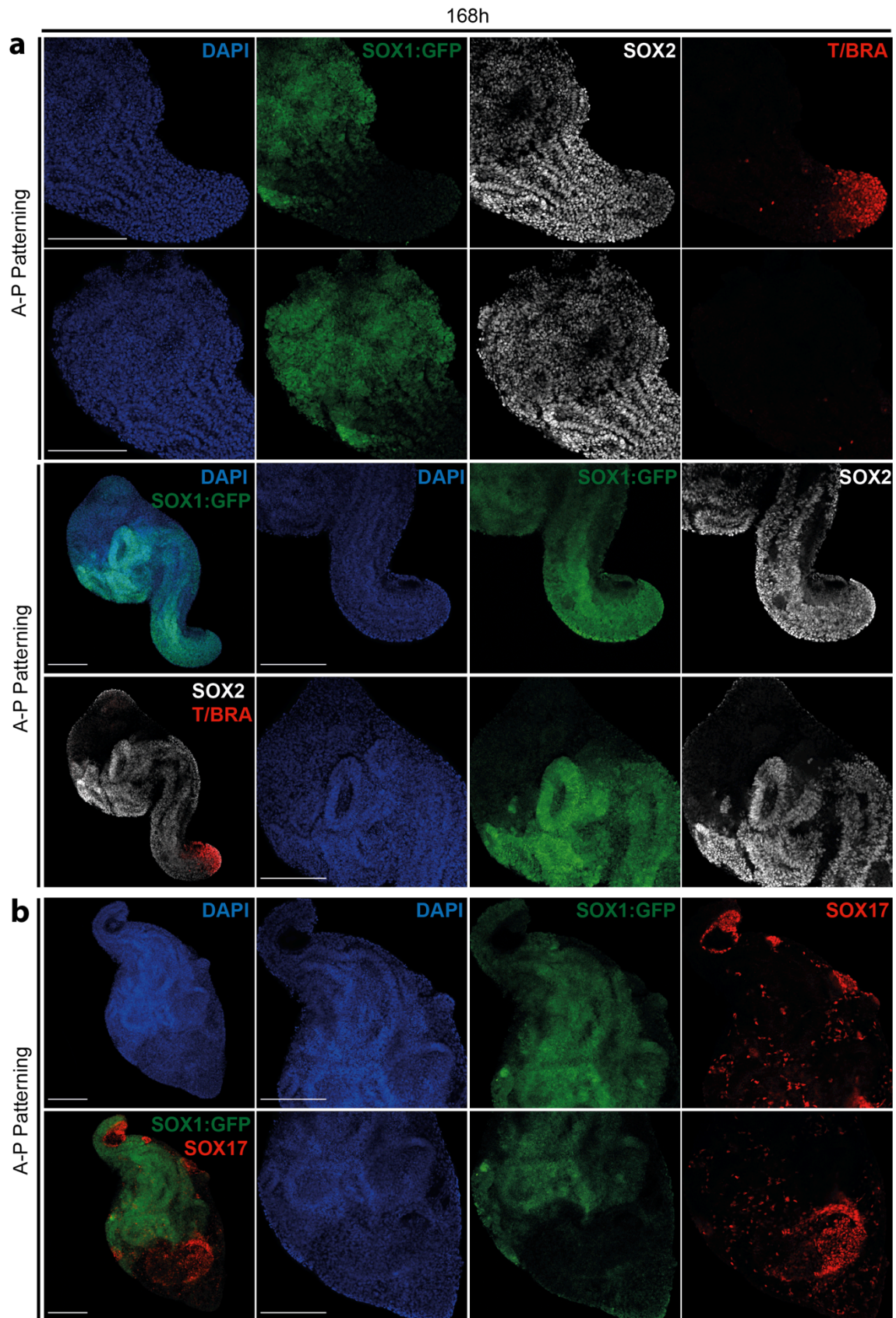


Figure 10: Antero-Posterior patterning in epithelial EPI aggregates at 168h. **a)** Representative confocal images at 168h showing co-localization of *Sox1* and *Sox2* expression extending from posterior to anterior and *T/Bra* expression at the posterior domain. **b)** Representative confocal images at 168h showing *Sox17* expression at the tail and at the anterior-most domain beyond *Sox1*+ neural tissue.

Epithelium sets a threshold of response for *T/Bra* expression and axial elongation

The above experiments suggested that a complete epithelium in EPI aggregates could set a threshold of response for *T/Bra* expression and subsequent axial elongation, where as incomplete epithelialization could exhibit lower threshold and promote self-organization to initiate elongation and patterning. We hypothesized that one strategy to lower this threshold in EPI aggregates with a complete epithelium would be by concentrating the autocrine and paracrine signaling factors secreted by the aggregates themselves by reducing the culture medium volume. To do so, we cultured EPI aggregates of variable size (initial diameter 220-260µm) from 72 h onwards in either 100µl or 190µl culture medium. At 120 h, aggregates cultured in 100µl medium were significantly bigger than the ones cultured in larger volumes (**Fig. 11a**). Moreover, ≈80% of the aggregates cultured in 100µl volume initiated *T/Bra* expression at 120 h, whereas those in 190µl medium only initiated *T/Bra* expression in ≈20% of the cases (**Fig. 11b,c**). Moreover, elongation efficiency was significantly higher in aggregates cultured in smaller volumes (**Fig. 11d,e**). Lowering the culture medium volume yielded A-P patterning efficiencies of 50% and 30% at 144h and 168h, respectively. Aggregates cultured in 190µl remained as spheroids and adopted neural fate (**Fig. 11f**). These data demonstrate an increased threshold of response in epithelial EPI aggregates that could be surpassed by concentrating the cell-secreted factors via volume changes.

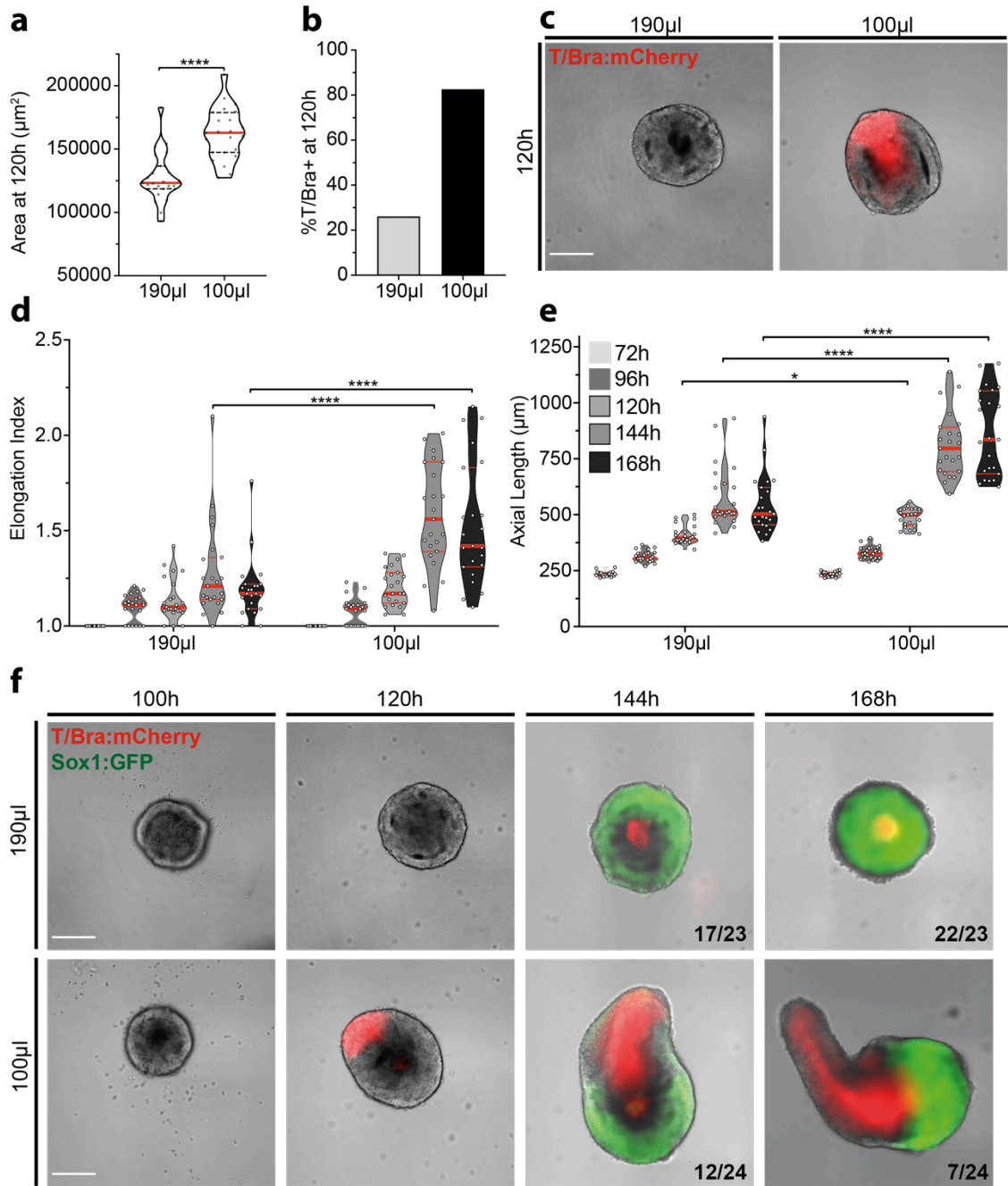


Figure 11: Lowering culture medium volume allows more efficient axial elongation and A-P patterning. **a)** Size quantification of aggregates cultured in either 190µl or 100µl at 120h. **b)** Quantification of *T/Bra*-positive EPI aggregates in either medium volume at 120h. **c)** Representative images showing *T/Bra* expression at 120h. **d,e)** Quantification of elongation index (**d**) and axial length (**e**) of epithelial EPI aggregates cultured in either medium volume at different timepoints. **f)** Representative images at different timepoints showing emergence of *T/Bra* and *Sox1* in aggregates cultured in either 190µl or 100µl. For statistical analysis, two-tailed unpaired Student's t-test (**a**) or two-way ANOVA followed by Bonferroni multiple comparison test (**d,e**) was performed. Following P-value style was used: ns=not significant, P****<0.0001, P***<0.0002, P**<0.0021, P*<0.0332. Scale bars: 200µm.

Discussion

We report a new model system to derive post-implantation epiblast-like structures by aggregation and pretreatment of mESCs. We formulated a serum-free epiblast-induction medium comprising Activin-A (Tgf- β agonist), Fgf2 (Fgf agonist) and knockout serum replacement which promoted the acquisition of epiblast identity of mESC aggregates, followed by their spontaneous symmetry breaking and subsequent morphogenesis without any external Wnt stimulation. Accordingly, mouse embryos that lack *Wnt3* specifically in the posterior visceral endoderm break symmetry, initiate gastrulation and form a primitive streak, suggesting an autonomous developmental potential of epiblast cells that is independent of an extra-embryonic Wnt source³⁵. It is conceivable that in our EPI aggregates, a critical level of Wnt signaling might be achieved by synergistic activities of Tgf- β and Fgf pathways as previously shown¹⁹, which in return could trigger *T/Bra* expression^{2,36}. Indeed, in 72 h EPI aggregates, a TCF/LEF complex reporter revealed homogenous Wnt activity (data not shown). When *Wnt3* was exclusively knocked out in epiblast cells, the mutant embryos demonstrated detrimental defects at later stages, as they were resorbed by E9.5³⁷. Similarly, conventional *gastruloids* show a dependence for Wnt signaling for the later stages such as axial elongation². It is likely that elongation of EPI aggregates could be dependent on Wnt signaling as well. We have shown that inhibition of Wnt by XAV939 during the first 72 h does not have a significant effect on elongation at later time points. Nevertheless, inhibiting the Wnt pathway at later stages could potentially influence axial elongation of EPI aggregates.

Similar to *gastruloids*, EPI aggregates demonstrated posterior patterning with neural tissues localized to the elongating tip. This might be due the fact that that endogenous Wnt activity levels in EPI aggregates at early stages was above a threshold to result in uniform mesoderm conversation (*i.e.* *T/Bra* expression) that yielded to loss of anterior neural progenitors. Accordingly, Osteil *et al.* showed that embryos with increased Wnt activity lose these progenitors and replace them with mesoderm derivatives instead. In this work⁶, treatment with the Wnt inhibitor IWP2 resulted in a more homogenous epiblast stem cell population and yielded an increased differentiation capacity towards ectoderm derivatives. In support of this, in our model, early Wnt inhibition by XAV939 allowed higher levels of *Sox2* and *Nanog* expression, in comparison with aggregates cultured in EPI medium alone. This could indicate a prolonged epiblast identity with an increased potential to differentiate into both anterior neural and posterior mesoderm fate. In Wnt-inhibited EPI aggregates, we observed emergence of neural progenitors (*Sox1+Sox2+*) located anteriorly to *T/Bra* expressing tip, a phenomenon that

not been reported for *gastruloids*. Future work should characterize the tissues generated by these anterior neural progenitors to investigate whether forebrain, midbrain and/or hindbrain-like structures could be achieved.

We have identified an alternative approach to derive anterior neural progenitors by introducing an epithelium in the EPI aggregates. As in the embryo^{12,13}, in our system, the epithelium served as a source for the emergence of anterior neural progenitors. However, we identified the importance of an intricate balance between a well-established epithelium and elongation efficiency. We noticed that cells needed to break down this epithelium in order to contribute to axial elongation. In cases of larger aggregates that were found to be more epithelialized, epithelial breakdown was impaired and tissues adopted primarily a neural fate. We postulate that the epithelium acts as some sort of barrier for the initiation of gastrulation-like events. This barrier can be overcome either by starting with EPI aggregates that feature lower epithelialization levels or else by reducing the cell culture volumes. The latter could concentrate autocrine and paracrine-signaling factors that might help to surpass the threshold set by an intact epithelium. Both approaches resulted in an increased elongation and A-P patterning efficiency. Intriguingly, previous attempts with mouse embryos showed an enhanced development of when embryos are cultured in groups or in low volumes of medium^{38,39}. Future experiments that allow a more targeted break down of the epithelium, e.g. by local administration of Wnt agonists or actomyosin inhibitors such as blebbistatin, to promote epithelial-to-mesenchymal transition (EMT) might allow to reach intermediate levels of epithelialization that could facilitate enhanced axial elongation and A-P patterning. Moreover, an in-depth characterization of endoderm-derived tissues is needed as preliminary data showing anteriorly and posteriorly located *Sox17*⁺ cells might correspond to foregut and hindgut endoderm, respectively. Finally, a thorough analysis of cell types within the different EPI aggregates via single cell RNA sequencing will be informative to reveal the identity and potential of progenitors and the types of tissues that they could generate.

Materials and Methods

Cell culture

Mouse embryonic stem cells (SBr line⁴⁰) were cultured at 37°C in 5% CO₂ in medium composed of DMEM+Glutamax (#61965-026), 10% ES cell-qualified FBS (#16141-079), 1mM sodium pyruvate (#11360-070), 1x MEM non-essential aminoacids (#11140-035), 0.1mM 2-mercaptoethanol (#31350-010) and 1000u/ml Pen/Strep (#15140-122) supplemented with 3µM GSK3i (#361559), 2µM MEKi (#S1036) and 0.1µg/ml LIF (in house preparation). Cells were routinely passaged every 2-3 days by seeding 8000-9000 cells/cm² and every 20 passages a fresh vial was thawed. Cells were tested and confirmed free of mycoplasma.

Preparing EPI differentiation medium

N2B27 medium was prepared by 1:1 mixing of DMEM/F12+Glutamax (#31331-028) and Neurobasal (#21103-049) with the addition of 0.5x N2 supplement (#17502001), 0.5x B27 supplement (#17504001), 0.5x Glutamax (#35050-038), 1mM sodium pyruvate (#11360-070), 1x MEM non-essential aminoacids (#11140-035), 0.1mM 2-mercaptoethanol (#31350-010) and 1000u/ml Pen/Strep (#15140-122). 12ng/ml Fgf2 (#PMG0035), 20ng/ml Activin-A (#338-AC) and 1% KSR (#10828-010) were added to make final EPI differentiation medium.

Preparing EPI aggregates on PEG microwells

Poly(ethylene glycol) (PEG) microwells with 400µm well diameter (121 wells per array) were prepared on 24-well plates as previously described²⁹. Microwells were equilibrated with 50µl of either EPI differentiation medium 30 minutes at 37°C. Mouse ESCs were dissociated to single cells with Accutase (#A11105-01). Cells were then centrifuged at 1000 rpm for 5 minutes and washed twice with 10 ml N2B27 medium at 4°C. Cells were resuspended in cold EPI differentiation medium and desired cell number per well was further adjusted from the cell suspension. For example, 35µl of the 484,000 cells/ml suspension was added dropwise on microwell arrays to have 100-150 cells/well. Seeding was done at 37°C for 15 minutes. 1 ml of EPI differentiation medium was slowly added from the side of the well. When preparing epithelialized EPI aggregates, growth factor reduced Matrigel (#356231) was diluted in cold EPI differentiation medium to 3% (v/v). The medium was vortexed and 1ml was slowly added from the side of the well, avoiding direct addition from the top of the microwell arrays. Plates were kept at 37°C in 5% CO₂ for at least 72 hours before further processing.

Transferring EPI aggregates to 96-well plates

At 72-80 hours of culture, aggregates on microwell arrays were flushed out and transferred to non-tissue culture treated 10cm plates in 10ml warm N2B27 medium. Single EPI aggregates were picked in 10µl and transferred to low adherent U-bottom 96 well plates (#COR-7007). 180µl of N2B27 medium was added on top. At 96, 120 and 144h hours, 150µl of medium was replaced with fresh N2B27 and EPI aggregates were kept until 168h.

Immunostaining and confocal microscopy

EPI aggregates at different stages were washed with PBS and fixed with 4% PFA for 2 hours at 4°C. PFA was removed by three serial washes of 20 minutes at room temperature. Blocking was performed in blocking solution (PBS+10%FBS+0.3% Triton-X) for 1 hour at room temperature. Primary antibodies were incubated for at least 24 hours at 4°C in blocking solution. Next day, primary antibodies were removed by three serial washes of 20 minutes at room temperature. Secondary antibodies were incubated for 24 hours and next day EPI aggregates were washed and mounted on glass slides in mounting medium. Confocal images were taken using an LSM700 inverted (Zeiss) with EC Plan-Neofluar 10x/0.30 or Plan-Apochromat 20x/0.80 air objectives.

Image analysis

All images were processed using algorithms developed in Image J (version 2.0.0-rc-69/1.52n). Brightfield, GFP (for *Sox1*), and mCherry (for *T/Bra*) channels were used as input. Thresholding and segmentation was performed sequentially for each channel. T/Bra coverage index was calculated by dividing area of the object identified in mCherry channel to the brightfield area. For morphology measurements, bright-field images were thresholded and segmented. Maximum inscribed circle function was used to fit circles in the identified object. Axial length was determined by connecting centers of the fit circles. Elongation index was calculated by dividing axial length to the diameter of the maximum inscribed circle.

References

1. van den Brink, S. C. *et al.* Symmetry breaking, germ layer specification and axial organisation in aggregates of mouse embryonic stem cells. *Development* **141**, 4231–4242 (2014).
2. Turner, D. A. *et al.* Anteroposterior polarity and elongation in the absence of extra-embryonic tissues and of spatially localised signalling in gastruloids: mammalian embryonic organoids. *Development* **144**, 3894–3906 (2017).
3. Beccari, L. *et al.* Multi-axial self-organization properties of mouse embryonic stem cells into gastruloids. *Nature* **562**, 272–276 (2018).
4. Arnold, S. J. & Robertson, E. J. Making a commitment: cell lineage allocation and axis patterning in the early mouse embryo. *Nat Rev Mol Cell Biol* **10**, 91–103 (2009).
5. Kimura, C. *et al.* Visceral endoderm mediates forebrain development by suppressing posteriorizing signals. *Developmental Biology* **225**, 304–321 (2000).
6. Osteil, P. *et al.* Dynamics of Wnt activity on the acquisition of ectoderm potency in epiblast stem cells. *Development* **146**, dev172858 (2019).
7. Merrill, B. J. *et al.* Tcf3: a transcriptional regulator of axis induction in the early embryo. *Development* **131**, 263–274 (2004).
8. Mukhopadhyay, M. *et al.* Dickkopf1 is required for embryonic head induction and limb morphogenesis in the mouse. *Developmental Cell* **1**, 423–434 (2001).
9. Lewis, S. L. *et al.* Dkk1 and Wnt3 interact to control head morphogenesis in the mouse. *Development* **135**, 1791–1801 (2008).
10. Fossat, N. *et al.* Stringent requirement of a proper level of canonical WNT signalling activity for head formation in mouse embryo. *Development* **138**, 667–676 (2011).
11. Rivera-Pérez, J. A., Mager, J. & Magnuson, T. Dynamic morphogenetic events characterize the mouse visceral endoderm. *Developmental Biology* **261**, 470–487 (2003).
12. Cajal, M. *et al.* Clonal and molecular analysis of the prospective anterior neural boundary in the mouse embryo. *Development* **139**, 423–436 (2012).
13. Quinlan, G. A., Williams, E. A., Tan, S. S. & Tam, P. P. Neuroectodermal fate of epiblast cells in the distal region of the mouse egg cylinder: implication for body plan organization during early embryogenesis. *Development* **121**, 87–98 (1995).

14. Lancaster, M. A. *et al.* Cerebral organoids model human brain development and microcephaly. *Nature* **501**, 373–379 (2013).
15. Qian, X. *et al.* Brain-Region-Specific Organoids Using Mini-bioreactors for Modeling ZIKV Exposure. *Cell* **165**, 1238–1254 (2016).
16. Nasu, M. *et al.* Robust formation and maintenance of continuous stratified cortical neuroepithelium by laminin-containing matrix in mouse ES cell culture. *PLoS ONE* **7**, e53024– (2012).
17. Eiraku, M. *et al.* Self-organizing optic-cup morphogenesis in three-dimensional culture. *Nature* **472**, 51–56 (2011).
18. Eiraku, M. *et al.* Self-organized formation of polarized cortical tissues from ESCs and its active manipulation by extrinsic signals. *Cell Stem Cell* **3**, 519–532 (2008).
19. Hayashi, K., Ohta, H., Kurimoto, K., Aramaki, S. & Saitou, M. Reconstitution of the mouse germ cell specification pathway in culture by pluripotent stem cells. *Cell* **146**, 519–532 (2011).
20. Bedzhov, I. & Zernicka-Goetz, M. Self-Organizing Properties of Mouse Pluripotent Cells Initiate Morphogenesis upon Implantation. *Cell* **156**, 1032–1044 (2014).
21. Ranga, A. *et al.* Neural tube morphogenesis in synthetic 3D microenvironments. *Proc. Natl. Acad. Sci. U.S.A.* **113**, E6831–E6839 (2016).
22. Meinhardt, A. *et al.* 3D Reconstitution of the Patterned Neural Tube from Embryonic Stem Cells. *Stem Cell Reports* **3**, 987–999 (2014).
23. Girgin, M. *et al.* Generating Gastruloids from Mouse Embryonic Stem Cells. (2019). doi:10.17863/CAM.37946
24. Beck, F. The role of Cdx genes in the mammalian gut. *Gut* **53**, 1394–1396 (2004).
25. Stemmler, M. P., Hecht, A. & Kemler, R. E-cadherin intron 2 contains cis-regulatory elements essential for gene expression. *Development* **132**, 965–976 (2005).
26. Kanai-Azuma, M. *et al.* Depletion of definitive gut endoderm in Sox17-null mutant mice. *Development* **129**, 2367–2379 (2002).
27. Auda-Boucher, G. *et al.* Staging of the Commitment of Murine Cardiac Cell Progenitors. *Developmental Biology* **225**, 214–225 (2000).
28. Sato, S. *et al.* Conserved expression of mouse Six1 in the pre-placodal region (PPR) and identification of an enhancer for the rostral PPR. *Developmental Biology* **344**, 158–171 (2010).

29. Unzu, C. *et al.* Pharmacological Induction of a Progenitor State for the Efficient Expansion of Primary Human Hepatocytes. *Hepatology* **69**, 2214–2231 (2019).
30. Sumi, T., Oki, S., Kitajima, K. & Meno, C. Epiblast ground state is controlled by canonical Wnt/ β -catenin signaling in the postimplantation mouse embryo and epiblast stem cells. *PLoS ONE* **8**, e63378 (2013).
31. Sugimoto, M. *et al.* A Simple and Robust Method for Establishing Homogeneous Mouse Epiblast Stem Cell Lines by Wnt Inhibition. *Stem Cell Reports* **4**, 744–757 (2015).
32. Turner, D. A., Ru, P., Mackenzie, J. P., Davies, E. & Arias, A. M. Brachyury cooperates with Wnt/ β -catenin signalling to elicit primitive-streak-like behaviour in differentiating mouse embryonic stem cells. 1–19 (2014). doi:10.1186/s12915-014-0063-7
33. Kearns, N. A. *et al.* Generation of organized anterior foregut epithelia from pluripotent stem cells using small molecules. *Stem Cell Res* **11**, 1003–1012 (2013).
34. Ivanov, A. I., Hunt, D., Utech, M., Nusrat, A. & Parkos, C. A. Differential roles for actin polymerization and a myosin II motor in assembly of the epithelial apical junctional complex. *Mol. Biol. Cell* **16**, 2636–2650 (2005).
35. Yoon, Y. *et al.* Extra-embryonic Wnt3 regulates the establishment of the primitive streak in mice. *Developmental Biology* **403**, 80–88 (2015).
36. Berge, ten, D. *et al.* Wnt Signaling Mediates Self-Organization and Axis Formation in Embryoid Bodies. *Stem Cell* **3**, 508–518 (2008).
37. Tortelote, G. G. *et al.* Wnt3 function in the epiblast is required for the maintenance but not the initiation of gastrulation in mice. *Developmental Biology* **374**, 164–173 (2013).
38. Canseco, R. S., Sparks, A. E. T., Pearson, R. E. & Gwazdauskas, F. C. Embryo density and medium volume effects on early murine embryo development. *J Assist Reprod Genet* **9**, 454–457 (1992).
39. Lane, M. & Gardner, D. K. Effect of incubation volume and embryo density on the development and viability of mouse embryos in vitro. *Hum. Reprod.* **7**, 558–562 (1992).
40. Deluz, C. *et al.* A role for mitotic bookmarking of SOX2 in pluripotency and differentiation. *Genes & Development* **30**, 2538–2550 (2016).

CHAPTER IV

BIOENGINEERED EMBRYOIDS MIMIC POST-IMPLANTATION DEVELOPMENT IN VITRO

BIOENGINEERED EMBRYOIDS MIMIC POST-IMPLANTATION DEVELOPMENT *IN VITRO*

Manuscript submitted to Nature Cell Biology

Received September 16, 2019

Mehmet U. Girgin¹, Sylke Hoehnel^{1,4}, Nathalie Brandenburg^{1,4}, Alfonso Martinez Arias²,
Matthias P. Lutolf^{1,3*}

¹Institute of Bioengineering, Faculty of Life Sciences, Ecole Polytechnique Fédérale de
Lausanne (EPFL), Lausanne, Switzerland.

²Department of Genetics, University of Cambridge, Cambridge, UK.

³Institute of Chemical Sciences and Engineering, School of Basic Sciences, Ecole
Polytechnique Fédérale de Lausanne (EPFL), Lausanne, Switzerland.

⁴Current address: Startlab / SUN bioscience, Biopôle, Bâtiment SE-B, Route de la Corniche
5, CH-1066 Epalinges, Switzerland.

*Correspondence to: Matthias P. Lutolf (matthias.lutolf@epfl.ch)

Author contribution: M.U.G. and M.P.L. conceived the study, designed experiments, analyzed data and wrote the manuscript. M.U.G. performed the experiments. S.H. and N.B. developed and fabricated microwell arrays. A.M.A. contributed to study design and data discussion and provided feedback on the final manuscript.

Abstract

The difficulty of studying post-implantation development in mammals has sparked a flurry of activity to develop *in vitro* models, termed embryoids, based on self-organizing pluripotent stem cells (PSC). Previous approaches to derive embryoids either lack the physiological morphology and signaling interactions, or are uncondusive to model post-gastrulation development. Here, we report a bioengineering approach aimed at addressing this gap. A high-throughput cell aggregation approach was employed to simultaneously coax PSCs into hundreds of uniform epiblast-like (EPI) aggregates in a solid matrix-free manner. When co-cultured with trophoblast stem cell (TSC) aggregates, the resulting hybrid structures initiate gastrulation-like events and undergo axial morphogenesis to yield structures, termed *EpiTS embryoids*, with an unprecedented anterior development, including brain-like and pre-placodal ectoderm-like regions. We identify the presence of an epithelium in EPI aggregates as the major determinant for the anterior development seen in *EpiTS embryoids*. Our results demonstrate the potential of *EpiTS embryoids* to study peri-gastrulation development *in vitro*.

Introduction

Attempts to recapitulate early mammalian embryonic development *in vitro* have begun with the introduction of embryoid bodies^{1,2}, aggregates of mouse embryonic stem cells (ESCs) that, when differentiated in serum-containing medium, undergo symmetry breaking and polarized gene expression, albeit in a highly uncoordinated manner³. The confinement of PSCs on circular, adhesive micropatterns in two dimensions allows for more robust cell fate patterning, revealing an astonishing capacity of stem cells to give rise to radially symmetric patterns of cell types from different germ layers^{4,5}. Recently, a more realistic three-dimensional (3D) culture system based on small, free-floating ESCs aggregates, termed *gastruloids*⁶⁻⁹, was developed, that upon Wnt activation can undergo elaborate axial morphogenesis and patterning along the anterior-posterior, dorso-ventral and medio-lateral axes, albeit in the absence of any brain-like structures⁹. Alternative embryoid approaches explored the introduction of other cell types present in the early conceptus, such as trophoblast stem cells (TSC) and extraembryonic endoderm (XEN) cells. Co-culture of these cells with ESCs revealed a striking self-organization capacity to recreate blastocyst-like embryoids called *blastoids*,^{10,11} or pre-gastrulation embryo-like structures referred to as *ETS-* or *ETX-embryos*^{12,13}. When transferred into mouse uteri, *blastoids* were shown to implant and trigger decidualization¹⁰. A newer

version of *blastoids* comprising primitive endoderm cells appears to form structures that resemble post-implantation embryos, but only to a relatively limited extent as they fail to undergo gastrulation-like events¹¹. *ETS-embryos*¹², generated by co-culturing ESCs and TSCs in 3D Matrigel, bypass the implantation stage and display an architecture that is remarkably similar to that of the gastrulating embryo. Nevertheless, the stochastic nature of this culture system – single ESCs and TSCs are mixed together in 3D and only occasionally find each other – limits its applicability for quantitative and/or mechanistic studies. Combination of ESCs and TSCs with XEN cells in an aggregation¹³ or on a shaker¹⁴ platform to generate *ETX-embryos* did not substantially increase the frequency of occurrence of such embryoids (~20% and ~23% of the multicellular structures, respectively). Moreover, *ETX-embryo* development appears to come to an end around the gastrulation stage. Altogether, these pioneering *in vitro* models of early embryo development highlight the remarkable self-organization capacity of embryonic and extraembryonic cells, but thus far are inadequate for the exploration of the extent of self-organization to post-gastrulation stages (*e.g.*, axial morphogenesis and formation of anterior neural regions) in an embryo-like context.

Here we employed a bioengineering approach to build a highly standardized embryoid model that could more realistically capture post-gastrulation development stages, specifically including the currently missing embryonic anterior neural regions, and provide a basis for quantitative studies. We hypothesized that to achieve this, it would be essential to specify starting culture conditions in multicellular aggregates that emulate the post-implantation epiblast, both morphologically and transcriptionally. Specifically, since *in vivo* epiblast epithelialization is crucial for embryo survival until gastrulation^{15,16}, and brain develops from anterior neuroepithelium¹⁷, we speculated that epithelialization of such ‘artificial epiblasts’ could be important. Moreover, since mutant mice that lack extraembryonic ectoderm fail to initiate proper gastrulation¹⁸, we reasoned that addition of an extraembryonic compartment, specifically based on TSCs, would be a requirement for modeling more complete post-gastrulation embryonic development, in line with work from Harrison *et al.*¹².

Considering these design criteria, we conceived an *in vitro* methodology in which highly uniform ESC and TSC aggregates could be reproducibly assembled and further developed. Using bioengineered arrays of cell-repellent hydrogel microwells, we separately generated epithelialized epiblast-like (EPI) aggregates, as well as TSC aggregates mimicking extraembryonic ectoderm, in a highly scalable manner. When assembled together in low-attachment wells in serum-free medium, EPI and TSC aggregates rapidly merged and underwent symmetry breaking similar to gastrulating embryos, as demonstrated by polarized

Brachyury (*T/Bra*) expression at the embryonic-extraembryonic interface. Subsequently, hybrid EPI/TSC structures, termed *EpiTS embryoids*, underwent axial morphogenesis to display patterning along an anterior-posterior axis. Strikingly, in late stage *EpiTS embryoids*, we detected the expression of genes associated with fore, mid and hindbrain, suggestive of the formation of a primitive brain-like region. Our approach enables the generation of embryoids in a highly stereotyped and scalable manner, with independent modulation of physical (e.g. size, epithelial architecture) and biological (e.g. provision of signaling molecules) properties of EPI and TSC aggregates, such as to systematically parse out the role of these parameters in promoting *in vitro* embryogenesis.

Results

High-throughput formation of EPI and TSC aggregates

We aggregated ESCs in arrayed round-bottom microwells composed of non-adhesive PEG hydrogels¹⁹ in epiblast induction medium (comprising Activin-A, bFGF and KSR), supplemented with soluble Matrigel (3%) to induce epithelialization²⁰ (**Fig. 1a**). The microwells allowed us to titrate the average number of cells seeded in each well, resulting in cell aggregates of defined size (**Fig. 1b**). Starting with an average of ~25 ESCs per microwell yielded aggregates with ~200 μm ($sd=35\mu\text{m}$) diameter by 72 h of culture; aggregates formed by seeding ~100 cells reached a diameter of ~250 μm ($sd=30\mu\text{m}$) (**Fig. 1c**). Smaller aggregates demonstrated apical expression of *aPKC* surrounded by a multi-layered *E-cadherin*-positive epithelium suggesting poor epithelialization. Moreover, multiple phalloidin-labeled cavities demonstrated incomplete lumenization (**Fig. 1d**). In contrast, larger aggregates featured a single lumen surrounded by a single layer of *E-cadherin*-positive cells, displaying apical *aPKC* and phalloidin, indicative of the formation of an apico-basally polarized epithelium (**Fig. 1e**). These results suggest that a critical aggregate size needs to be reached in order to form a single cell layer epithelium with a central lumen, a phenomenon reminiscent of epiblast maturation²¹. Notably, in the absence of low percentage Matrigel, no epithelium was formed. Instead, the compact aggregates, composed of *E-cadherin*-positive cells, harbored multiple phalloidin- and *aPKC*-positive cavities (**Fig. 1f**). These data show that polarized epithelial aggregates of defined sizes can be readily generated from ESCs using hydrogel microwell arrays, and confirmed that the provision of Matrigel, likely via $\beta 1$ -integrin-mediated signaling²², is critical for their lumenization and epithelialization.

Next, to test whether epithelial aggregates derived from 100 ESC (**Fig. 1e**) acquired an epiblast identity, we used qRT-PCR to check for the expression of pluripotency and epiblast-specific genes (**Fig. 1g**). Compared to ESCs grown under self-renewal conditions, the aggregates downregulated the expression of the naïve pluripotency factors *Rex1*, *Nanog* and *Klf4*, while the expression levels of *Oct4* and *Sox2*, continuously expressed from pre- to post-implantation epiblast *in vivo*, did not change. The epiblast-specific genes *Fgf5* and *Otx2* were markedly upregulated at 72 h of culture. Immunostaining analysis confirmed the gene expression data, showing expression of *Otx2*, *Oct4*, *Sox2* and *Nanog* in the epithelial tissues (**Fig. 1h**). For simplicity, we refer to these aggregates as epithelial EPI aggregates from here onwards.

In the early embryo, the epiblast develops in conjunction with extraembryonic tissues. Signaling from the extraembryonic ectoderm is involved in specifying the onset of gastrulation, as is evident from embryos failing to form an extra-embryonic ectoderm and do not undergo gastrulation¹⁸. To mimic the extraembryonic ectoderm of the developing conceptus, we used hydrogel microwell arrays to generate TSC aggregates, as done previously with ESCs (**Fig. 1a**). Aggregate size at 72 h was again found to be dependent on the initial cell seeding number (**Fig. 1i**). On average, TSC aggregates were slightly smaller than EPI aggregates; aggregates composed of 25 cells or 100 cells reached a diameter of ~ 180 ($sd=25\mu\text{m}$) μm or 230 ($sd=25\mu\text{m}$) μm , respectively (**Fig. 1j**). qRT-PCR analysis revealed a downregulation of *Cdx2*, *Elf5* and *Eomes*, and an upregulation of *Ap2 γ* compared to non-aggregated TSCs, suggesting that aggregated TSCs lose stem-cell identity and get primed for differentiation²³ (**Fig. 1k**). Immunostaining showed that cells expressing *Cdx2* and *Eomes* were primarily maintained at the periphery, but lost at the core of the aggregates. Unlike EPI aggregates, TSC aggregates grown in the presence of soluble Matrigel (3%) did not lumenize, as evidenced by expression of *E-cadherin* and *aPKC* throughout the aggregate (**Fig. 1l**). Collectively, these data show that by culturing defined numbers of ESCs and TSCs on non-adhesive microwell substrates, we can generate cell aggregates with controlled size and morphology, approximating in their identity the epiblast and extraembryonic ectoderm of the developing conceptus, respectively.

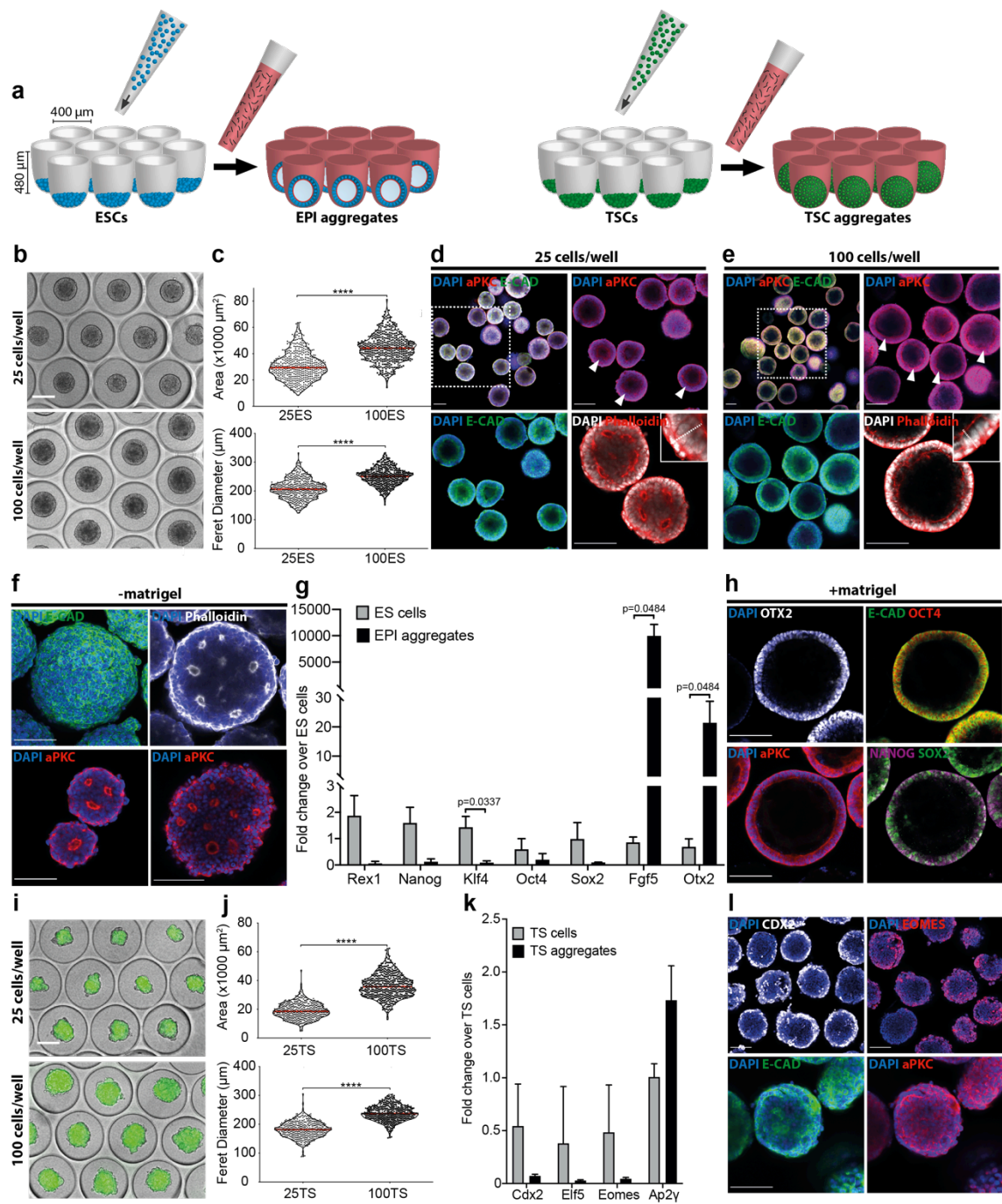


Figure 1: Formation and characterization of EPI and TSC aggregates. **a)** Schematic representation of the workflow showing aggregation of ESCs and TSCs on PEG microwells. **b)** Representative images showing EPI aggregates on microwells at 72 h formed by 25 cells/well (top) or 100 cells/well (bottom). Scale bars: 200µm. **c)** Comparing area (top) and ferret diameter (bottom) features of EPI aggregates at 72 h formed by 25 or 100 cells/well. Data are shown as median. n=479 for 25 ES cells/well and n=439 for 100 ES cells/well. Data is collected from three biologically independent experiments. **d,e)** Confocal images of EPI aggregates formed by 25 cells/well (**d**) or 100 cells/well (**e**) fixed at 72 h and stained for *aPKC*, *E-cadherin* and *phalloidin*. Note multi-layered epithelium in EPI aggregates formed from 25 cells/well compared to single-layer epithelium in EPI aggregates formed from 100 cells/well. Scale bars: 100µm. **f)** Confocal images of non-epithelial aggregates formed by 100 cells/well without Matrigel fixed at 72 h stained for *E-cadherin* (maximum intensity projection), *phalloidin* (z=70µm) and *aPKC*. Nuclei were stained with DAPI. Scale bars: 100µm. **g)** qRT-PCR analysis of EPI aggregates at 72 h formed by 100 cells/well showing expression levels of pluripotency and epiblast-specific genes normalized to ESCs. Data are shown as mean with standard deviation. Data is collected from three biologically independent experiments. **h)** Confocal images of EPI aggregates formed by 100 cells/well with Matrigel fixed at 72 hours showing ubiquitous expression of *Otx2*, *Oct4*, *Sox2* and *Nanog* in the *E-cadherin*-positive epithelium. Nuclei were stained with DAPI. Scale bars: 100µm. **i)** Representative images of TSC aggregates on microwells at 72 h formed by 25 cells/well (top) or 100 cells/well (bottom). Scale bars: 200µm. **j)** Comparing area (top) and ferret diameter (bottom) features of TSC aggregates at 72 h formed by 25 or 100 cells/well. Data are shown as median. n=451 for 25 TS cells/well and n=475 for 100 TS cells/well. Data is collected from three biologically independent experiments. **k)** RT-PCR analysis of TSC aggregates at 72 h formed by 100 cells/well showing expression levels of trophoblast stem cell genes. Data are shown as mean with standard deviation. Data is collected from three biologically independent experiments. **l)** Confocal images of TSC aggregates formed by 100 cells/well with Matrigel fixed at 72 h showing *Cdx2* and *Eomes* expression at the periphery of the aggregates and ubiquitous expression of *aPKC* and *E-cadherin*. Nuclei were stained with DAPI. Scale bars: 100µm. For statistical analysis, two-tailed unpaired Student's t-test (**c,j**) or multiple t-tests followed by Holm-Sidak multiple comparison test (**g,k**) were performed. Following P-value style was used: ns=not significant, P****<0.0001, P***<0.0002, P**<0.0021, P*<0.0332.

Combining EPI and TSC aggregates to form *EpiTS* embryoids

Next, to build a culture system that could promote embryogenesis-like processes, we assembled EPI and TSC aggregates into structures that we termed *EpiTS* embryoids. Individual EPI and TSC aggregates were transferred to U-bottom low-attachment wells (96-well plate) at 72 h where they closely interacted and then fused within a few hours after transfer (**Fig. 2a**). Live imaging revealed that by 120 h, *T/Bra* expression appeared at the aggregate interface. Interestingly, the combination of EPI and TSC aggregates of different size strongly influenced the timing of *T/Bra* expression (**Supplementary Fig. 1a, b**). On the one hand, *embryoids* composed of smaller EPI aggregates initiated *T/Bra* expression generally before 110 h (**Fig. 2b**); by 120 h almost all *embryoids* were *T/Bra*-positive, regardless of the size of TSC aggregates they were fused to (**Supplementary Fig. 1c**). On the other hand, *EpiTS* *embryoids* formed from bigger EPI aggregates showed a delayed onset of *T/Bra* expression (**Fig. 2b**), with 40-60% being *T/Bra*-positive at 120 h and increasing to 90-100% by 144 h (**Supplementary Fig. 1c**). In addition to differences in timing, we measured a strong dependence of EPI aggregate size on the size of the *T/Bra* expression domain, as quantified by the coverage index, corresponding to the area of the *T/Bra* domain divided by the total area of the EPI compartment (**Fig. 2c**). At 120 h *embryoids* formed from smaller EPI aggregates

acquired a dispersed expression of *T/Bra*, covering almost the entire EPI compartment. Conversely, *EpiTS embryoids* formed from bigger EPI aggregates featured a more restricted *T/Bra* expression (**Fig. 2c**, **Supplementary Fig. 1d**) and a larger anterior EPI domain (**Supplementary Fig. 1e**).

Next, we analyzed by immunostaining and confocal microscopy the progression of *EpiTS embryoids* after symmetry breaking, focusing in particular on the onset of gastrulation and epithelial-to-mesenchymal transition (EMT). In the culture condition that yielded the most restricted induction of *T/Bra* expression (100ESC/100TSC), the *E-cadherin*-positive epithelium disappeared in *T/Bra*-positive posterior domain but was maintained on the anterior domain where the cells remained epithelial (**Fig. 2d**, white arrowheads). Moreover, *T/Bra*-positive cells were negative for *laminin* and positive for *Snail* (**Fig. 2d**, white arrowheads), suggesting the involvement of an EMT that precedes the migration from the primitive streak in the embryo²⁴. *Oct4* and *Otx2* expression was maintained throughout the EPI domain. *T/Bra*-positive cells on the posterior showed co-localization with *Oct4* and low levels of *Otx2*. (**Fig. 2e**). However, the expression domain of *Nanog* was more restricted, encircling and co-localizing with *T/Bra* expression. Notably, *Sox2* was mostly expressed on the anterior epithelium and low levels of *Sox2* were detected in the *T/Bra* domain. As the *T/Bra* domain expanded, *Oct4* expression became more restricted on the posterior side, whereas the *Otx2*-positive domain shifted more anteriorly. *Nanog* expression was maintained in a domain encircling *T/Bra* on the posterior side⁵ of the *EpiTS embryoids*, whereas high levels of *Sox2* were maintained in the anterior epithelium (**Supplementary Fig. 1f**). These data suggest that under optimal aggregation (*i.e.* starting with 100 ESCs and 100sTSCs per well) and culture conditions (*i.e.* addition of Matrigel to induce epithelialization in EPI aggregates), *EpiTS embryoids* establish an anterior-posterior axis that resembles the organization of E6.5 embryos. To test whether the extent of *T/Bra* expression was dependent on the epithelial architecture of the aggregates or the presence of extraembryonic compartment, we generated epithelialized (*i.e.* presence of Matrigel) and non-epithelialized (*i.e.* absence of Matrigel) EPI aggregates, and cultured them in the presence or absence of TSC aggregates. Epithelialized EPI aggregates alone could not initiate *T/Bra* expression and required co-culture with TSC aggregates, in contrast to non-epithelialized ones (**Fig. 2f**) that displayed a broad domain of *T/Bra* expression with a small non-expressing region (**Fig. 2g,h**). Overall, these data highlight the importance of an epithelial architecture of the starting EPI aggregate for the restriction of gastrulation-like events to one side of the embryoid, and for the maintenance of an anterior epithelium.

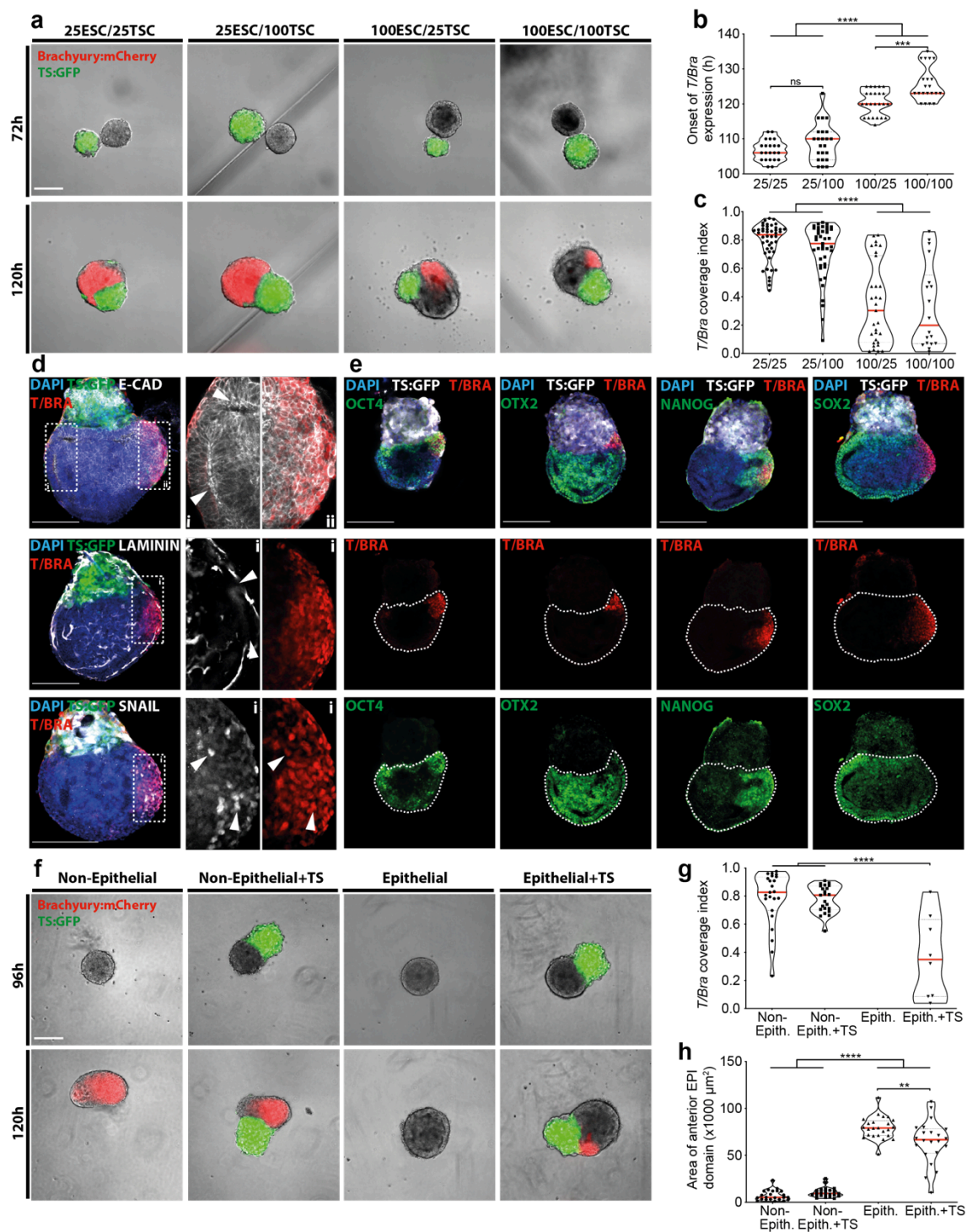


Figure 2: Combination of EPI and TSC aggregates. **a-c)** *T/Bra* expression dynamics in *EpiTS* embryoids formed from different starting cell numbers per well (ESC/TSC). **a)** Representative images showing EPI and TSC aggregates right after transfer at 72 hours and *T/Bra* expression in *EpiTS* embryoids at 120 hours. **b)** Analysis of timelapse between 78h and 149h with 2h interval showing the onset of *T/Bra* expression. For 25/25, 25/100, 100/25 and 100/100 conditions, total number of embryoids analyzed were 22, 23, 24 and 21, respectively. Data is collected from one experiment. **c)** Coverage index of *T/Bra* expression calculated by division of *T/Bra*-positive area to EPI area. Data are shown as median. For 25/25, 25/100, 100/25 and 100/100 conditions, total number of embryoids analyzed were 46, 41, 31 and 18, respectively. Data was collected from two biologically independent experiments. **d,e)** Representative confocal images at 120 hours. Nuclei were stained with DAPI. **d,** GFP-labeled TS cells were depicted in green. *E-cadherin* (top panel) expression showing maintenance of epithelium at the anterior (white arrowheads). Downregulation of *laminin* (middle panel) at the posterior end suggesting basement membrane degradation (white arrowheads). Co-expression of *Snail* (bottom panel) and *T/Bra* marking cells undergoing EMT (white arrowheads) **e,** GFP-labeled TS cells were depicted in gray. *T/Bra* expression marks the onset of gastrulation-like events and co-localizes with *Oct4* and *Nanog*. *Otx2* and *Sox2* expression are mostly detected on the anterior domain. Dashed lines depicting EPI domain **f-h)** *T/Bra* expression dynamics shown in *EpiTS* embryoids formed from non-epithelial or epithelial EPI aggregates with or without TSC aggregates. **f,** Representative images showing *EpiTS* embryoids at 96 hours and expression profile of *T/Bra* at 120 hours. **g,** *T/Bra* coverage index calculated by division of *T/Bra*-positive area to total EPI area at 120h. For Non. Epith., Non. Epith.+TS and Epith.+TS conditions, total number of embryoids analyzed were 23, 23 and 8, respectively. There were no *T/Bra*+ embryoid detected in Epith. condition. Data are shown as median. Data is collected from one experiment. **h,** Area of anterior EPI domain calculated by subtraction of *T/Bra*-positive area from total EPI area. For Non. Epith., Non. Epith.+TS, Epith. and Epith.+TS conditions, total number of embryoids analyzed were 23, 23, 24 and 22, respectively. Data are shown as median. Data is collected from one experiment. For all statistical analysis, one-way ANOVA followed by Bonferroni multiple comparison test was performed. Following P-value style was used: ns=not significant, P****<0.0001, P***<0.0002, P**<0.0021, P*<0.0332. Scale bars: 200µm.

Spontaneous axial morphogenesis of EpiTS embryoids

To assess whether *EpiTS* embryoids formed from epithelial EPI aggregates develop further, we cultured them on U-bottom low-attachment 96 well plates until 189 h without adding additional growth factors. The EPI and TSC aggregates remained fused together and the EPI cells began to elongate from the *T/Bra*-positive end (**Fig. 3a**). *T/Bra* expression tracked the elongation in the form of as medial stripe spanning the length of the aggregate, peaked around 147 h and gradually declined until 189 h, when it became restricted to the elongating tip and then trailed behind in a short stripe of cells (**Fig. 3a-b**). By 168 h, the majority of the *EpiTS* embryoids were reproducibly elongated (**Fig. 3c,d, Supplementary Fig. 2a,b**). Notably, the EPI domain significantly grew over time whereas the size of the TSC aggregates did not change markedly (**Fig. 3e**), suggesting that TSC proliferation is not occurring in the present culture conditions and is not required for the elongation of the EPI domain.

Next, to determine whether the axial morphogenesis is dependent on the co-culture with TSC aggregates and/or the epithelial architecture of the EPI aggregates, we formulated *embryoids* from non-epithelial EPI aggregates (**Fig. 1f**) and compared them to *EpiTS* embryoids formed under optimal conditions. Epithelial EPI aggregates alone remained as spheroids and required TSC aggregates to elongate (**Fig. 3f,g**). Interestingly, non-epithelial EPI aggregates alone could elongate and when co-cultured with TSC aggregates the elongation efficiency was highest at

144 h (**Fig. 3f,g**). Similarly, *embryoids* formed from poorly epithelialized EPI aggregates (**Fig. 1d**) showed more efficient elongation at 144 h compared to *EpiTS embryoids* formed under optimal conditions (**Supplementary Fig. 2c,d**), suggesting a negative correlation between initial presence of an epithelium and axial morphogenesis.

Taken together, these results demonstrate the capacity of *EpiTS embryoids* to spontaneously undergo axial morphogenesis, notably in the absence of any exogenous factor to activate Wnt signaling (e.g. the Wnt agonist CHIR99021) that is critical for the development of other embryoids such as *gastruloids*^{6,7,9}. Furthermore, axial elongation of *EpiTS embryoids* was found to be critically dependent on the epithelial architecture of the EPI aggregate and interaction with the extraembryonic domain.

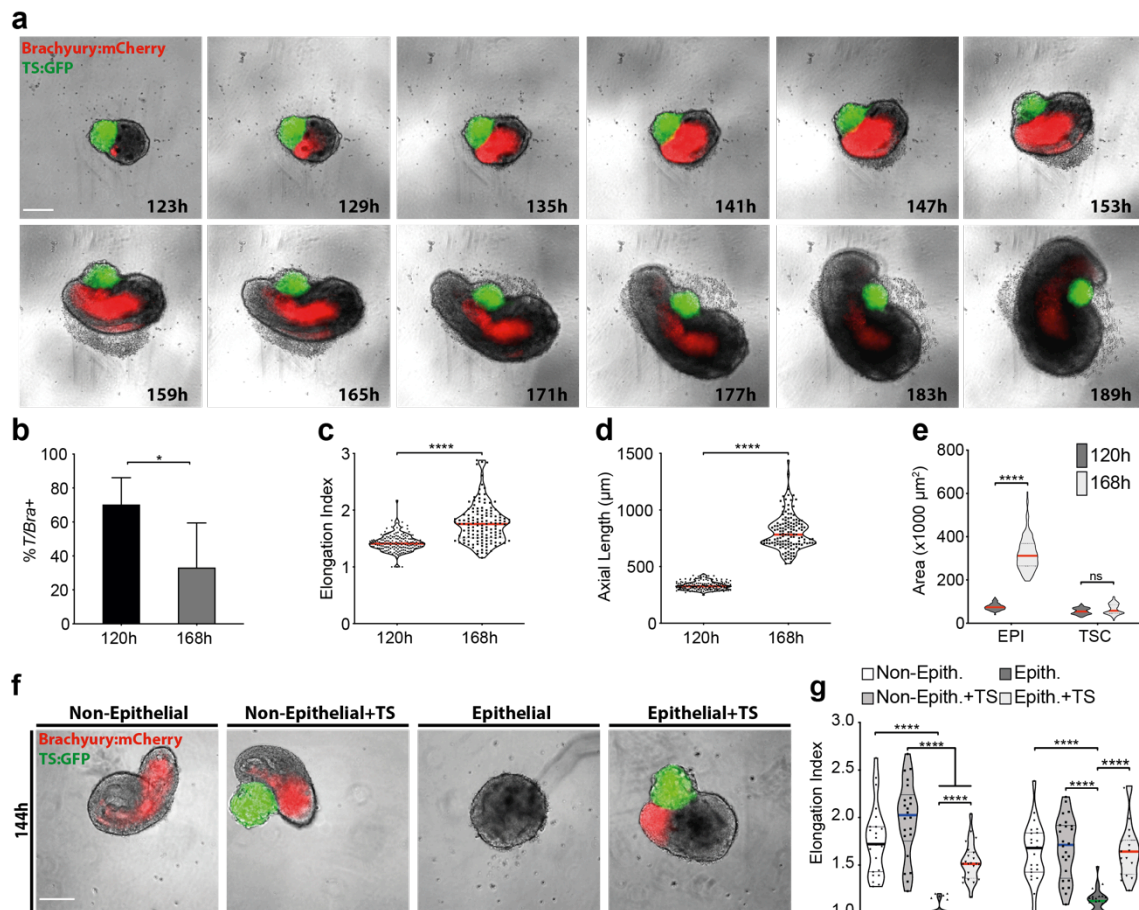


Figure 3: Axial morphogenesis of *EpiTS* embryoids. **a)** Representative time-point images of *EpiTS* embryoids formed from 100ESC/25TSC condition until 189 h. Images were acquired every 2 hours. **b)** Percentage of *T/Bra*-positive *EpiTS* embryoids at 120 h and 168 h. Data are shown as mean with standard deviation. Data is collected from five biologically independent experiments. **c,d)** Morphological measurements of *EpiTS* embryoids formed from 100ESC/100TSC condition showing elongation index (**c**) and axial length (**d**) at 120 h and 168 h. Data are shown as median. n=163 for 120h and n=136 for 168h. Data is collected from five biologically independent experiments. **e)** Area of EPI and TS domains at 120 and 168h. Data are shown as median. n=166 for 120h and n=138 for 168h. Data is collected from five biologically independent experiments. Note that the TSC domain remained the same size whereas EPI domain grew significantly. **f,g)** Characterization of *EpiTS* embryoids at late stages formed from combination of non-epithelial or epithelial EPI aggregates with or without TSC aggregates. **f)** Representative images at 144 h. **g)** Comparison of elongation index between 144 h and 168 h. Data are shown as median. For Non. Epith., Non. Epith.+TS, Epith. and Epith.+TS conditions, total number of embryoids analyzed were 23, 22, 24, 22, respectively at 144h and 23, 24, 22, 23, respectively at 168h. For statistical analysis, two-tailed unpaired Student's t-test (**b-d**) or two-way ANOVA followed by Bonferroni multiple comparison test (**e,g**) were performed. Following P-value style was used: ns=not significant, P****<0.0001, P***<0.0002, P**<0.0021, P*<0.0332. Scale bars: 200µm.

Gastrulation-like events are orchestrated by key early developmental signaling pathways

The onset of gastrulation is the output of asymmetric signaling across the post-implantation epiblast and is tightly regulated by TGF- β , BMP and Wnt signaling pathways²⁵. The activation of these pathways is restricted to the proximal-posterior part of the embryo via secretion of inhibitors from the anterior visceral endoderm²⁶. Therefore, to test whether gastrulation-like processes seen in optimal *EpiTS* embryoids involved similar mechanisms, we inhibited these pathways by adding Lefty (TGF- β inhibitor), Noggin (BMP inhibitor) and Dkk1 (Wnt inhibitor) from 96 h to 120 h, *i.e.* just before the onset of *T/Bra* expression (**Fig. 4**). Treatment with Lefty and Dkk1 resulted in a decreased percentage of *T/Bra*-positive *EpiTS* embryoids by 127 h of culture. Surprisingly, Noggin did not have a significant effect on *T/Bra* expression (**Fig. 4a,b**). Dkk1-treated *EpiTS* embryoids exhibited a delayed *T/Bra* expression compared to non-treated or Noggin-treated ones (median ~140 h versus ~125 h) (**Fig 4c**). Furthermore, we observed a decreased extent of *T/Bra* expression in the presence of these inhibitors, an effect that was more pronounced in the case of Dkk1 and Lefty (**Fig. 4d**). Of note, the treatment with the small molecule inhibitors SB431542 (TGF- β inhibitor), LDN193189 (BMP inhibitor) and XAV939 (Wnt inhibitor) resulted in a dramatic reduction of *T/Bra* expression (**Supplementary Fig. 3a**); SB431542 and XAV939 resulted in a complete loss of *T/Bra* expression, whereas a small percentage of LDN193189-treated *EpiTS* embryoids still expressed *T/Bra* (**Supplementary Fig. 3b**), yet with a domain that was spatially very restricted (**Supplementary Fig. 3c**). Altogether, these results indicate a crucial role of Wnt signaling for the induction, and TGF- β and Wnt pathways for determining the extent of *T/Bra* expression in *EpiTS* embryoids. The BMP pathway was shown to have lesser effect on the dynamics of gastrulation-like events in *EpiTS* embryoids.

We further investigated the effect of the protein inhibitors on axial morphogenesis of late stage (168 h) *EpiTS-embryoids*. Noggin-treated *EpiTS embryoids* were significantly more elongated (**Fig. 4e**) and maintained larger *T/Bra* domains compared to non-treated or Lefty/Dkk1-treated ones (**Fig. 4f**). Moreover, *EpiTS embryoids* treated with Lefty exhibited small clumps of *T/Bra*-positive cells, whereas Dkk-treated ones showed a more scattered expression throughout the body of the structure. Surprisingly, in Noggin-treated *EpiTS embryoids* the longitudinal stripe of *T/Bra* expressing cells was longer and exhibited higher levels of expression (**Fig. 4g**) and were positive for *FoxA2* (**Supplementary Fig. 3d**), reminiscent of a notochord-like structure. qRT-PCR analysis revealed an upregulation of *T/Bra*, *FoxA2* and *Shh* in these Noggin-treated *EpiTS embryoids* compared to non-treated ones (N2B27), indeed suggesting that BMP inhibition may promote aspects of notochord formation (**Fig. 4h**). Dkk1-treatment also resulted in an increased expression of these genes but it was not accompanied by any morphological organization of the *T/Bra* domain (**Fig. 4g**). These results suggest an important early role of TGF- β and Wnt pathways to prime *EpiTS embryoids* for axial morphogenesis. BMP inhibition by Noggin resulted in more elongated morphology and the formation of notochord-like structures, supporting the role of Noggin in proper notochord formation²⁷.

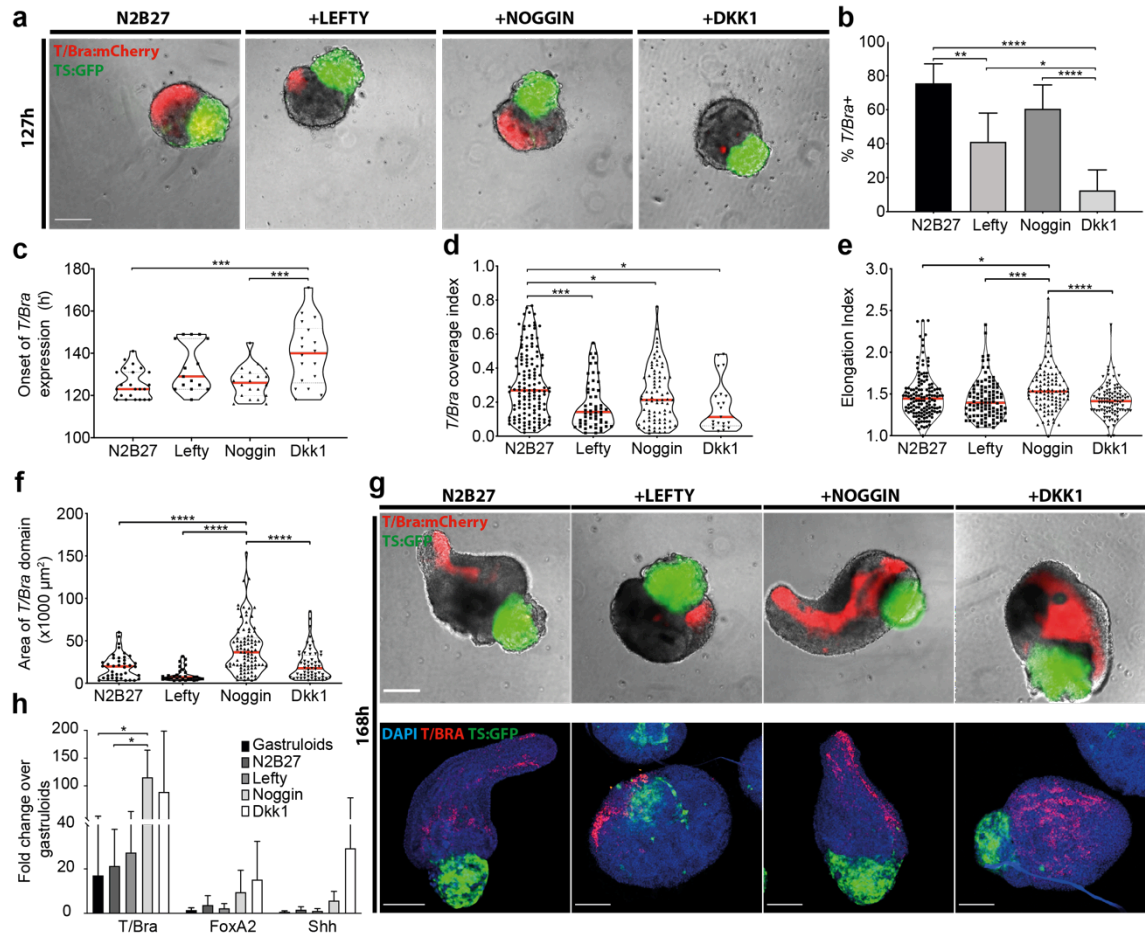


Figure 4: The effect of protein inhibitors of TGF- β , BMP and Wnt signaling pathways on *T/Bra* expression dynamics. a-d) *T/Bra* expression dynamics in *EpiTS* embryoids treated with indicated inhibitors between 96 h and 120 h. a) Representative images at 127 h. b) Percentage of *T/Bra*-positive *EpiTS* embryoids at 120 h. Data are shown as mean with standard deviation. Data is collected from six biologically independent experiments. c) Analysis of time-lapse between 77 h and 189 h with 2 hour interval showing the onset of *T/Bra* expression. Data are shown as median. For N2B27, Lefty, Noggin and Dkk1 conditions, total number of embryoids analyzed were 23, 15, 20 and 18, respectively. Data is collected from one experiment. d) *T/Bra* coverage index calculated by division of *T/Bra*-positive area to total EPI area at 120 h. Data are shown as median. For N2B27, Lefty, Noggin and Dkk1 conditions, total number of embryoids analyzed were 139, 55, 81 and 21, respectively. Data was collected from six biologically independent experiments. e-g) Characterization of *EpiTS* embryoids formed from different inhibitor conditions at 168 h. e, Comparing elongation index. Data are shown as median. For N2B27, Lefty, Noggin and Dkk1 conditions, total number of embryoids analyzed were 140, 104, 105 and 98, respectively. Data was collected from six biologically independent experiments. f, *T/Bra* expression domain. Data are shown as median. For N2B27, Lefty, Noggin and Dkk1 conditions, total number of embryoids analyzed were 40, 31, 92 and 55, respectively. g, Representative wide-field (top panel) and confocal (bottom panel) images showing *T/Bra* expression profile at 168 h. Nuclei are stained with DAPI. GFP-labeled TSCs are shown in green. h) qRT-PCR analysis showing expression levels of notochord genes *T/Bra*, *FoxA2* and *Shh* at 168 h normalized to age-matched gastruloids. Data are shown as mean with standard deviation. Data is collected from three biologically independent experiments. For statistical analysis, one-way ANOVA (b-f) or two-way ANOVA (h) followed by Bonferroni multiple comparison test were performed. Following P-value style was used: ns=not significant, P**<0.0001, P***<0.0002, P**<0.0021, P*<0.0332. Scale bars: 200μm.**

Formation of primitive brain- and pre-placodal ectoderm-like regions in late EpiTS embryoids

Previous studies with *gastruloids* have shown faithful recapitulation of the post-occipital regions of the mouse embryo⁹. *Gastruloids* exhibit spatio-temporal activation of *Hox* gene clusters and develop posterior neural tissue; however, anterior neural regions, such as forebrain, midbrain and hindbrain, are missing⁹. We hypothesized that this might be due to a lack of an epithelium in *gastruloids*, as well as the highly posteriorizing effect of Wnt activation that is applied to initiate *gastruloid* formation. Indeed, embryos with increased Wnt activity fail to form any forebrain/midbrain^{28,29}.

To test this hypothesis, we assessed the presence of key markers expressed in anterior neural regions in *EpiTS embryoids* (**Fig. 5**). *Otx2*, which during development becomes localized to the midbrain by stage E10.5³⁰, was found to be expressed in a large domain adjacent to the extraembryonic domain in *EpiTS embryoids* (**Fig. 5a**). Interestingly, embryoids formed from poorly epithelialized aggregates (**Fig. 1d**) showed little or no expression of *Otx2* at 168 h (**Fig. 5a**), suggesting a potentially important role of the epithelium in the EPI aggregate as a progenitor pool for the formation of anterior neural regions¹⁷. *Sox1*, an early marker of neural progenitors³¹ that is maintained throughout the central nervous system until E9.5³², was found to be expressed spanning from the most anterior domain to the posterior end at the midline (**Fig. 5b**, **Supplementary Fig. 4a**) where it co-localized with *Pax6* (**Supplementary Fig. 4b**). The *Sox1*-positive tissue was flanked by domains staining positive for *Six1*, suggestive of a pre-placodal ectoderm-like (PPE) region³³⁻³⁵ in *EpiTS embryoids* (**Fig. 5c**, **Supplementary Fig. 4c**). In support of this observation, we identified *Otx2*-positive epithelial cavities at the anterior-most region that resemble placode-like structures³⁶ (**Fig. 5d**, white arrowheads). Interestingly, we also detected *Otx2*-positive cells that project from rosettes towards the surface of the *EpiTS embryoid* (**Fig. 5e**), suggesting the presence of differentiated neurons in *EpiTS embryoids*.

A more detailed analysis of anterior neural markers by qRT-PCR revealed striking differences between late *EpiTS-embryoids* and *gastruloids*. *EpiTS-embryoids* had upregulated expression of forebrain (*Emx2*, *Six3*, *Wnt7b*), midbrain (*Otx2*, *Dmbx1*, *En1*, *Pax2*) and hindbrain (*Gbx2*, *Irx3*) markers compared to age-matched *gastruloids* (at 168 h), suggesting a general recapitulation of anterior neural development in *EpiTS embryoids*. Moreover, markers of the central nervous system (*Sox1*, *Sox2*) were also highly upregulated in *EpiTS embryoids*. Notably, *gastruloids* had higher expression of *HoxB4* and *HoxB9* suggesting that neural tissues in *gastruloids* has a more spinal cord identity (**Fig. 5f**), as reported⁹ and, importantly, that *EpiTS embryoids* represent the complementary missing brain structures.

Finally, we explored whether TGF- β , BMP and Wnt signaling pathways may be relevant for the establishment of neural tissues in late *EpiTS embryoids*. Treatment with Lefty and Dkk1 did not result in a change in the size of the *Otx2* expression domain. However, Noggin-treated *EpiTS embryoids* exhibited smaller *Otx2*-positive domains (**Fig. 5g**). qRT-PCR analysis of forebrain, midbrain and hindbrain markers revealed an overall increase in expression levels in Dkk1-treated ones compared to non-treated controls (**Supplementary Fig. 5a-c**), in line with the involvement of Dkk1 in anterior neural development²⁸. Likewise, Lefty treatment resulted in an increased expression of several anterior neural genes such as *Foxg1*, *En1* and *Irx3* (**Supplementary Fig. 5a-c**). Altogether, these data show that our co-culture approach promotes a surprising development of anterior neural and PPE-like regions in *EpiTS embryoids* (**Fig. 5h**).

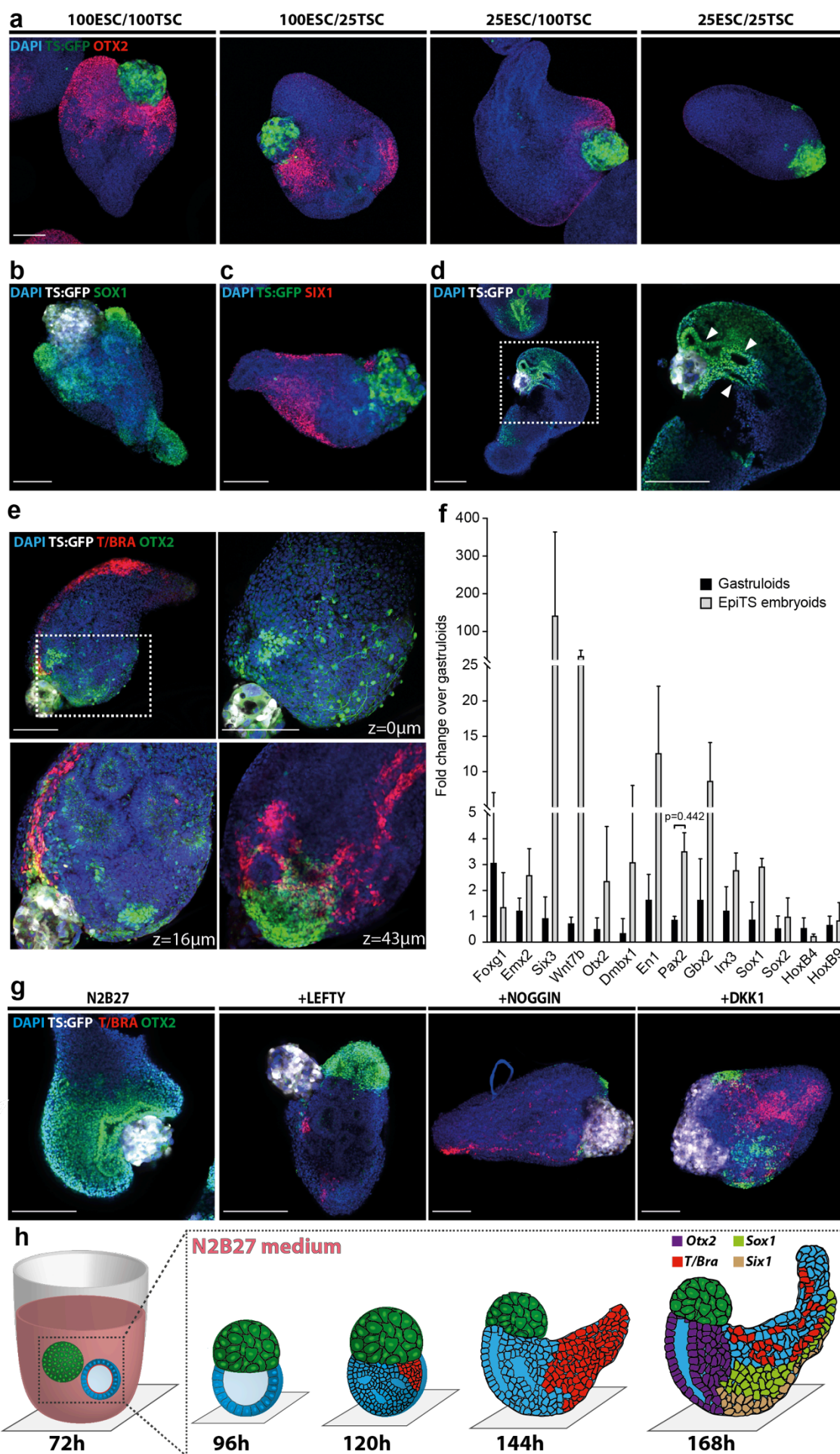


Figure 5: Formation of primitive brain- and PPE-like regions in late stage *EpiTS* embryoids. **a)** Confocal images showing *Otx2* expression at 168h in *EpiTS* embryoids formed from indicated conditions. Nuclei are stained with DAPI. GFP-labeled TSCs are depicted in green **b)** Confocal image showing *Sox1* expression extending along anterior-posterior axis at 168h. Nuclei were stained with DAPI. GFP-labeled TS cells were depicted in gray. **c)** Confocal image showing *Six1* expression flanking the *EpiTS* embryoid at 168 h. **d)** Confocal image showing formation of *Otx2*-positive placode-like domains at 168h. Nuclei were stained with DAPI. GFP-labeled TS cells were depicted in gray. **e)** Confocal image showing *T/Bra* and *Otx2* expression at 168 h. Note the formation of *Otx2*-positive neurons and rosettes at different planes. Nuclei were stained with DAPI. GFP-labeled TS cells were depicted in gray. **f)** qRT-PCR analysis showing expression levels of forebrain (*Foxg1*, *Emx2*, *Six3*, *Wnt7b*), midbrain (*Otx2*, *Dmbx1*, *En1*, *Pax2*), hindbrain (*Gbx2*, *Irx3*), central nervous system (*Sox1*, *Sox2*) and spinal cord (*HoxB4*, *HoxB9*) genes at 168 h normalized to age-matched gastruloids. Data are shown as mean with standard deviation. Data is collected from three biologically independent experiments. **g)** Representative confocal images showing *T/Bra* and *Otx2* expression at 168 h in *EpiTS* embryoids treated with indicated inhibitors between 96 h and 120 h. Nuclei were stained with DAPI. GFP-labeled TS cells were depicted in gray. **g)** Experimental workflow depicting *EpiTS* embryoid formation, initiation of *T/Bra* expression and subsequent axial morphogenesis. In 168 h *EpiTS* embryoids, indicated cell types form reproducibly and get spatially arranged as shown. For statistical analysis, multiple t-tests followed by Holm-Sidak multiple comparison test (**d**) was performed. Following P-value style was used: ns=not significant, P****<0.0001, P***<0.0002, P**<0.0021, P*<0.0332. Scale bars: 200µm.

Discussion

We report a bioengineering effort to generate a novel embryoid culture system for the study of early mouse post-implantation development *in vitro*. Our high-throughput aggregation approach provides precise control over the size and the epithelial architecture of the aggregates, potentially offering an unprecedented modularity for decoupling the role of physical and biological factors involved in early development. The separate derivation of EPI and TSC aggregates before merging allows for an independent modulation of key aspects of the embryonic and extraembryonic compartments, in contrast to previous approaches^{12,13}. This makes our system both experimentally tractable and efficient for quantitative and mechanistic studies.

When EPI and TSC aggregates are assembled together, *EpiTS* embryoids reproducibly express *T/Bra* at a localized domain in the embryonic-extraembryonic interface. We found that the dynamics of this process are highly dependent on the epithelial architecture of the EPI aggregate. Intriguingly, the lack of an epithelium in co-cultured EPI/TSC aggregates results in the extension of *T/Bra* expression throughout the embryonic domain, resembling Wnt gain-of-function mutant mouse embryos²⁹. Previous studies have highlighted the opposing roles of epithelia and Wnt signaling during development³⁷ as recapitulated in our experimental system. Recent experiments on 2D micropatterns demonstrated that E-cadherin-deficient human ESCs did not form an epithelium and exhibited increased levels of Wnt activity that perturbed cell fate patterning³⁸. Therefore, we believe that in our model, a threshold of responsiveness to Wnt activation may explain the counteracting roles of epithelium and *T/Bra* expression.

Epithelialized EPI aggregates would display a higher threshold and could only overcome it when coupled to TSC aggregates, suggesting a biological (*e.g.* through secretion of Wnt/TGF- β ligands) or physical (*e.g.* through cell-cell contact or mechanical forces) influence of TSC aggregates on EPI aggregates. The addition of Dkk1 or Lefty could further increase this threshold, suggesting a contribution from TGF- β signaling for the establishment of a threshold of responsiveness.

The organization of gene expression in the *EpiTS embryoids* suggests an anteroposterior organization similar to that of E6.0 embryos with an ensuing elongation along an axis which mimics an anteroposterior axis. Upon induction of *T/Bra* at the posterior domain, *EpiTS embryoids* were found to reproducibly undergo axial elongation, establishing patterning along an anterior-posterior axis comprising brain- and PPE-like regions. To the best of our knowledge, existing ESCs/TSC-based embryoid models^{12,13} fail to capture such embryo-like axial elongation, likely due to the non-permissive initial culture conditions containing high percentage of serum that might prevent ESCs from efficiently differentiating³⁹. *Gastruloids* on the other hand show very robust axial elongation in serum-free medium in the presence of Wnt agonists, but they recapitulate the post-occipital region of the mouse embryo, not forming any anterior neural regions⁹. In our model, epithelialized EPI aggregates promoted the formation of *Otx2*-positive brain-like regions that are missing in *gastruloids* that are indeed generated from non-epithelialized mESC aggregates. Of note, in contrast to *gastruloids*, we did not detect well-developed mesoderm and endoderm derivatives in *EpiTS embryoids* (data not shown). This could suggest that in our system, the bias towards more anterior development comes at the cost of a somewhat restricted mesoderm and endoderm development. It could be interesting to test whether addition of extraembryonic endoderm cells to *EpiTS embryoids* would increase the formation of endodermal tissue to achieve a more complete body plan.

The importance of an epithelium for the formation of brain-like^{40,41} and placode-like^{42,43} tissues generated from PSCs has been previously suggested. Although these pioneering approaches based on directed differentiation have paved the way for the derivation of region-specific brain- and placode-like structures, they have thus far ignored the *in vivo* complexity and interactions with various tissues present in the developing early embryo. Our approach addresses this bottleneck to form more developmentally relevant structures that harbor both brain- and PPE-like domains through an *in vivo* gastrulation-like process. Collectively, we believe that *EpiTS embryoids* bridge the gap between already existing hybrid embryoids and *gastruloids* and provide a modular and robust model system to perform mechanistic studies to identify unknown

embryonic or extraembryonic regulators of gastrulation and/or anterior development. Ultimately, the adoption of our approach to generate human embryoids holds significant potential to shed light on early human development as experimenting with early human embryos is challenging.

Materials and Methods

Cell culture

Mouse embryonic stem cells (SBr line⁴⁴) were cultured at 37°C in 5% CO₂ in medium composed of DMEM+Glutamax (#61965-026), 10% ES cell-qualified FBS (#16141-079), 1mM sodium pyruvate (#11360-070), 1x MEM non-essential aminoacids (#11140-035), 0.1mM 2-mercaptoethanol (#31350-010) and 1000u/ml Pen/Strep (#15140-122) supplemented with 3µM GSK3i (#361559), 2µM MEKi (#S1036) and 0.1µg/ml LIF (in house preparation). Cells were routinely passaged every 2-3 days by seeding 8000-9000 cells/cm² and every 20 passages a fresh vial was thawed. Cells were tested and confirmed free of mycoplasma. Mouse trophoblast stem cells (TS:GFP line⁴⁵) were cultured at 37°C in 5% CO₂ in TS medium composed of RPMI 1640+Glutamax (#61870-010), 20% ES cell-qualified FBS (#16141-079), 1mM sodium pyruvate (#11360-070), 0.1mM 2-mercaptoethanol (#31350-010) and 1000u/ml Pen/Strep (#15140-122). TS medium was conditioned on irradiated MEFs for 3 days and stored at -20°C. This was repeated three times for one batch of irradiated MEFs. Aliquots of TS conditioned medium (TSCM) were thawed and mixed 3:1 with fresh TS medium before cell passaging. 50ng/ml Fgf4 (#100-31) and 1µg/ml Heparin (#H3149) were added to make final TS medium. TS cells were routinely passaged every 2-3 days by seeding 5000-6000 cells/cm² and every 20 passages a fresh vial was thawed. Cells were tested and confirmed free of mycoplasma.

Gastruloid culture

Mouse ESCs were dissociated to single cells with Accutase (#A11105-01). Cells were then centrifuged at 1000 rpm for 5 minutes and washed twice with 10 ml PBS at room temperature. Cells were resuspended in N2B27 medium and counted on haemocytometer. 37,500 cells were added in 5ml of warm N2B27 to yield 300 cells per well. 40µl of the cell suspension was added to every well of one U-bottom low-attachment 96-well plate by multichannel pipettor. Plates were kept at 37°C in 5% CO₂ for 48 hours before further processing. At 48 hours, 3µM of CHIR99021 was prepared in warm N2B27 (e.g. 15µl of CHIR99021 at 3mM added in 15ml of N2B27) and added in 150µl to the plates. At 72, 96, 120 and 144 hours, 150µl of medium was replenished with fresh N2B27. To extend the culture period, gastruloids were transferred onto low-attachment 24-well plates in 700 µl fresh N2B27 at 120h and cultured in an incubator-compatible shaker for 48 h at 40 r.p.m. Four hundred microlitres medium was replenished at 144 h, and RNA was extracted from *gastruloids* at 168 h.

Preparing EPI and TS differentiation medium

N2B27 medium was prepared by 1:1 mixing of DMEM/F12+Glutamax (#31331-028) and Neurobasal (#21103-049) with the addition of 0.5x N2 supplement (#17502001), 0.5x B27 supplement (#17504001), 0.5x Glutamax (#35050-038), 1mM sodium pyruvate (#11360-070), 1x MEM non-essential amino acids (#11140-035), 0.1mM 2-mercaptoethanol (#31350-010) and 1000u/ml Pen/Strep (#15140-122). 12ng/ml Fgf2 (#PMG0035), 20ng/ml Activin-A (#338-AC) and 1% KSR (#10828-010) were added to make final EPI differentiation medium (EPIdiff). TS differentiation medium (TSdiff) was prepared by 1:1 mixing of N2B27 and TS medium supplemented with 25ng/ml Fgf4 (#100-31) and 500ng/ml Heparin (#H3149).

Preparing EPI and TSC Aggregates on PEG microwells

Poly(ethylene glycol) (PEG) microwells with 400µm well diameter (121 wells per array) were prepared on 24-well plates as previously described¹⁹. Microwells were equilibrated with 50µl of either EPIdiff (for ES cells) or TSdiff (for TS cells) for at least 30 minutes at 37°C. Mouse ES and TS cells were dissociated to single cells with Accutase (#A11105-01) or TrypLE (#12605-028), respectively. Cells were then centrifuged at 1000 rpm for 5 minutes and washed twice with 10 ml N2B27 medium at 4°C. Cells were resuspended in cold EPIdiff (for ES cells) or TSdiff (for TS cells) and suspension of 484,000 cells/ml was prepared. 35µl of the suspension was added dropwise on microwell arrays to have 100-150 cells/well. Seeding was done at 37°C for 15 minutes. Growth factor reduced Matrigel (#356231) was diluted in cold EPIdiff or TSdiff to 3% (v/v). The medium was vortexed and 1ml was slowly added from the side of the well, avoiding direct addition from the top of the microwell arrays. Plates were kept at 37°C in 5% CO₂ for at least 72 hours before further processing.

Forming EpiTS embryoids

At 72-75 hours of culture, aggregates on microwell arrays were flushed out and transferred to non-tissue culture treated 10cm plates in 10ml warm N2B27 medium. Single EPI and TSC aggregates were picked in 10µl and transferred to low adherent U-bottom 96 well plates (#COR-7007). 170µl of N2B27 medium was added on top. At 96 and 120 hours, 150µl of medium was replaced with fresh N2B27 and *EpiTS embryoids* were kept until 168h.

Immunostaining and confocal microscopy

EpiTS embryoids were washed with PBS and fixed with 4% PFA for 2 hours at 4°C. PFA was removed by three serial washes of 20 minutes at room temperature. Blocking was performed in blocking solution (PBS+10%FBS+0.3% Triton-X) for 1 hour at room temperature. Primary antibodies (see supplementary table 1) were incubated for at least 24 hours at 4°C in blocking solution. Next day, primary antibodies were removed by three serial washes of 20 minutes at room temperature. Secondary antibodies were incubated for 24 hours and next day embryoids were washed and mounted on glass slides in mounting medium. Confocal images were taken using an LSM700 inverted (Zeiss) with EC Plan-Neofluar 10x/0.30 or Plan-Apochromat 20x/0.80 air objectives.

Image analysis

All images were processed using algorithms developed in Image J (version 2.0.0-rc-69/1.52n). Brightfield, GFP (for TS cells), and mCherry (for *T/Bra*) channels were used as input. Thresholding and segmentation was performed sequentially for each channel. Area of EPI domain was calculated by subtraction of the area of the object identified in GFP channel from the area of the object identified in brightfield channel. For the calculation of the anterior EPI domain, area of the object identified in mCherry channel was subtracted from the EPI area. *T/Bra* coverage index was calculated by dividing area of the object identified in mCherry channel to the EPI area. For morphology measurements, bright-field images were thresholded and segmented. Maximum inscribed circle function was used to fit circles in the identified object. Axial length was determined by connecting centers of the fit circles. Elongation index was calculated by dividing axial length to the diameter of the maximum inscribed circle.

References

1. Doetschman, T. C., Eistetter, H., Katz, M., Schmidt, W. & Kemler, R. The in vitro development of blastocyst-derived embryonic stem cell lines: formation of visceral yolk sac, blood islands and myocardium. *J Embryol Exp Morphol* **87**, 27–45 (1985).
2. Brickman, J. M. & Serup, P. Properties of embryoid bodies. *Wiley Interdiscip Rev Dev Biol* **6**, e259 (2017).
3. Berge, ten, D. *et al.* Wnt signaling mediates self-organization and axis formation in embryoid bodies. *Cell Stem Cell* **3**, 508–518 (2008).
4. Warmflash, A., Sorre, B., Etoc, F., Siggia, E. D. & Brivanlou, A. H. A method to recapitulate early embryonic spatial patterning in human embryonic stem cells. *Nat. Methods* **11**, 847–854 (2014).
5. Morgani, S. M., Metzger, J. J., Nichols, J., Siggia, E. D. & Hadjantonakis, A.-K. Micropattern differentiation of mouse pluripotent stem cells recapitulates embryo regionalized cell fate patterning. *Elife* **7**, 1040 (2018).
6. van den Brink, S. C. *et al.* Symmetry breaking, germ layer specification and axial organisation in aggregates of mouse embryonic stem cells. *Development* **141**, 4231–4242 (2014).
7. Turner, D. A. *et al.* Anteroposterior polarity and elongation in the absence of extra-embryonic tissues and of spatially localised signalling in gastruloids: mammalian embryonic organoids. *Development* **144**, 3894–3906 (2017).
8. Girgin, M. *et al.* Generating Gastruloids from Mouse Embryonic Stem Cells. (2019). doi:10.17863/CAM.37946
9. Beccari, L. *et al.* Multi-axial self-organization properties of mouse embryonic stem cells into gastruloids. *Nature* **562**, 272–276 (2018).
10. Rivron, N. C. *et al.* Blastocyst-like structures generated solely from stem cells. *Nature* **557**, 106–111 (2018).
11. Vrij, E. J. *et al.* Chemically-defined induction of a primitive endoderm and epiblast-like niche supports post-implantation progression from blastoids. *bioRxiv* **120**, 510396 (2019).
12. Harrison, S. E., Sozen, B., Christodoulou, N., Kyprianou, C. & Zernicka-Goetz, M. Assembly of embryonic and extraembryonic stem cells to mimic embryogenesis in vitro. *Science* **356**, eaal1810 (2017).

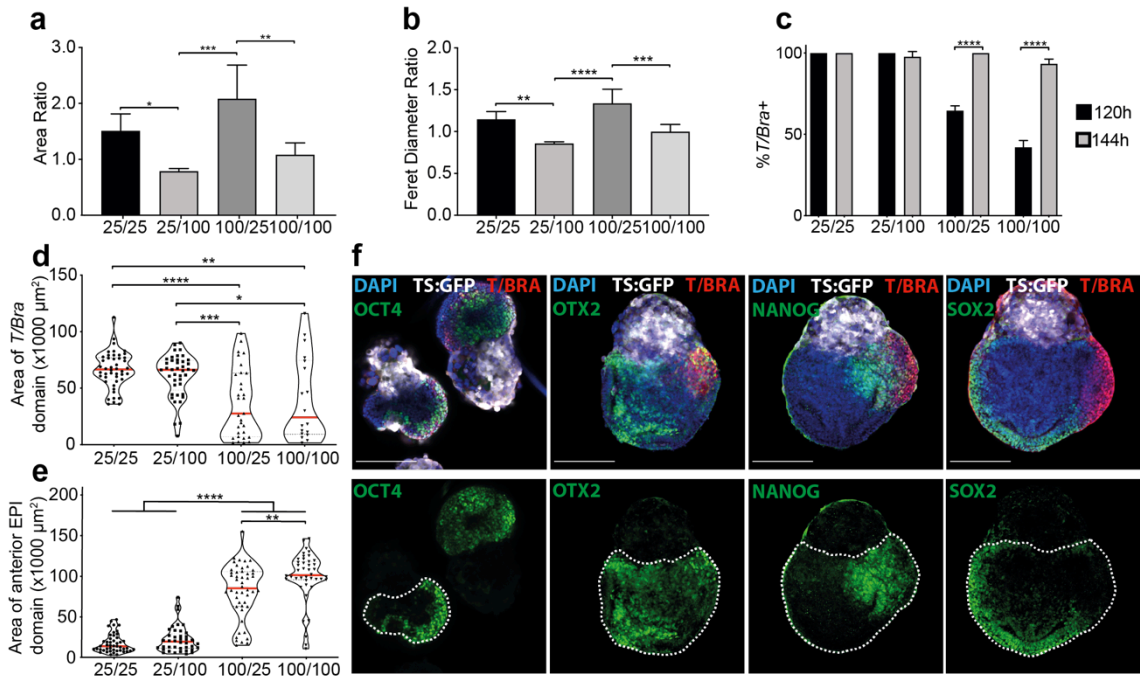
13. Sozen, B. *et al.* Self-assembly of embryonic and two extra-embryonic stem cell types into gastrulating embryo-like structures. *Nature Cell Biology* **20**, 979–989 (2018).
14. Zhang, S. *et al.* Implantation initiation of self-assembled embryo-like structures generated using three types of mouse blastocyst-derived stem cells. *Nature Communications* **10**, 1–17 (2019).
15. Meng, Y. *et al.* Pten facilitates epiblast epithelial polarization and proamniotic lumen formation in early mouse embryos. *Dev. Dyn.* **246**, 517–530 (2017).
16. Sheng, G. Epiblast morphogenesis before gastrulation. *Developmental Biology* **401**, 17–24 (2015).
17. Cajal, M. *et al.* Clonal and molecular analysis of the prospective anterior neural boundary in the mouse embryo. *Development* **139**, 423–436 (2012).
18. Donnison, M. *et al.* Loss of the extraembryonic ectoderm in Elf5 mutants leads to defects in embryonic patterning. *Development* **132**, 2299–2308 (2005).
19. Unzu, C. *et al.* Pharmacological Induction of a Progenitor State for the Efficient Expansion of Primary Human Hepatocytes. *Hepatology* **69**, 2214–2231 (2019).
20. Eiraku, M. *et al.* Self-organizing optic-cup morphogenesis in three-dimensional culture. *Nature* **472**, 51–56 (2011).
21. Hamidi, S. *et al.* Mesenchymal-Epithelial Transition Regulates Initiation of Pluripotency Exit before Gastrulation. *bioRxiv* **28**, 655654 (2019).
22. Bedzhov, I. & Zernicka-Goetz, M. Self-Organizing Properties of Mouse Pluripotent Cells Initiate Morphogenesis upon Implantation. *Cell* **156**, 1032–1044 (2014).
23. Latos, P. A. & Hemberger, M. From the stem of the placental tree: trophoblast stem cells and their progeny. *Development* **143**, 3650–3660 (2016).
24. Carver, E. A., Jiang, R., Lan, Y., Oram, K. F. & Gridley, T. The mouse snail gene encodes a key regulator of the epithelial-mesenchymal transition. *Mol. Cell. Biol.* **21**, 8184–8188 (2001).
25. Rossant, J. & Tam, P. P. L. Blastocyst lineage formation, early embryonic asymmetries and axis patterning in the mouse. *Development* **136**, 701–713 (2009).
26. Arnold, S. J. & Robertson, E. J. Making a commitment: cell lineage allocation and axis patterning in the early mouse embryo. *Nat Rev Mol Cell Biol* **10**, 91–103 (2009).
27. Fausett, S. R., Brunet, L. J. & Klingensmith, J. BMP antagonism by Noggin is required in presumptive notochord cells for mammalian foregut morphogenesis. *Developmental Biology* **391**, 111–124 (2014).

28. Mukhopadhyay, M. *et al.* Dickkopf1 is required for embryonic head induction and limb morphogenesis in the mouse. *Developmental Cell* **1**, 423–434 (2001).
29. Lewis, S. L. *et al.* Dkk1 and Wnt3 interact to control head morphogenesis in the mouse. *Development* **135**, 1791–1801 (2008).
30. Martinez-Barbera, J. P. *et al.* Regionalisation of anterior neuroectoderm and its competence in responding to forebrain and midbrain inducing activities depend on mutual antagonism between OTX2 and GBX2. *Development* **128**, 4789–4800 (2001).
31. Aubert, J. *et al.* Screening for mammalian neural genes via fluorescence-activated cell sorter purification of neural precursors from Sox1-gfp knock-in mice. *Proceedings of the National Academy of Sciences* **100 Suppl 1**, 11836–11841 (2003).
32. Wood, H. B. & Episkopou, V. Comparative expression of the mouse Sox1, Sox2 and Sox3 genes from pre-gastrulation to early somite stages. *Mech. Dev.* **86**, 197–201 (1999).
33. Sato, S. *et al.* Conserved expression of mouse Six1 in the pre-placodal region (PPR) and identification of an enhancer for the rostral PPR. *Developmental Biology* **344**, 158–171 (2010).
34. Britton, G., Heemskerk, I., Hodge, R., Qutub, A. A. & Warmflash, A. A novel self-organizing embryonic stem cell system reveals signaling logic underlying the patterning of human ectoderm. *bioRxiv* 518803 (2019). doi:10.1101/518803
35. Haremak, T. *et al.* Self-organizing neuruloids model developmental aspects of Huntington's disease in the ectodermal compartment. *Nature Biotechnology* **2**, 479–11 (2019).
36. Martinez-Morales, J. R., Signore, M., Acampora, D., Simeone, A. & Bovolenta, P. Otx genes are required for tissue specification in the developing eye. *Development* **128**, 2019–2030 (2001).
37. Nelson, W. J. & Nusse, R. Convergence of Wnt, β -Catenin, and Cadherin Pathways. *Science* **303**, 1483–1487 (2004).
38. Martyn, I., Brivanlou, A. H. & Siggia, E. D. A wave of WNT signaling balanced by secreted inhibitors controls primitive streak formation in micropattern colonies of human embryonic stem cells. *Development* **146**, dev172791 (2019).
39. Hayashi, K., Ohta, H., Kurimoto, K., Aramaki, S. & Saitou, M. Reconstitution of the mouse germ cell specification pathway in culture by pluripotent stem cells. *Cell* **146**, 519–532 (2011).
40. Lancaster, M. A. *et al.* Cerebral organoids model human brain development and microcephaly. *Nature* **501**, 373–379 (2013).

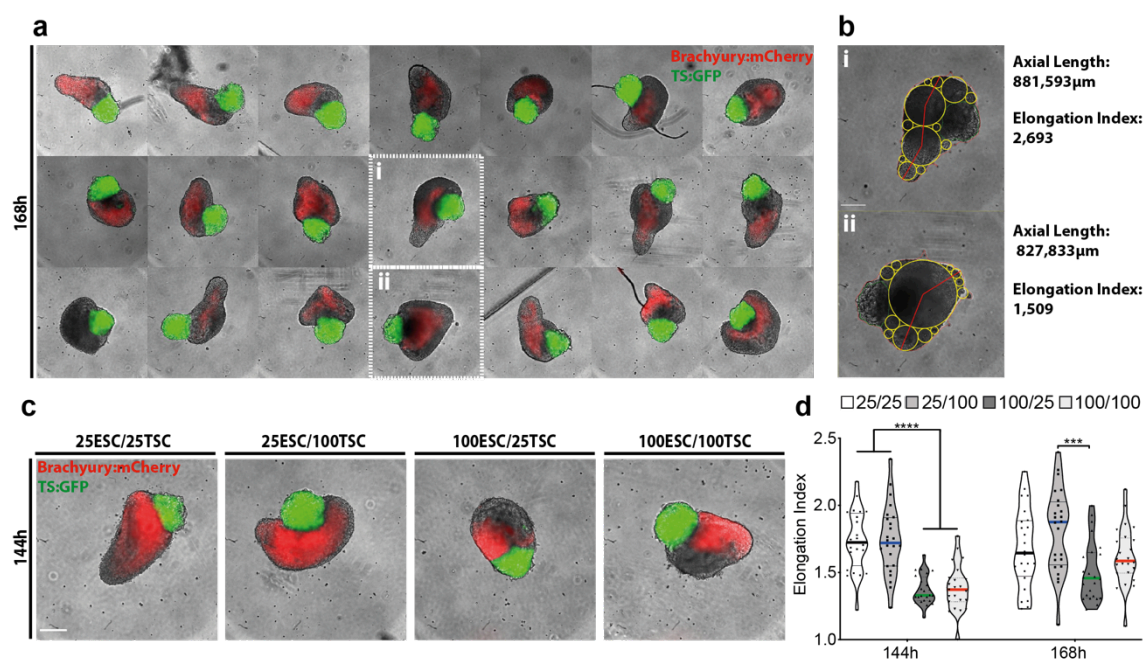
41. Qian, X. *et al.* Brain-Region-Specific Organoids Using Mini-bioreactors for Modeling ZIKV Exposure. *Cell* **165**, 1238–1254 (2016).
42. Koehler, K. R. *et al.* Generation of inner ear organoids containing functional hair cells from human pluripotent stem cells. *Nature Biotechnology* **35**, 583–589 (2017).
43. Nakano, T. *et al.* Self-formation of optic cups and storable stratified neural retina from human ESCs. *Cell Stem Cell* **10**, 771–785 (2012).
44. Deluz, C. *et al.* A role for mitotic bookmarking of SOX2 in pluripotency and differentiation. *Genes & Development* **30**, 2538–2550 (2016).
45. Tanaka, S., Kunath, T., Hadjantonakis, A. K., Nagy, A. & Rossant, J. Promotion of trophoblast stem cell proliferation by FGF4. *Science* **282**, 2072–2075 (1998).

SUPPORTING INFORMATION FOR CHAPTER IV:

BIOENGINEERED EMBRYOIDS MIMIC POST-IMPLANTATION
DEVELOPMENT IN VITRO

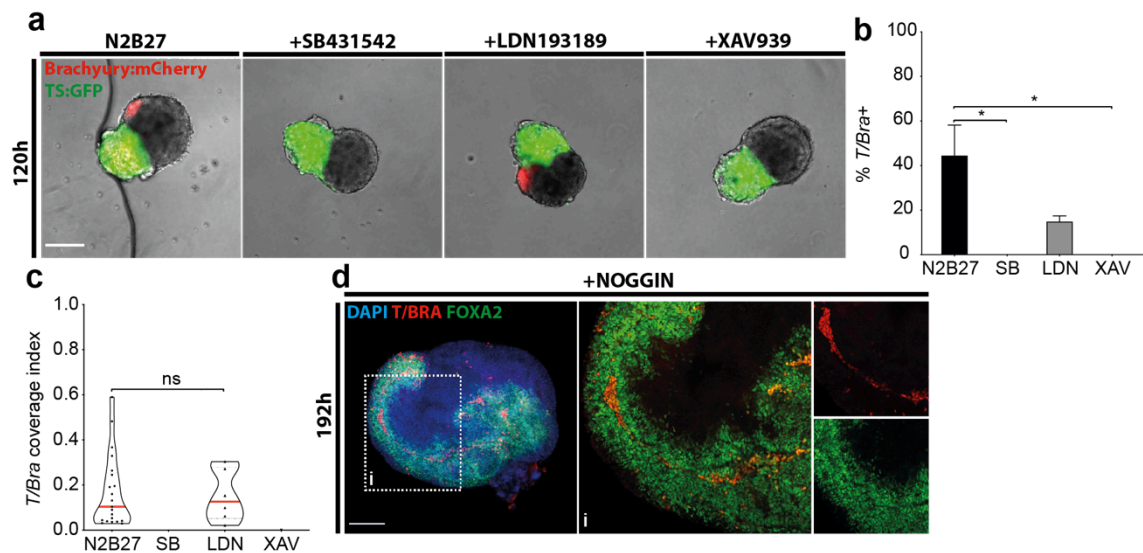


Supplementary Figure 1: Morphological measurements of EPI and TSC aggregates and *T/Bra* expression dynamics in *EpiTS* embryoids. **a-e)** Morphological measurements and *T/Bra* expression dynamics in *EpiTS* embryoids formed from different starting cell numbers per well (ESC/TSC). **a)** Area ratios of EPI and TSC aggregates. Data are shown as mean with standard deviation. Data is collected from five biologically independent experiments. **b)** Feret diameter ratios of EPI and TSC aggregates. Data are shown as mean with standard deviation. Data is collected from five biologically independent experiments. **c)** Percentage of *T/Bra*-positive *EpiTS* embryoids at 120 and 144 h of culture. Data are shown as mean with standard deviation. Data is collected from two biologically independent experiments. **d)** Area of *T/Bra* expression domain at 120h. Data are shown as median. For 25/25, 25/100, 100/25 and 100/100 conditions, total number of embryoids analyzed were 46, 41, 31 and 18, respectively. Data was collected from two biologically independent experiments. **e)** Area of anterior EPI domain calculated by subtraction of *T/Bra*-positive area from total EPI area. Data are shown as median. For 25/25, 25/100, 100/25 and 100/100 conditions, total number of embryoids analyzed were 46, 4, 48 and 42, respectively. Data was collected from two biologically independent experiments. **f)** Representative confocal images at 120 hours. Nuclei were stained with DAPI. GFP-labeled TS cells were depicted in gray. *T/Bra* expression marks the gastrulation-like events and colocalizes with *Oct4* and *Nanog*. *Otx2* and *Sox2* expression are mostly detected on the anterior domain. For statistical analysis one-way (**a,b,d,e**) or two-way (**c**) ANOVA followed by Bonferroni multiple comparison test were performed. Following P-value style was used: ns=not significant, P****<0.0001, P***<0.0002, P**<0.0021, P*<0.0332.

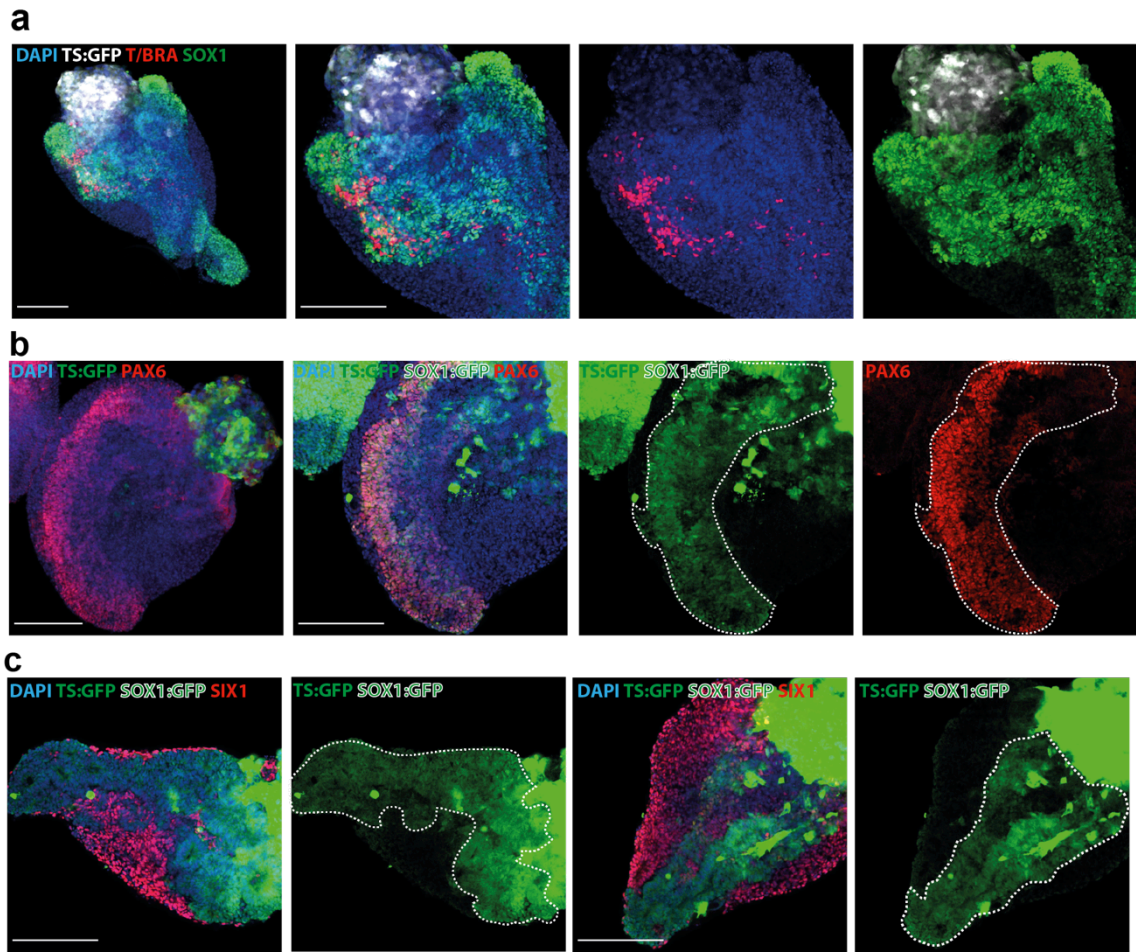


Supplementary Figure 2: Role of epithelial architecture of EPI aggregates in axial morphogenesis.

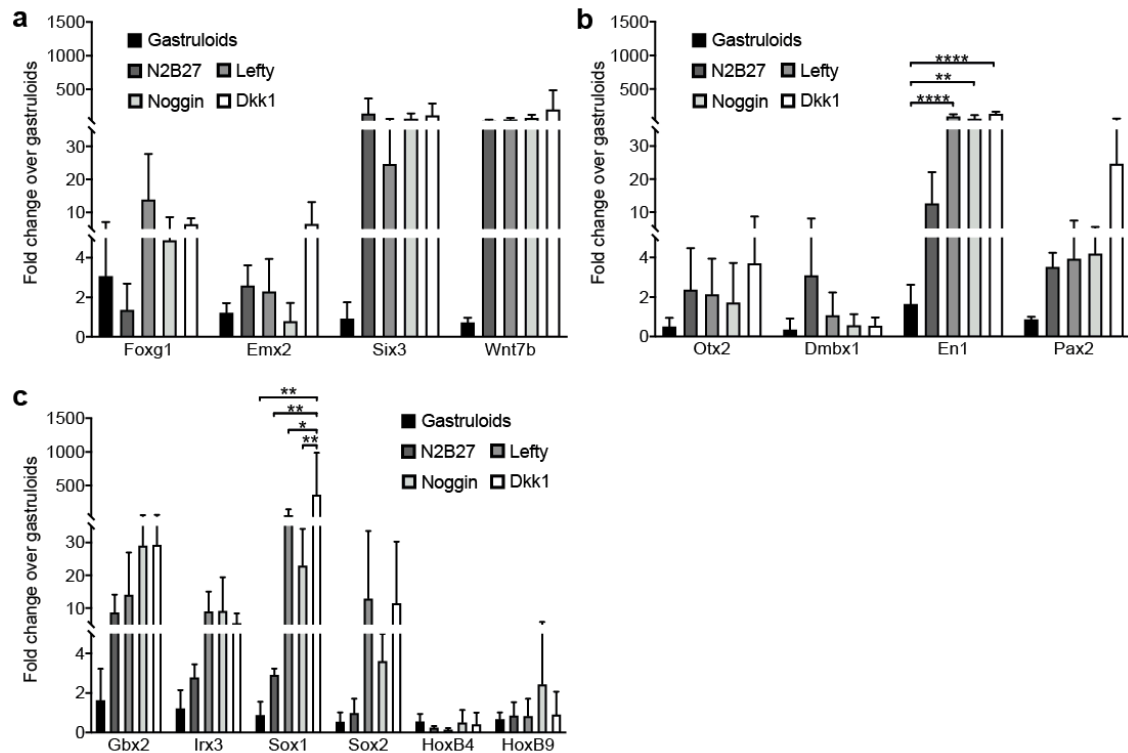
a) Montage of EpiTS embryoids showing reproducible axial elongation at 168 h. **b)** Representative images describing axial length and elongation index measurement criteria. **c,d)** Characterization of *EpiTS* embryoids formed from 25ESC/25TSC, 25ESC/100TSC, 100ESC/25TSC and 100ESC/100TSC conditions at late stages. **c)** Representative images at 144. **d)** Comparison of elongation index between 144 h and 168 h. Data are shown as median. For 25/25, 25/100, 100/25 and 100/100, total number of embryoids analyzed were 24, 24, 24, 23, respectively at 144h and 24, 24, 24, 24, respectively at 168h. For statistical analysis, two-way ANOVA followed by Bonferroni multiple comparison test were performed. Following P-value style was used: ns=not significant, P****<0.0001, P***<0.0002, P**<0.0021, P*<0.0332. Scale bars: 200μm.



Supplementary Figure 3: The effect of small molecule inhibitors of TGF- β , BMP and Wnt signaling pathways on *T/Bra* expression dynamics. a-c) *T/Bra* expression dynamics in *EpiTS* embryoids treated with indicated inhibitors between 96 h and 120 h. **a) Representative images at 120 h. **b)** Percentage of *T/Bra*-positive *EpiTS* embryoids at 120 h. Data are shown as mean with standard deviation. Data is collected from two biologically independent experiments. **c)** *T/Bra* coverage index calculated by division of *T/Bra*-positive area to total EPI area at 120 h. Data are shown as median. Data was collected from two biologically independent experiments. For N2B27 and LDN conditions, total number of embryoids analyzed were 21 and 7, respectively. There were no *T/Bra*+ embryoids in SB and XAV conditions. **d)** Representative confocal images of Noggin-treated (96h-120h) *EpiTS* embryoid showing colocalization of *T/Bra* and *Foxa2* expression at 192 h. For statistical analysis, one-way ANOVA followed by Bonferroni multiple comparison test (**b**) or two-tailed unpaired Student's t-test (**c**) were performed. Following P-value style was used: ns=not significant, P****<0.0001, P***<0.0002, P**<0.0021, P*<0.0332. Scale bar: 200 μ m.**



Supplementary Figure 4: Expression profile of anterior neural markers in late stage *EpiTS* embryoids. **a)** Confocal images showing *T/Bra* and *Sox1* expression at high magnification at 168 h. Nuclei were stained with DAPI. GFP-labeled TS cells were depicted in gray. **b)** Confocal images showing *Pax6* and *Sox1* expression at 168 h. Nuclei were stained with DAPI. GFP-labeled TS cells were depicted in green. Samples were overexposed to visualize endogenous *Sox1:GFP* expression (dashed lines). **c)** Confocal images showing *Six1* and *Sox1* expression at 168 h. Nuclei were stained with DAPI. GFP-labeled TS cells were depicted in green. Samples were overexposed to visualize endogenous *Sox1:GFP* expression (dashed lines). Scale bars: 200µm.



Supplementary Figure 5: The effect of protein inhibitors of TGF- β , BMP and Wnt signaling pathways on expression of neural genes. a-c) RT-PCR analysis showing expression levels of forebrain (a), midbrain (b) and hindbrain/ central nervous system/spinal cord (c) genes in 168 h *EpiTS* embryoids treated with indicated inhibitors between 96 h and 120 h. Data are shown as mean with standard deviation and normalized to age-matched gastruloids. Data are shown as mean with standard deviation. Data is collected from three biologically independent experiments. For statistical analysis, two-way ANOVA followed by Bonferroni multiple comparison test were performed. Following P-value style was used: ns=not significant, P**<0.0001, P***<0.0002, P**<0.0021, P*<0.0332. Scale bars: 200 μ m.**

CHAPTER V

CONCLUSIONS AND OUTLOOK

In 1828, Karl Ernst von Baer discovered the blastula and proposed the basic guidelines of embryonic development: a trajectory from a homogeneous, simple tissue towards more heterogeneous and complex structures¹. Since then, the embryo continued to develop the same way, but our knowledge about it tremendously increased over the years. Numerous studies have been done with various types of model organisms to understand how tissues and organs form in such a well-orchestrated manner. I believe, in the last few decades, developmental biology is switching gears to take a different perspective about understanding embryonic development. As inspired by Richard Feynman's words² and Baer's trajectory; we are now aiming to create simpler structures in order to better understand the complex embryonic development. In this PhD thesis, I followed this trajectory, with a goal to create simplified versions to better understand post-implantation mouse embryonic development.

After 120 years since Baer's first observations, scientists finally achieved culturing mammalian embryos *ex utero*^{3,4} and showed that they can give rise to viable progeny when implanted back in mouse uteri⁵. These findings led scientists to come to the realization that embryonic development could take place, in some part, outside of the animal body. However, the idea of being able to create embryo-like structures followed later when experiments with teratocarcinomas^{6,7} introduced the concept of multipotency; i.e., a cell of origin (embryonal carcinoma (EC) cell) that has potential to create all other cells types⁸. When aggregates of these tumor-forming cells were formed, they were organized in a way that is similar to the developing embryo; a visceral endoderm surrounding undifferentiated cells. Therefore, these aggregates were called embryoid bodies (EBs)^{9,10}.

The culture conditions used to propagate EC cells led to the isolation and maintenance of mouse embryonic stem cells (mESCs) in 1981^{11,12}. EBs formed with mESCs were shown to demonstrate cell fate patterning similar to that of mouse embryos, eventually forming cell types from ectoderm, mesoderm and endoderm germ layers¹³⁻¹⁸, albeit in an uncontrolled way. Even though these pioneering approaches were extremely reductionist, they have revealed the self-organization potential of pluripotent stem cells, a phenomenon that paved the way for the establishment of more advanced embryo-like structures.

During my PhD, I have established and characterized three different approaches to build up on existing *in vitro* models of embryonic development. In the first part, I focused on a more advanced version of mESC-derived embryoid bodies, *gastruloids*^{19,20}, that upon stimulation of Wnt signaling, exhibited recapitulation of certain developmental features such as symmetry breaking and axial elongation. I showed that when *gastruloids* were cultured for an extended period²¹, they could establish patterning along antero-posterior, dorso-ventral and medio-lateral

axes. I further demonstrated that *gastruloids* could demonstrate spatial and temporal activation of Hox genes, in a way strikingly similar to the mouse embryo²².

Despite demonstrating elaborate patterning on the posterior domain (i.e. tail), *gastruloids* failed to form any anterior neural structures (i.e. brain). I hypothesized that the early stages of the current *gastruloid* protocol is not permissive for the formation and maintenance of anterior neural progenitors. Therefore, in the second part of my thesis, I established a novel aggregation platform from mESCs to achieve an epiblast-like structure that would comprise both anterior and posterior progenitors. To do so, I have modified the culture medium by removing the Wnt agonist CHIR99021 that was the obvious candidate for the uniform induction of mesodermal differentiation in the expense of anterior neural differentiation. Instead, I supplemented the serum-free medium with Activin-A, Fgf2 and Knockout Serum Replacement to induce an epiblast identity²³ in aggregating mESCs. When individually transferred to serum-free medium in the absence of the above-mentioned factors, these epiblast-like (EPI) aggregates broke symmetry, initiated *T/Bra* expression and underwent axial elongation to yield to structures that were similar to *gastruloids*. I could identify the initial EPI aggregate size as an important determinant for the extent of axial elongation. Interestingly, when Wnt inhibitor XAV939 was added in the medium during the aggregation period, the resulting structures had a fundamental difference; the *T/Bra*-negative anterior domain was populated by neural progenitors. This observation was along the lines with studies performed in mouse embryos that suggested a Wnt-deprived environment for the formation of anterior neural progenitors^{24,25}. Moreover, in our bioengineered aggregation platform, we could form EPI aggregates with an epithelium by using diluted Matrigel as substitute for epiblast basement membrane^{26,27}. Epithelialized EPI aggregates also demonstrated dependence to the initial aggregate diameter for the axial elongation and recapitulated the formation of anterior neural progenitors, providing an alternative way to generate these cells. In the future, detailed analysis by RNA sequencing at specific time-points during the development of EPI aggregates (with or without early Wnt inhibition/epithelialization) will be informative to identify how and when these progenitors arise and what types of tissues do they form. It would also be interesting to see whether mesoderm or endoderm derived tissues are present in late EPI aggregates.

In the third chapter of my thesis, I presented a hybrid *embryoid* model that comprises both embryonic and extraembryonic compartments. Inspired from the pioneering work that showed remarkable self-organization capacity of mouse embryonic and trophoblast stem cells^{26,28}, I decided to build on previously established epithelialized EPI aggregates by adding an extraembryonic domain derived from trophoblast stem cells (TSCs). This new method allowed

independent modulation of biochemical (e.g. medium components) and biophysical (e.g. size, epithelialization) properties of the embryonic and extraembryonic compartments. In order to maximize the efficiency of coupling of the two domains, I decided to pre-form EPI and TSC aggregates in high-throughput and then individually place them in low attachment U-bottom wells. When formed at optimal sizes, 75-80% of these hybrid embryoids initiated gastrulation-like events (e.g. *T/Bra* expression) at the embryonic-extraembryonic interface, an efficiency that was higher than previous reports^{26,29,30}. Moreover, for the first time, I could demonstrate that hybrid embryoids could undergo axial elongation and demonstrate patterning that resembles formation of primitive brain-like and preplacodal ectoderm-like regions. I believe these observations and results bridge the gap between *gastruloids* and hybrid embryoid models, to demonstrate that gastrulation and post-gastrulation stages could be mimicked *in vitro*.

In the future, it will be interesting to conduct a comparative study between EPI aggregates and *EpiTS embryoids*, to elucidate the role of extraembryonic tissues in initiating gastrulation-like events or to define an unprecedented role of extraembryonic tissues in the formation of anterior neural tissues. Single cell-sequencing at different stages of the *EpiTS embryoid* culture would allow identification of cell types that emerge in both systems and help us to explore generation of rare cells such as hematopoietic stem cells and primordial germ cells, that are not convenient to generate with *in vitro* directed differentiation approaches. Moreover, extending the culture period of *EpiTS embryoids* beyond one week would be interesting to potentially see development of more complex brain-like structures. Direct comparison of extended *EpiTS embryoids* to cerebral organoids³¹ might reveal differences between two different approaches to generate organ-like structures: former following a developmentally relevant trajectory and latter following a directed differentiation approach. Similarly, careful characterization of Hox gene activation in extended *EpiTS embryoids* and comparison to *gastruloids* would allow better understanding of the extent of antero-posterior patterning in hybrid embryoids.

Furthermore, advanced bioengineering approaches, such as incorporation of hybrid embryoids in bioinspired hydrogels³², remains as an uncharted area. Uterus-mimicking biomaterials will potentially have a beneficiary effect on the long-term culture of these hybrid embryoids. This would also allow studying the influence of extracellular and mechanical forces on embryogenesis, a phenomenon that is difficult to address in post-implantation mouse embryos. Ultimately, the application of the methodologies described here by using human embryonic and extraembryonic stem cells will carry an immense potential. Considering the limited access to the human embryos due to ethical and technical challenges, hybrid human embryoids could be used to perform embryotoxicity experiments to screen for compounds that have detrimental

effects on early embryonic development³³. Moreover, induced pluripotent stem cells (iPSCs) could be used to model diseases that demonstrate an embryonic onset around gastrulation or axial extension³⁴. Such experiments would contribute to the better understanding of the disease etiology.

Ever since we realized that embryonic development could be recapitulated *in vitro*, we are constantly learning how to solve problems that have been solved by the embryo over the millions of years. I believe, this PhD thesis contributes to our collective advancements^{22,26,28-30,35-41} towards solving these problems and creating simplified embryo-like structures, in order to understand embryonic development better. I strongly believe that the future holds great promise for the advancement and application of these newly emerging methodologies.

References

1. Tammiksaar, E. & Brauckmann, S. *Karl ernst von Baer's "Über Entwicklungsgeschichte der Thiere II" and its unpublished drawings. History and philosophy of the life sciences* **26**, 291–308 (2004).
2. Way, M. "What I cannot create, I do not understand". *Journal of Cell Science* **130**, 2941–2942 (2017).
3. Hammond, J. Recovery and Culture of Tubal Mouse Ova. *Nature* **163**, 28–29 (1949).
4. Whitten, W. K. Culture of Tubal Mouse Ova. *Nature* **177**, 96– (1956).
5. McLaren, A. & Biggers, J. D. Successful Development and Birth of Mice cultivated in vitro as Early Embryos. *Nature* **182**, 877–878 (1958).
6. PIERCE, G. B. & DIXON, F. J. Testicular teratomas. II. Teratocarcinoma as an ascitic tumor. *Cancer* **12**, 584–589 (1959).
7. STEVENS, L. C. Embryology of testicular teratomas in strain 129 mice. *J. Natl. Cancer Inst.* **23**, 1249–1295 (1959).
8. KLEINSMITH, L. J. & PIERCE, G. B. MULTIPOTENTIALITY OF SINGLE EMBRYONAL CARCINOMA CELLS. *Cancer Res.* **24**, 1544–1551 (1964).
9. Martin, G. R. & Evans, M. J. Differentiation of clonal lines of teratocarcinoma cells: formation of embryoid bodies in vitro. *Proceedings of the National Academy of Sciences* **72**, 1441–1445 (1975).
10. Martin, G. R. & Evans, M. J. Multiple differentiation of clonal teratocarcinoma stem cells following embryoid body formation in vitro. *Cell* **6**, 467–474 (1975).
11. Evans, M. J. & Kaufman, M. H. Establishment in culture of pluripotential cells from mouse embryos. *Nature* **292**, 154–156 (1981).
12. Martin, G. R. Isolation of a pluripotent cell line from early mouse embryos cultured in medium conditioned by teratocarcinoma stem cells. *Proceedings of the National Academy of Sciences* **78**, 7634–7638 (1981).
13. Guan, K., Chang, H., Rolletschek, A. & Wobus, A. M. Embryonic stem cell-derived neurogenesis. Retinoic acid induction and lineage selection of neuronal cells. *Cell Tissue Res.* **305**, 171–176 (2001).
14. Kubo, A. *et al.* Development of definitive endoderm from embryonic stem cells in culture. *Development* **131**, 1651–1662 (2004).

15. Bone, H. K., Nelson, A. S., Goldring, C. E., Tosh, D. & Welham, M. J. A novel chemically directed route for the generation of definitive endoderm from human embryonic stem cells based on inhibition of GSK-3. *Journal of Cell Science* **124**, 1992–2000 (2011).
16. Doetschman, T. C., Eistetter, H., Katz, M., Schmidt, W. & Kemler, R. The in vitro development of blastocyst-derived embryonic stem cell lines: formation of visceral yolk sac, blood islands and myocardium. *J Embryol Exp Morphol* **87**, 27–45 (1985).
17. Berge, ten, D. *et al.* Wnt Signaling Mediates Self-Organization and Axis Formation in Embryoid Bodies. *Stem Cell* **3**, 508–518 (2008).
18. Itskovitz-Eldor, J. *et al.* Differentiation of Human Embryonic Stem Cells into Embryoid Bodies Comprising the Three Embryonic Germ Layers. *Mol Med* **6**, 88–95 (2000).
19. van den Brink, S. C. *et al.* Symmetry breaking, germ layer specification and axial organisation in aggregates of mouse embryonic stem cells. *Development* **141**, 4231–4242 (2014).
20. Turner, D. A. *et al.* Anteroposterior polarity and elongation in the absence of extra-embryonic tissues and of spatially localised signalling in gastruloids: mammalian embryonic organoids. *Development* **144**, 3894–3906 (2017).
21. Girgin, M. *et al.* Generating Gastruloids from Mouse Embryonic Stem Cells. (2019). doi:10.17863/CAM.37946
22. Beccari, L. *et al.* Multi-axial self-organization properties of mouse embryonic stem cells into gastruloids. *Nature* **562**, 272–276 (2018).
23. Hayashi, K., Ohta, H., Kurimoto, K., Aramaki, S. & Saitou, M. Reconstitution of the mouse germ cell specification pathway in culture by pluripotent stem cells. *Cell* **146**, 519–532 (2011).
24. Arnold, S. J. & Robertson, E. J. Making a commitment: cell lineage allocation and axis patterning in the early mouse embryo. *Nat Rev Mol Cell Biol* **10**, 91–103 (2009).
25. Kimura, C. *et al.* Visceral endoderm mediates forebrain development by suppressing posteriorizing signals. *Developmental Biology* **225**, 304–321 (2000).
26. Harrison, S. E., Sozen, B., Christodoulou, N., Kyprianou, C. & Zernicka-Goetz, M. Assembly of embryonic and extraembryonic stem cells to mimic embryogenesis in vitro. *Science* **356**, eaal1810 (2017).

27. Bedzhov, I. & Zernicka-Goetz, M. Self-Organizing Properties of Mouse Pluripotent Cells Initiate Morphogenesis upon Implantation. *Cell* **156**, 1032–1044 (2014).
28. Rivron, N. C. *et al.* Blastocyst-like structures generated solely from stem cells. *Nature* **557**, 106–111 (2018).
29. Sozen, B. *et al.* Self-assembly of embryonic and two extra-embryonic stem cell types into gastrulating embryo-like structures. *Nature Cell Biology* **20**, 979–989 (2018).
30. Zhang, S. *et al.* Implantation initiation of self-assembled embryo-like structures generated using three types of mouse blastocyst-derived stem cells. *Nature Communications* **10**, 1–17 (2019).
31. Lancaster, M. A. *et al.* Cerebral organoids model human brain development and microcephaly. *Nature* **501**, 373–379 (2013).
32. Blondel, D. & Lutolf, M. P. Bioinspired Hydrogels for 3D Organoid Culture. *Chimia (Aarau)* **73**, 81–85 (2019).
33. Liu, H. *et al.* Embryotoxicity estimation of commonly used compounds with embryonic stem cell test. *Mol Med Rep* **16**, 263–271 (2017).
34. Vaquer, A. F. & Hadjantonakis, A.-K. Birth defects associated with perturbations in preimplantation, gastrulation, and axis extension: from conjoined twinning to caudal dysgenesis. *Wiley Interdiscip Rev Dev Biol* **2**, 427–442 (2013).
35. Morgani, S. M., Metzger, J. J., Nichols, J., Siggia, E. D. & Hadjantonakis, A.-K. Micropattern differentiation of mouse pluripotent stem cells recapitulates embryo regionalized cell fate patterning. *Elife* **7**, 1040 (2018).
36. Warmflash, A., Sorre, B., Etoc, F., Siggia, E. D. & Brivanlou, A. H. A method to recapitulate early embryonic spatial patterning in human embryonic stem cells. *Nat. Methods* **11**, 847–854 (2014).
37. Shao, Y. *et al.* Self-organized amniogenesis by human pluripotent stem cells in a biomimetic implantation-like niche. *Nature Materials* **16**, 419–425 (2017).
38. Zheng, Y. *et al.* Controlled modelling of human epiblast and amnion development using stem cells. *Nature* **573**, 421–425 (2019).
39. Manfrin, A. *et al.* Engineered signaling centers for the spatially controlled patterning of human pluripotent stem cells. *Nat. Methods* **16**, 640–648 (2019).
40. Vrij, E. J. *et al.* Chemically-defined induction of a primitive endoderm and epiblast-like niche supports post-implantation progression from blastoids. *bioRxiv* **120**, 510396 (2019).

41. Simunovic, M. *et al.* A 3D model of a human epiblast reveals BMP4-driven symmetry breaking. *Nature Cell Biology* **21**, 900–910 (2019).

CHAPTER VI

CURRICULUM VITAE

Curriculum Vitae

Mehmet Uğur Girgin

Current address: Chemin des Retraites 11, 1004, Lausanne, Switzerland

Phone number: +41 78 859 35 24

Email address: mehmet.girgin@epfl.ch

Nationality: Turkish

EDUCATION

École Polytechnique Fédérale de Lausanne, EPFL, SWITZERLAND 2014-2019

PhD in Biotechnology and Bioengineering Program (EDBB)

Koç University, College of Sciences, Istanbul, TURKEY 2010-2014

BSc in Molecular Biology and Genetics

Işıkent High School, Izmir, TURKEY 2006-2010

RESEARCH EXPERIENCE

Laboratory of Prof. Dr. Matthias Lutolf, EPFL, Lausanne 2014-2019

PhD Project: "In vitro modeling of early mouse development".

Laboratory of Dr. Tamer Onder, Koc University, Istanbul 2014

Undergraduate Research Project: "CRISPR/Cas9 mediated knockout of human Ash1L and testing its effect on reprogramming".

Laboratory of Dr. Mazhar Adli, University of Virginia, USA 2013

Summer Internship Research Project: "Role of CHD7 chromatin remodeler on differentiation of hematopoietic stem cells into myeloid lineage".

Laboratory of Dr. Tamer Onder, Koc University, Istanbul 2012-2014

Undergraduate Research Project: "Role of H3K36 methyltransferases in somatic cell reprogramming and induced pluripotent stem cell generation".

PUBLICATIONS

*Girgin M. U., Hoehnel S., Brandenberg N., Arias A. M., Lutolf M.P. Bioengineered embryoids mimic post-implantation development in vitro. **Nature Cell Biology**. Manuscript submitted, received on September, 2019.

Rossi G., Boni A., Guet R., Girgin M. U., Kelly R., Lutolf M. P. Embryonic organoids recapitulate early heart organogenesis. **Cell Stem Cell**. Manuscript submitted, received on November, 2019.

Kolb L., Allazetta S., Karlsson M., Girgin M.U., Weber W., Lutolf M.P. High-throughput stem cell-based phenotypic screening through microniches. **Biomater Sci**. 2019 Jul 23;7(8):3471-3479. doi: 10.1039/c8bm01180j.

*Beccari L., *Moris N., *Girgin M. U., Turner D.A., Baillie-Johnson P., Cossy A.C., Lutolf M.P., Duboule D., Arias A. M. Multi-axial self-organization properties of mouse embryonic stem cells into gastruloids. **Nature**. 2018 Oct;562(7726):272-276. doi: 10.1038/s41586-018-0578-0. Epub 2018 Oct 3.

Turner D. A., Girgin M. U., Alonso-Crisostomo L., Trivedi V., Baillie-Johnson P., Glodowski C. R., Hayward P.C., Collignon J., Gustavsen C., Serup P., Steventon B., Lutolf M. P., Arias AM. Anteroposterior polarity and elongation in the absence of extra-embryonic tissues and of spatially localised signalling in gastruloids: mammalian embryonic organoids. **Development**. 2017 Nov 1;144(21):3894-3906. doi: 10.1242/dev.150391. Epub 2017 Sep 26.

Ranga A., Girgin M. U., Meinhardt A., Eberle D., Caiazzo M., Tanaka E. M., Lutolf M. P. Neural tube morphogenesis in synthetic 3D microenvironments. **Proc Natl Acad Sci U S A**. 2016 Nov 1;113(44):E6831-E6839. Epub 2016 Oct 14.

Acknowledgements

I would like to express my gratitude to Professor Matthias Lutolf for giving me the opportunity to be a part of his laboratory as a PhD student and his continuous support during these five years. With his guidance, I have improved a lot as a scientist. I always saw myself as a lucky one to be surrounded by amazing scientists in a fun and collaborative environment. I would also like to thank Matthias for creating this environment.

My sincere thanks go to Professor Alfonso Martinez-Arias whom I collaborated with very closely and who led me to take smart decisions regarding my PhD career. I learnt a lot from our scientific/non-scientific discussions. Thanks also to David, Naomi and Peter from Alfonso's lab for long-lasting collaboration.

I would like to thank Professor Denis Duboule and Leonardo for sharing their expertise with us and helping me to publish my first first—author paper. It has been a great experience.

A big thanks goes to the members of my PhD thesis jury: Bart Deplancke, Andrew Oates, Ben Steventon and Nicolas Rivron for agreeing to be a part of my PhD defense and their constructive comments during the exam. I feel very honored to be nominated as a candidate for the best thesis award.

Thanks to Romain Guet and Olivier Burri from Bioimaging and Optics Platform (BIOP) for helping me with the image analysis scripts.

A very special thanks go to all previous and current members of LSCB. They made me realize the importance of the working environment while doing a PhD. I would like to express my gratitude to them in a chronological order.

Adrian- My supervisor (even though you did not accept it) when I started the lab. Thank you for being kind and positive with me and teaching me the basics which were very important for the future of my PhD.

Sylke- Thank you for bearing with my untimely microwell orders! Without you I wouldn't be able to do almost any of the experiments I performed in my thesis. It was all good memories with you (except the ones you were trying to lock my phone for hours). I hope the success of SUN bioscience will continue in the future.

Nikolce- The lab's party animal. Thank you for being such a fun and knowledgeable person at the same time! I have learnt a lot from you. It was amazing times to have you in the lab and this continues every time we see each other. You are the real guy!

Laura- Now it's 4'o clock so it's coffee time! I still cannot sing total eclipse of the heart with the original lyrics. Thank you for always being nice and a good scientist! I wish you all the best for the future.

Nathalie- Thank you for your continuous eagerness to help and your positive mood! I wish you all the best for the future of SUN bioscience. Also, thank you very much for translating the summary of my thesis to French!

Yoji- Thank you for being always nice and helpful! I wish all the best for you and your family and promise to let you know next time I visit Japan!

Massi- “Bonjou. How about a coffee?” Thank you for always bringing the good mood and ground-breaking science in the lab! It was a great experience to learn from you and spend fun time with you. I wish all the best for your family with little Alexander.

Aleks- The external member of LSCB. It was a great experience to overlap during our PhDs and to adopt you in our lab! We had so many good moments and I believe more is yet to come. I wish you the best for the next adventures. Go team rakija!

Sonja- Freitag Sonja! We have been sitting side-by-side during these 5 years. I always see you as a great example of how one can balance PhD/non-PhD life. We had many great moments together (e.g. dancing in the lab, pipetting wine) and I am sure the future holds great potential for more memories! Alles Gute für die Zukunft!

Sara- Thank you for being an extremely positive person and a scientific/non-scientific advisor to me. I really appreciated the time we spent in the lab together and I could only wish for you to stay longer. I wish all the best for you and your family.

Delphine- La petite française! It was amazing 5 years having you sitting next to me and making every day easier with your positivity. I have always admired your constant good mood and the vibe that you give to people around you. I think my French improved a lot with our discussions. Bonne chance pour la suite!

Andrea- Thank you for your inputs, comments and help during my PhD. I greatly admire your scientific knowledge and the way you communicate them to others. I wish you all the best for your future career steps that I have no doubt you will succeed!

Giuliana- My gastruloid partner and desk-neighbor. It was amazing to work with you and have scientific/non-scientific discussions that were really valuable to me. I truly see you as an advisor. I hope your positivity continues and I wish you all the best for the future!

François- Thank you for being always in a good mood and bringing it to people around you as well. I will remember you as the social guy who always have events and parties planned. We will be having our public defenses back to back. All the best for the future and I hope you enjoy the post-PhD travelling!

Mike- The guy who always runs in the lab. Thank you for bringing energy to the lab and best wishes for your future career!

Saba- Thank you for always being nice and understanding. It was great to have someone who is culturally closer to me over these years. I wish you will have an amazing end of PhD!

Jisoo- Selam! Thank you for always being helpful and considerate. I see you as someone who cares a lot about people around her. I am very glad to be your colleague and friend. I wish you all the best for your PhD and I am sure it will be great!

Stefano-Future of gastruloids. Thank you for bringing the fun and joy with you after joining the lab. I hope you will always keep the positivity and smile on your face. I am sure you will have an amazing PhD!

Olga- Thank you for being a positive and fun person. I am glad we get to work in the same environment and all the best wishes for your PhD!

Nicolas- Thank you for always being helpful and nice. I am amazed by your knowledge in almost every field. I am sure you will have a successful career! All the best wishes.

Antonius- Thank you for always being in good mood and making people around you happy. Also, thanks for the tips for the Bali trip. I am sure you will have a great PhD!

Tania- Thank you for being fun and a good scientist at the same time. I wish you the best for your PhD!

Sophia-Thank you for always being curious and fun. I enjoyed being in the same lab with you. Best wishes for the future!

Moritz- Thank you for being a positive and fun person. It was great to have you around. I am sure you will do great during your PhD! If it doesn't work, you can have an alternative career as he Sonja!

Bilge- The second Turkish in the history of LSCB. I am quite confident that you will continue to represent our country successfully in the coming years! I wish you a great PhD!

Stefanie- Thank you for organizing the lab and putting things together. I believe the lab became much more structured after you joined the lab! Best wishes for the future.

Julia- Thank you as well for organizing the lab and specifically taking care of everything about conferences, contracts, trips, etc. I am glad to have you in the lab. Enjoy your vacations!

Finally, I would like to thank all my family for giving me the opportunity to grow up in a nice environment, to attend good schools and get high level education. I am and will always be grateful for this to my parents and great parents. Leaving home at the age of 18 for university and then moving abroad were not easy decisions for me but without the support of my family I would have never been able to come this far. They have always believed in me with any decision I took and were always behind me. I dedicate this thesis to my mother, brother, father and to my grandfathers who would have been very proud to see me becoming a doctor.